Design, Control, and Assessment of a Semi-Powered Prosthetic Ankle

By

Harrison Logan Bartlett

Dissertation

Submitted to the Faculty of the

Graduate School of Vanderbilt University

in partial fulfillment of the requirements

for the degree of

DOCTOR OF PHILOSOPHY

in

Mechanical Engineering

October 31, 2018

Nashville, Tennessee

Approved:

Michael Goldfarb, Ph.D.

Eric Barth, Ph.D.

Gerasimos Bastas, MD, Ph.D.

Nilanjan Sarkar, Ph.D.

Karl Zelik, Ph.D.

Dedicated to My Wife, Kerriann

ACKNOWLEDGEMENTS

I would like to begin by thanking my advisor, Michael Goldfarb. He is a brilliant engineer, but more importantly, a great mentor. I would like to thank Professor Goldfarb for helping to foster my academic independence and creativity while also being a source for help and guidance along the way. He has always respected my ideas and opinions and is always willing to drop everything at a moment's notice to help a student. For that, and many other admirable qualities, he has gained my respect and gratitude. I would also like to thank Drs. Eric Barth, Gerasimos Bastas, Nilanjan Sarkar, and Karl Zelik for serving as members of my committee. They have spent time and effort providing feedback and support, and my work has benefited greatly from their contributions.

I would also like to thank Dr. Brian Lawson for his continued contributions to and support of this work. Brian served as a postdoc in the lab during my time there; he is a talented engineer who has spurred many thoughtful conversations and debates. He has challenged me to grow personally and professionally while serving as a mentor, colleague, and friend. He has contributed a great deal to this work, and I look forward to future collaborations.

A number of other students and researchers have played a significant role in my graduate experience. I would like to thank the current and former members of Drs. Goldfarb and Zelik's labs for their continued support and friendship. It has been a pleasure to work in such a welcoming and collaborative environment throughout my time at Vanderbilt.

I have been lucky enough in my life to benefit from many wonderful teachers and mentors, without whose help, encouragement, and mentorship, I would not be the person I am today. I would be remiss to not give them the thanks they deserve. Dr. Lena Ting served as a generous mentor to me during my undergraduate research experiences and continues to

set a shining example of what it means to be a great teacher and scientist. As an undergraduate, her mentorship helped me define a path for myself, and I am grateful for all that she has done for me. I would also like to thank Jeff Bingham for his role in mentoring me during my undergraduate years. His depth of knowledge and dedication to his work are admirable qualities. Although his teachings seemed difficult at the time, I truly appreciate the time he spent showing me the importance of scientific and engineering rigor; I am a better engineer and person thanks to his efforts. I would also like to thank Amy Maddox, Jane Schaefer, and James Shoemaker for serving as wonderful teachers who all set examples of how to teach with humility, foster creativity in their students, and enable their students to think critically. Their infectious excitement for teaching and mentoring has had a lasting effect on me over the years, and I admire the respect with which they serve their students.

I would also like to thank my family for their continued encouragement. I am grateful to my parents for the love that they have shown and for the opportunities that they have made possible through their unconditional support. They have always been there for advice and have provided a solid foundation for me, both intellectually and morally. I would also like to thank my older brothers for setting frustratingly high standards as they paved the way. They have both served as outstanding role models and friends.

Furthermore, I would like to thank my wife, Kerriann, for her unwavering support. I am truly grateful for the endless encouragement and love that she shows. She reminds me every day of the fullness and joy that life can bring. She is my best friend, and I couldn't imagine going through life without her. For that and so much more, I am thankful.

Lastly, I would like to thank my funding sources. I would like to thank the National Science Foundation. The Graduate Research Fellowship I received from them was instrumental in my graduate experience. It allowed me flexibility in my academic pursuits,

and the work contained in this dissertation is a product of that flexibility. I was able to explore and develop as a scientist and engineer thanks to the opportunities provided by this fellowship.

TABLE OF CONTENTS

Page

LIST OF TABLES

Tables Page

LIST OF FIGURES

Chapter 1

Introduction

1.1 Document Summary and Organization

This dissertation summarizes the work performed towards the development and assessment of a semi-powered prosthetic ankle. Although the ultimate objective of the research was the development of an ankle prosthesis, the research covered by this dissertation can be divided into research that is directly related to the resulting prosthesis, and research that is indirectly related (e.g., general methods for selecting mechatronic transmissions). In order to present a more focused and unified description of the ankle prosthesis, the body of this thesis focuses almost entirely on the research directly related to the ankle prosthesis. The research that was conducted as part of this dissertation, but is not directly related to the ankle prosthesis, is mentioned towards the end of this chapter, and described more fully via associated manuscripts [1-4] included as appendices to this document.

The remainder of this chapter outlines the contributions of this dissertation, and concludes with an overview of the motivation for the work presented in this dissertation. The remaining chapters consist of both published works as well as previously unpublished material related to the design and assessment of the semi-powered prosthetic ankle. Chapter 2 describes the conceptual motivation for the prosthetic ankle. Chapter 2 also describes the first iteration of the ankle's mechanical design and level walking controller and describes preliminary experimental assessment of this device on an amputee subject. A manuscript representing Chapter 2 was submitted for publication as a journal paper in *IEEE/ASME*

Transactions on Mechatronics. The actuator design material in Chapter 2 was also presented at the *2017 International Conference on Rehabilitation Robotics (ICORR)*. Chapter 3 describes the functionality of the ankle during stair descent. Specifically, Chapter 3 describes the development of a controller for the semi-powered ankle for stair descent gait as well as presents the results of an experimental assessment of the ankle and controller on a single amputee subject. The manuscript in Chapter 3 was submitted for publication as a journal article in *IEEE Transactions on Neural Systems & Rehabilitation Engineering*. Chapter 4 describes the development of a novel hydraulic actuator concept for eliminating performance limitations present in the first prototype of the semi-powered prosthetic ankle. The work from this chapter was primarily performed in conjunction with an undergraduate student, Beau Johnson, who worked under the author's advisement. This work was submitted for publication as a journal article in the *International Journal of Fluid Power*. Chapter 5 describes a design iteration of the ankle's actuator as well as the design and assessment of a walking controller for sloped and level walking. Chapter 5 also describes an assessment of the ankle's ability to provide quiet standing supporting on various slopes/inclines. Chapter 6 presents conclusions that may be drawn from this work. Chapter 6 also presents directions for future work and development for the device developed in this work.

1.2 Contributions

1.2.1 Power-Asymmetric Actuator Concept and Design

The primary contribution of Chapter 2 is the conceptual development through design implementation of a linear actuator with asymmetric power generation and dissipation properties. This actuator is the first of its kind in that it is able to generate small

amounts of power at low force while also being able to dissipate large amounts of power at high force. These capabilities are achieved in a compact package relative to a power-symmetric actuator such as one driven by an electric motor and transmission. The power-asymmetry capabilities of this actuator are provided via a novel combination of an electromechanical drive system for power generation and a modulated hydraulic damper for high power dissipation. This power-asymmetry is provided in a compact package due to the positioning of the lead screw of the electromechanical drive system coaxial with the cylinder bore of the hydraulic cylinder. Similar actuation approaches may be useful for other applications characterized by design requirements of power asymmetry and compact packaging.

1.2.2 Stair Descent Control for Semi-powered Prosthetic Ankle

The primary contribution of Chapter 3 is the development of a control system for stair descent with a semi-powered device. Stair descent is characterized by small amounts of active (positive) power during the swing phase and large amounts of dissipative (negative) power during the loading phase. Stair descent controllers have previously been designed for fully powered prostheses executing stair descent [4-12]; however, these devices leverage the use of power-symmetric actuators that are able to generate or dissipate power through their large motors and transmissions. This chapter describes use of a semi-powered prosthesis that is able to achieve biomechanical outcome measures that are more representative of healthy norms than are achievable with standard prosthetic interventions. Moreover, this functionality is provided with a device that is approximately 50% of the mass of a fully powered prosthesis [4]. The ability of this semi-powered ankle prosthesis to achieve stair descent functionality exemplifies the utility of the power-asymmetric design. This chapter

also describes the assessment of stair descent functionality utilizing a custom force-sensing staircase to allow for inverse dynamic calculations to be applied to the prosthesis and user.

1.2.3 Constant-Volume, Single-Rod Fluid Actuator Concept and Design

One of the primary contributions of Chapter 4 is the conceptual development and physical implementation of a constant volume, single rod (CVSR) fluid actuator. This novel cylinder design allows the fluid volume of the cylinder to remain constant as a function of piston position. The constant-volume nature of this cylinder provides a solution to the many problems associated with standard single-rod cylinders (which are non-constant-volume) used in fluid power systems (especially closed hydraulic systems). This novel design builds upon prior work with multi-chamber cylinders [13-20]. Namely, this five-chamber cylinder allows for constant fluid volume as a function of piston stroke length while simultaneously minimizing the cylinder diameter. This cylinder may be useful in closed hydraulic systems that necessitate a small design envelope. Chapter 4 utilizes this constant volume cylinder design in the semi-powered ankle to provide: 1) a small design envelope while simultaneously maintaining a sufficiently large range of motion, 2) bidirectional locking capability for the device, and 3) isolation of the electromechanical drive components from hydraulic fluid volumes without the use of a high-friction shaft seal.

1.2.4 Robust Controller for Walking on Level Ground and Slopes

The primary contribution of Chapter 5 is the design and assessment of a single controller for a semi-powered prosthetic ankle that is capable of walking on sloped and level terrain. This novel controller draws insights from observations of healthy subject kinematic and kinetic data while walking across level ground and slopes. These healthy subject

observations inspired a control policy that utilizes a method of shifting the set point of the ankle's spring-like functionality across slopes based on an invariant reference in the global reference frame. This controller is similar to the work presented in [21]; however, this newly developed controller is applied to continuous sloped walking as opposed to uneven terrain. Additionally, this controller is subject to hardware constraints such that the ankle set point cannot be controlled virtually, and instead can only be set when the ankle is located at the desired set point. This hardware constraint and goal of continuous slope walking precluded the adoption of the methods presented in [21] and resulted in a new, novel controller created for this application. This controller provides a more faithful reproduction of healthy shank impedance while walking across various slopes than is provided by standard prosthetic interventions.

1.3 Related Work during Graduate Studies

Although not directly related to the development of the semi-powered ankle prosthesis, this dissertation also encompasses additional scholarly work, as briefly described in the following subsections. The manuscripts that accompany these works are included in the appendix of this thesis.

1.3.1 Transmission Ratio Optimization and Motor Selection

A method was developed for selecting the optimal transmission ratio for an electric motor for applications for which the desired torque and motion at the transmission output are known a priori. Representative applications for which the desired output torque and motion are periodic and known include robotic manipulation, robotic locomotion, powered

prostheses, and exoskeletons. Optimal transmission ratios are presented in two senses: one that minimizes the root-mean-square (RMS) electrical current and one that minimizes the RMS electrical power. Additionally, feasibility constraints are applied to the transmission ratio selection process that consider both thermal limitations (stemming from the maximum continuous current) as well as saturation limitations due to the available supply voltage. An example application is presented in order to demonstrate the method for optimal transmission ratio selection. This example application additionally highlights the implications on different motor topologies (external vs. internal rotor) on the importance of properly selecting the transmission ratio. This work was published as a journal paper in the *ASME Journal of Dynamic Systems Measurement and Control* [1].

1.3.2 Multistage Gear Train Optimization

This work presents a formulation for selecting the stage ratios and number of stages in a multistage transmission with a given desired total transmission ratio in a manner that maximizes efficiency, maximizes acceleration, or minimizes the mass of the transmission. The formulation is used to highlight several implications for gear train design, including the fact that minimizing rotational inertia and mass are competing objectives with respect to optimal selection of stage ratios, and that both rotational inertia and mass can often be minimized by increasing the total number of stages beyond a minimum realizable number. Additionally, a multistage transmission will generally provide maximum acceleration when the stage ratios increase monotonically from the motor to the load. The transmission will have minimum mass when the stage ratios decrease monotonically. The transmission will also provide maximum efficiency when the corresponding stages employ constant stage ratios. This paper aims to use this optimization formulation to elucidate tradeoffs between

various common objectives in gear train design (efficiency, acceleration, and mass). This work was published as a journal article in *Plos One* [2].

1.3.3 Phase Variable Approach for Locomotion Activity Recognition

This work describes a gait classification method which utilizes measured motion of the thigh segment provided by an inertial measurement unit (IMU). The classification method employs a phase-variable description of gait, and identifies a given activity based on the expected curvature characteristics of that activity over a gait cycle. The classification method was tested in experiments conducted with seven healthy subjects performing three different locomotor activities: level ground walking, stair descent, and stair ascent. Classification accuracy of the phase variable classification method was assessed for classifying each activity, and transitions between activities, and compared to a linear discriminant analysis (LDA) classifier as a benchmark. For the subjects tested, the phase variable classification method outperformed LDA when using non-subject-specific training data, while the LDA outperformed the phase variable approach when using subject-specific training. The proposed method may provide improved classification accuracy for gait classification applications trained with non-subject-specific data. This work offers a new method of gait classification based on a phase variable description. The method is shown to provide improved classification accuracy relative to an LDA pattern recognition framework when trained with non-subject-specific data. This work was published as a journal paper in the *IEEE Transactions on Biomedical Engineering* [3].

1.3.4 Stair Ascent and Descent Controller for a Powered Ankle Prosthesis

This work describes a control system for a powered transtibial prosthesis that provides stair ascent and descent capability, as well as an ability for user-controlled transitions between walking, standing, stair ascent, and stair descent. The control system was implemented on a powered prosthesis and evaluated on a single unilateral transtibial amputee subject. The ability of the prosthesis to provide appropriate functionality during stair ascent and descent was assessed by comparing gait kinematics and kinetics of the prosthesis to those of a passive dynamic elastic response (DER) prosthesis and those of a set of non-amputee subjects. Data from the assessment indicates that the powered prosthesis is able to provide some desirable stair ascent and stair descent characteristics, relative to the passive prosthesis. I began this work and developed the controllers to a working state. The work was then continued and refined by an undergraduate student, Steven Culver, under my advisement. The resulting work was published as a journal article in *IEEE Transactions on Neural Systems and Rehabilitation Engineering* [4].

1.4 Motivation for a Semi-Powered Prosthetic Ankle

A conventional prosthetic ankle consists of a carbon fiber ankle-foot complex that is nominally configured to a neutral position, herein called a fixed-angle stiffness (FAS) ankle prosthesis. These prostheses generally work well for level-ground walking and standing, but lack the adaptability to explicitly accommodate other terrain or locomotion activities, such as slope walking, slope standing, and stair ambulation. As such, common activities with an FAS prosthesis can be some of the most difficult for individuals with lower limb amputation.

In response to the deficiencies of FAS prostheses, several adaptive ankle-foot (AAF)

prostheses have emerged on the commercial market and in the research community over the past several years. Rather than provide strictly a fixed angle stiffness behavior, these adaptive ankle-foot prostheses provide some degree of adaptive behavior.

Adaptive prostheses can be divided into two classes: fully-powered AAF (FPAAF) devices [22-27] (e.g., Empower, Ottobock) and primarily-passive AAF [28-31] (PPAAF) devices. The primary distinction between the two is that fully powered (FP) AAF devices offer net positive power during push-off, while primarily-passive AAF prostheses do not. Providing net positive power during push-off may offer improved walking economy [32], but doing so entails a corresponding size and weight increase, and thus the benefit of net power during push-off trades off against the associated weight penalty.

PPAAF devices provide a more subtle variation on the simple FAS behavior; rather than a simple stiffness, PPAAF devices currently offer various combinations of dual behaviors. These devices can be roughly categorized as either: 1) combined damping and stiffness (CDS) devices [31] or, 2) low-power repositioning (LPR) devices [30]. CDS devices provide damping about the ankle joint within a narrow range of motion around a neutral orientation, then provide a stiffness outside of that range. These devices are available as strictly passive devices (e.g., Endolite Echelon) or in microprocessor-controlled (MPC) versions (e.g., Endolite Elan, Fillauer Raize, Otto Bock Meridium). Relative to a FAS prosthesis, CDS devices increase socket comfort during slope standing and walking by providing a congruent ankle angle [33], and may also reduce time between heel strike and foot-flat (herein called time-to-foot-flat, or TTFF) in early stance [34]. However, they may also compromise level-ground standing and walking stability and increase walking effort due to the absence of mid-stance stiffness and decreased energy return at push-off.

Additionally, CDS devices do not address several other deficiencies associated with FAS prostheses (i.e., increased stumble due to absence of swing dorsiflexion [35], compromised stair descent, etc.).

The second category of dual-behavior PPAAF devices is the LPR device. These devices are microprocessor-controlled and can vary the equilibrium angle of the ankle stiffness when the prosthesis is in swing phase. This repositioning functionality allows this device provide swing-phase dorsiflexion and equilibrium angle adjustment when walking on continuous slopes [35, 36]. Since the device is not backdrivable (i.e., lacks controllable conformal damping), however, it cannot address a number of the aforementioned deficiencies of the FAS prosthesis, including increased TTFF and lack of shock absorption in stair descent. Also, importantly, the lack of backdrivability precludes within-step adaptation to slope, and the ability to accommodate uneven terrain.

This thesis presents the mechanical design, control design, and assessment of a semi-powered prosthesis that is unique in its ability to independently adjust both its configuration (i.e., ankle neutral position) and its resistance (i.e., can be either stiff or free). Unlike a fully powered robotic ankle, the semi-powered ankle is comparable in size and weight to its passive counterparts, and yet it offers a suite of functionality that is not available in such devices. The mechanical design of the semi-powered ankle is presented. Subsequently, controllers are designed for the ankle in order to provide the appropriate biomechanical functionality during level walking, stair descent, sloped walking, and sloped standing. The semi-powered ankle is then assessed on a single subject with a transtibial amputation for each of these activities of daily living.

Chapter 2

Design, Control, and Preliminary Assessment of a Multifunctional Semi-powered Ankle Prosthesis

The current state of the art in ankle-foot prostheses is a leaf-spring-like device typically constructed from carbon fiber. While passive leaf-spring-like prosthetic ankles perform well on level terrains, they lack the behavioral adaptability to accommodate other terrains such as stairs and slopes. Recently, fully powered prosthesis have been developed to address this lack of versatility, however, these fully-powered devices require sizeable motors, transmissions, and batteries, increasing the size and weight of the prosthesis relative to the spring-like standard-of-care. This chapter describes the development of an ankle prosthesis that attempts to provide behavioral adaptability across activities and terrains while minimizing the size and weight of the device relative to fully powered prostheses. This functionality is provided via the design of a semi-powered ankle that is able to control its configuration (spring equilibrium angle) and its resistance (damping). This mechanical functionality is provided via a novel power-asymmetric actuator, the design of which is presented here. The following manuscript was submitted to the *IEEE/ASME Transactions on Mechatronics* and is currently under review for possible publication as a journal article.

2.1 Manuscript 1: Design, Control, and Preliminary Assessment of a Multifunctional Semi-powered Ankle Prosthesis

2.1.1 Abstract

This paper describes the design, control, and preliminary assessment of a novel microprocessor-controlled multifunction ankle prosthesis that provides three microprocessor-controlled behaviors – a selectable stiffness equilibrium angle, lockable conformal damping, and swing-phase repositioning. Following a description of the motivation for providing these behaviors, the authors provide a detailed description of the device and walking controller design. The functionality of the prosthesis is demonstrated by: 1) a set of benchtop experiments that characterize the ability of the prosthesis to provide the three desired behaviors; and 2) a set of experiments in which the prosthesis was worn by a transtibial amputee during walking. Both sets of experiments indicate that the prosthesis provides the functionality for which it was designed.

2.1.2 Introduction

Approximately 600,000 people in the US had a major lower limb amputation in 2005, and that number is expected to double by 2050 [37]. Major lower limb amputations are defined as those with at least an ankle amputation, and as such, all these individuals require at least a foot-ankle prosthesis, referred to here as a transtibial or ankle prosthesis, to restore legged mobility.

The current standard in transtibial prostheses is a carbon-fiber leaf spring configured to a neutral equilibrium angle, referred to here as a fixed-angle stiffness (FAS) prosthesis. This type of prosthesis is environmentally robust, lightweight, and available at low to moderate cost. These prostheses generally work well for level walking and level-ground

standing, but lack the adaptability to explicitly accommodate other terrain or locomotion activities, such as slope walking, slope standing, and stair ambulation. For example, in a study of 226 individuals with transtibial amputation [38], 88% could walk unassisted in their home and 76% could walk unassisted outside on level ground. Of the same cohort, however, only 48% could walk unassisted outside on *uneven* ground, and only 47% could walk unassisted down a few steps without a handrail. A number of other studies corroborate the substantial challenges of slope and stair walking for individuals with lower extremity amputation [33, 38-44]. Specifically, [40] reports that approximately 17% of transtibial amputees avoid climbing stairs on a daily basis. Additionally, [33] reports that amputee subjects rated socket comfort for sloped walking as significantly worse than that of level walking.

When encountering slopes, the FAS prosthesis is unable to adjust the equilibrium angle of ankle stiffness, which is necessary to provide appropriate support [45]. The limited range of motion of the FAS prostheses precludes them from appropriately tackling ramps and slopes [46]. During stair descent, the FAS prosthesis is unable to plantarflex during swing, dissipate power during the loading response, or appropriately yield in dorsiflexion during stance [47-50]. Even in level walking, the FAS prosthesis lacks the full extent of a healthy loading response at heel strike and is unable to dorsiflex during swing for toe clearance.

In order to improve upon the functionality of FAS prostheses, several multifunctional (MF) ankle prostheses have emerged on the commercial market over the past few years. Rather than providing strictly a fixed angle stiffness behavior, MF prostheses provide some degree of multifunctional behavior. Multifunctional prostheses can be regarded in two

classes: fully-powered MF devices and primarily-passive MF devices. The primary distinction between the two is that fully-powered (FP) MF devices offer net positive power during push-off [22-24, 51-53], while primarily-passive MF prostheses do not. Providing net positive power during push-off may offer improved walking economy [32], but doing so entails a corresponding size and weight increase, and thus the benefit of net push-off power trades off against the associated device weight , which is often considered a liability [54, 55].

Primarily-passive (PP) MF devices provide a more subtle variation on the simple FAS behavior; rather than a simple stiffness, PPMF devices currently on the market offer various combinations of dual behaviors. Recently, low-power PP devices have emerged in the academic community with the work in this area focusing on developing low-mass prostheses [28-30, 56]. The commercially available PPMF devices can be roughly categorized as either: 1) combined damping and stiffness (CDS) devices or, 2) low power repositioning (LPR) devices. CDS devices provide damping about the ankle joint within a narrow range of motion around a neutral orientation, then provide a stiffness outside of that range due to motion stops. These devices are available as strictly passive devices (e.g., Endolite Echelon) or in microprocessor-controlled (MPC) versions (e.g., Endolite Elan, Fillauer Raize, Otto Bock Meridium). Relative to a FAS prosthesis, CDS devices have been shown to decrease socket forces during slope standing and walking [33] and reduce braking forces limiting forward progression in early stance [34]. However, they may also compromise level-ground standing and walking stability and efficiency due to the absence of mid-stance stiffness and decreased energy return at push-off. Additionally, CDS devices do not address several other deficiencies associated with FAS prostheses (i.e., increased stumble due to absence of swing dorsiflexion [35], compromised stair descent, etc.).

The second class of dual-behavior PPMF devices is the LPR device. Although several CDS devices have recently emerged, only a single LPR device is currently available on the market, which is the Ossur Proprio Foot. This device is an MPC ankle that can vary the equilibrium angle of the ankle stiffness when the prosthesis is in swing phase (i.e., it provides the swing-phase repositioning behavior), and therefore it is able to provide swing-phase dorsiflexion and equilibrium angle adjustment when walking on continuous slopes [35, 36]. A similar device exhibiting a more compact mechanical form factor was recently described in [30]. Recent research suggests that dorsiflexion has significant biomechanical advantages with regards to preventing foot scuffing and stumbles [57]. In the implementations of LPR ankles referenced above, the devices are not backdrivable, and therefore they lack a controllable conformal damping capability. This omission prevents these devices from addressing some of the other deficiencies of the FAS prosthesis. These deficiencies include increased musculoskeletal loading, socket discomfort, and increased likelihood of slipping associated with the loading response during walking; or excessive joint loading, precarious foot placement, or decreased stability associated with stair descent.

This paper describes a novel ankle prosthesis of the primarily-passive multifunction (PPMF) type (i.e., it foregoes net-positive-power-push-off in exchange for a smaller and lighter-weight device) that encompasses the behaviors of the MPC CDS and MPC LPR devices, in a device of similar size and weight. The device incorporates: 1) high-torque lockable conformal damping; 2) a selectable ankle stiffness equilibrium angle; and 3) low-torque repositioning, and, as such, it is referred to as a damping, stiffness, and repositioning (DSR) prosthesis. No other primarily passive ankle prosthesis of which the authors are aware combines this set of features. The ability to provide these features in a compact and

lightweight package is enabled by leveraging a novel actuator, designed for this purpose, as described in the following section. The authors hypothesize that the combination of these behaviors addresses FAS deficiencies, and provides improved function to individuals with lower extremity amputation with little size or weight penalty relative to existing PPMF prostheses.

2.1.3 Prosthesis Design

A primary goal during the design of the DSR prosthesis is to minimize size and mass while maximizing functionality. To that end, a set of design requirements were drafted based on biomechanical requirements as well as commercially available prostheses and are described in detail in [58]. These requirements can be summarized as follows: 1) mass under 1.5 kg; 2) build height of less than 175 mm; 3) locking ankle torque of 120 Nm [58] ; 4) maximum dissipative power of 200 W [58]; 5) active repositioning power of 10 W; and 6) maximum repositioning speed of 100 deg/s.

2.1.3.1 *Mechanical Design*

2.1.3.1.1 *Slider-crank Ankle*

The DSR ankle utilizes a slider-crank mechanism to transduce the linear force and motion of the actuator developed in [58] to the torque and angular motion of the ankle. The geometry of the slider-crank was dictated in large part by the geometric envelope of the anatomical ankle, combined with a desired build-height of less than 175mm. The resulting configuration is shown in Fig. 2.1. Note that a compliant element (i.e., a leaf spring) connects one end of the cylinder to the structure (Fig. 2.1), which serves as a series elastic element that enables ankle torque measurement.

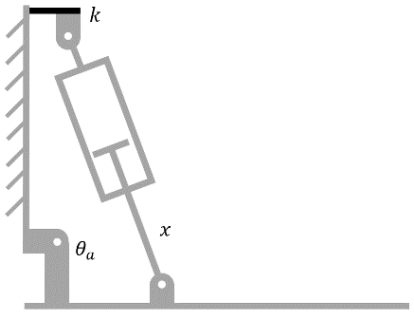

Fig. 2.1. Kinematic configuration of ankle prosthesis, also showing series elastic leaf spring.

Specifically, deformation of the leaf spring is estimated through differential measurement of the actuator length (x) and an estimated actuator length (x_θ). The estimated actuator length (x_θ) is calculated by projecting the measured ankle angle (θ_a) into the linear actuator domain through assumed rigid kinematics. Ankle torque is then computed via knowledge of the spring stiffness (k).

2.1.3.1.2 *Power-asymmetric Linear Actuator*

The power-asymmetric linear actuator leverages the uniqueness of the required ankle behaviors to provide these behaviors in a compact and lightweight device. Recall that the DSR ankle requires three behaviors: 1) high-torque lockable conformal damping; 2) locking the ankle at a desired angle to set the equilibrium point of the ankle stiffness; and 3) low-torque and power repositioning. The first two behaviors are strictly passive, but require high torque capability, and in the case of the conformal damping, high power dissipation (e.g., toe strike in stair descent). The third behavior is an active behavior, but requires relatively low power and low torque to achieve. As such, a substantial power-asymmetry exists in the design requirements. The investigators leverage this asymmetry by using an electrically-

modulated hydraulic system to provide the high-torque and high-power controllable locking and damping functionality and by using direct electrical actuation to perform the low-torque and low-power controllable ankle repositioning. As is well-known in the actuation and prosthetics communities, hydraulic systems provide (passive) torque and power densities approximately an order-of-magnitude greater than electrical drives [59]. Electromechanical drive systems, however, are easily controllable and can provide information about the configuration of the actuator if a positive engagement transmission is utilized. This dual-actuation approach leverages the asymmetry of requirements between active and passive behaviors, and is intended to provide a smaller and lighter actuation package than would be possible with a conventional single actuator approach. Due to the fundamental asymmetric nature of the actuator, it is referred to as a power asymmetric linear (PAL) actuator. A detailed description of the design and characterization of this actuator can be found in [58], and a summary of the design is given here.

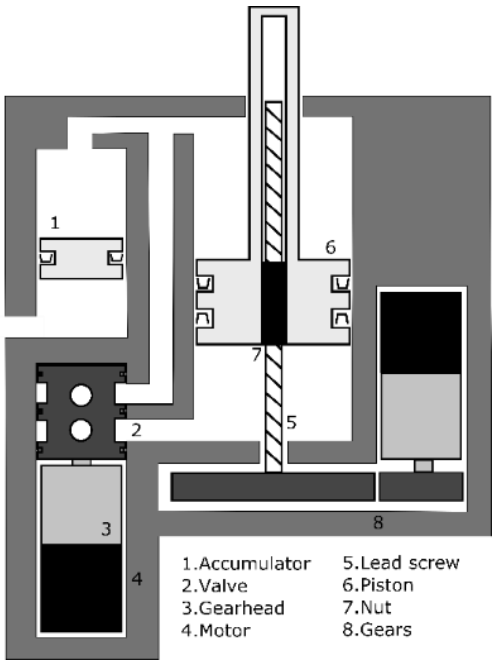

Fig. 2.2: Schematic representation of the power asymmetric linear (PAL) actuator.

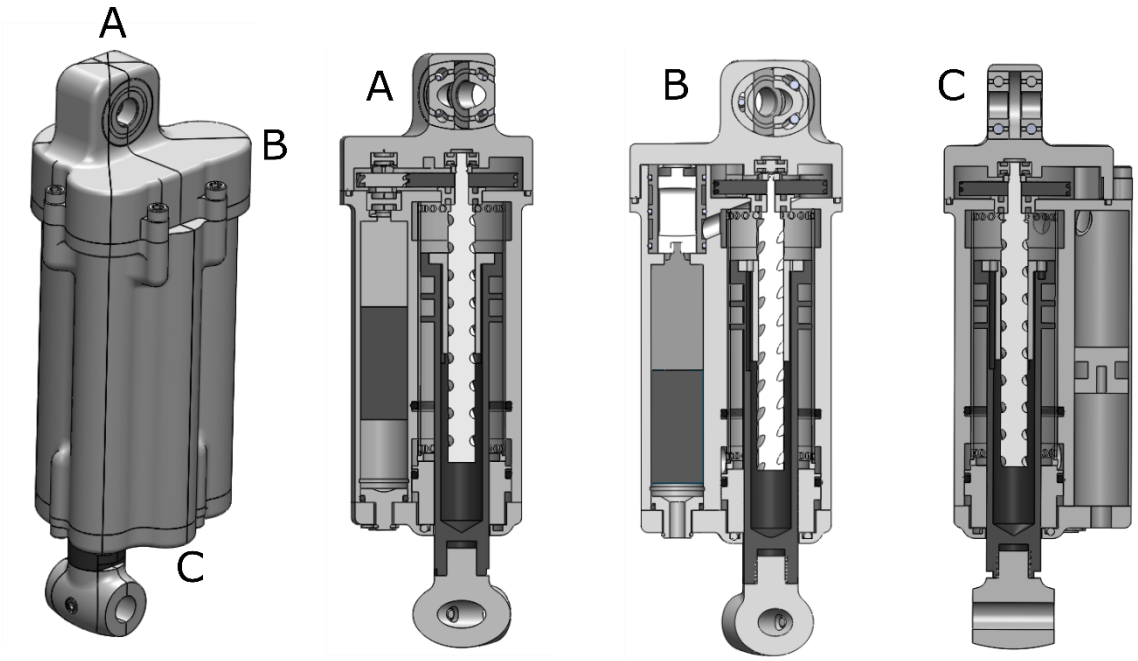

Fig. 2.3. Multiple cross section view of the PAL actuator: section A shows electromechanical drive system; section B shows the hydraulic damper valve; and section C shows the accumulator.

The PAL actuator, which is shown schematically in Fig. 2.2, consists of a linear hydraulic actuator, with fluid flow governed by a two-way proportional hydraulic valve

(similar to those employed in modulated passive prostheses such as the Endolite Elan ankle or the Otto Bock C-Leg). The power generation drive system consists of an electric motor and gearhead driving a set of gears which connect to a lead screw, which is in turn nested inside of the piston and rod of the hydraulic circuit to which the lead nut is attached. By placing much of electromechanical transmission inside the hydraulic unit, the two parallel systems can be realized in a small overall package. The electromechanical drive system of the actuator was designed to be backdrivable so that dissipative loads applied to the system are reacted by the high impedance hydraulic load pathway, rather than the electromechanical drive system, which enables the use of small drive components. Note also that an accumulator accommodates fluid volume changes as the rod enters and exits the cylinder.

A series of section views of the actuator can be seen in Fig. 2.3. These section views indicate planes showing the electromechanical drive system (section A), the damping valve (section B), and the accumulator (section C). The modulated damping and locking functionality of the actuator is performed by an integrated proportional servo valve. The valve is a pressure-balanced two-way spool-and-sleeve valve driven by a Faulhaber brushless DC 1226 10 W motor in series with a 64:1 gearhead. Valve position sensing is provided by the motor's Hall Effect sensors, which provides a position resolution of the valve of 0.94 deg. The valve is pressure balanced, and as such damping can be modulated without regard to load.

The drive system consists also of a Faulhaber brushless DC 1226 10 W motor, although with a 16:1 gearhead. The gearhead is coupled to a 2.25:1 helical gear stage, the output of which drives a lead screw. The lead screw, which was chosen for its high efficiency and backdrivability, is 6.35 mm (0.25 in) in diameter and has a lead of 6.35 mm (0.25 in).

The lead nut is fixed to the hydraulic piston such that the lead screw can enter and exit the hollow bore of the piston rod as the actuator moves. This transmission system was designed with aid from the methods presented in [1, 60]. Position sensing of the actuator is provided by the Hall Effect sensors of the motor in order to minimize the size of the device. The resulting linear position resolution of the actuator is 0.03 mm. Note finally that use of helical gears and a lead screw also minimizes audible noise.

Fig. 2.4: Photograph of constructed PAL actuator and pen (for scale).

A photograph of the prototype PAL actuator can be seen in Fig. 2.4. The actuator was experimentally characterized in [58], with characteristics summarized in Fig. 2.5. Figure 2.5a shows the measured damping characteristics of the actuator, where the different lines in Fig. 2.5a represent various levels of damping (i.e., each line/color represent data recorded with the rotary spool and sleeve valve in a different position). Based on the data shown, the valve has a dynamic range of approximately 250:1, and is able to move through its full range of motion (and subsequently through the full range of damping values) in approximately 0.04 s. A dashed line is included in Fig. 2.5a to indicate the damping level associated with the stance phase of stair descent as reflected in the linear actuator domain. This damping value represents the largest value of ankle damping seen in common locomotor activities. It should be noted that the levels of damping obtained with the valve span the

range of biomechanically relevant damping values as indicated by the stair descent damping falling within the range of damping obtainable by the actuator.

In order to characterize the repositioning ability of the device, the actuator was subjected to a step movement command, the results of which can be seen in Fig. 2.5b. The actuator is able to move 2.5 cm in approximately 0.3 s, reaching maximum ankle angular velocities of approximately 140 deg/s (compared to the 100 deg/s design requirement). When translated into the rotary domain of the ankle, this represents an ankle movement of approximately 30 deg. The actuator also exhibits a full range of motion -3 dB bandwidth of approximately 2.5 Hz.

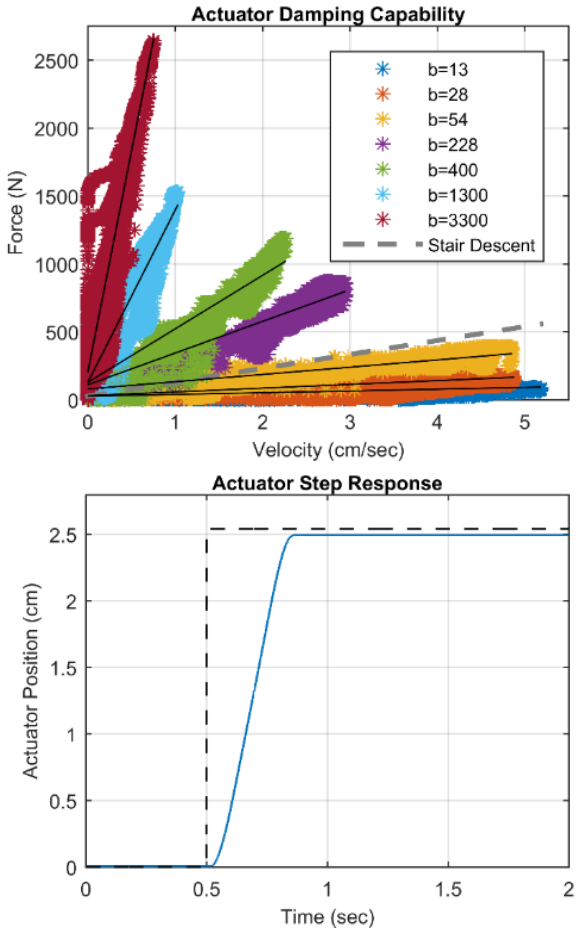

Fig. 2.5. (a) Applied force plotted against actuator velocity for a set of valve damping settings, and (b) step response of the actuator.

2.1.3.2 *Ankle Structure*

A photo of the ankle assembly is shown in Fig. 2.6. As can be seen in Fig. 2.6, the ankle prosthesis utilizes a standard carbon fiber foot plate, which can be configured in varying sizes or stiffnesses. Additionally, the prosthesis uses a standardized pyramid connector to interface with an amputee's socket on their residual limb. The structural components of the prosthesis are machined from 7075 aluminum alloy. It should also be noted from Fig. 2.6 that both the embedded system and battery for the device are housed onboard. The ankle is backdriveable and has a range of motion of 12 deg dorsiflexion to 30 deg plantarflexion.

The current prototype has a mass of 1.35 kg (including the onboard battery) and has a build height of 16.3 cm (compared to a 17.5 cm build height and 1.5 kg design requirement). For purposes of comparison, the Ossur Proprio Foot has a mass of 1.25 kg and has a build height of 18.6 cm (with off-board battery), and as such, the DSR is approximately the same size and weight.

Fig. 2.6. Photograph of the constructed ankle prosthesis. The ankle embedded system can be seen on the side of the device (blue). The battery is housed in the posterior portion of the device and not clearly visible in the figure.

2.1.3.3 *Electrical Design*

The embedded system architecture for the DSR prototype is depicted in Fig. 2.7. All hardware components necessary for untethered operation are integrated into the prototype. For the experiments described in this paper, however, a high-level controller was implemented in MATLAB Simulink in order to facilitate a rapid development iteration cycle, where communication between the embedded system and Simulink was provided by a CAN bus at a sampling rate of 1 kHz.

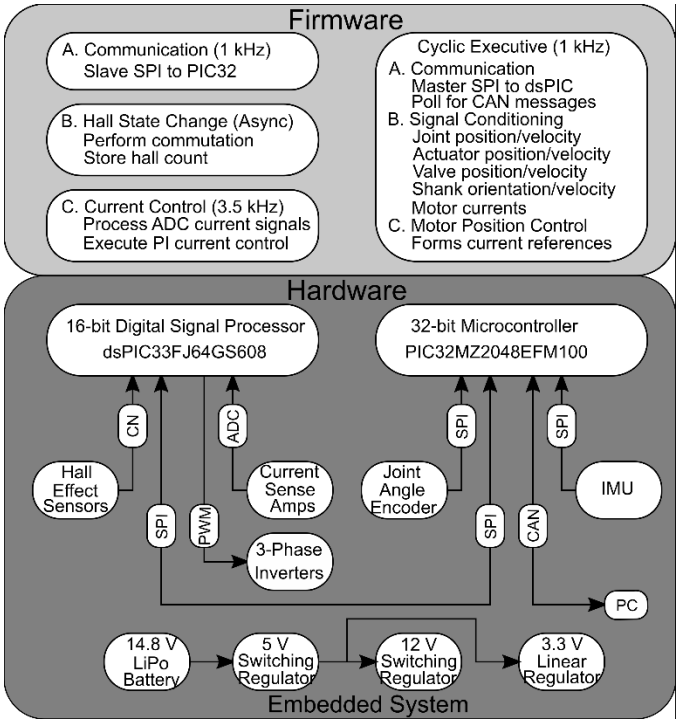

Fig. 2.7: Embedded system architecture showing both hardware and firmware.

The embedded system employs two processors: a main processor and a digital signal processor. The main processor is a 32-bit general purpose microcontroller available from Microchip Technology Inc. The main processor asynchronously receives position reference updates for the valve and actuator motors (Faulhaber 1226) over the CAN bus and implements a PD position control loop. This loop is cascaded with a current control loop in the digital signal processor (DSP), and so it generates a current reference that is subsequently passed to the DSP over a Serial Peripheral Interface (SPI). The main processor also performs the majority of the signal conditioning in the embedded system, calculating position and velocity for both motors and the joint position encoder as IEEE single-precision floating point values. It estimates the orientation of the prosthetic shank in the sagittal plane through the use of complimentary filters combining the low frequency components of the inverse-tangent of the in-plane accelerometer signals with the high-frequency components of the

integral of the in-plane rate gyroscope signal.

The current references are passed to the DSP at 1 kHz, which implements a PI current control loop at 3.5 kHz. The DSP monitors the Hall Effect signals to perform commutation via a custom 3-phase inverter for each motor. The current loop can enforce peak currents of up to 6 A and has a -3 dB bandwidth of approximately 100 Hz. When not actively responding to a reference change, the DSP disables the bridge and halts the PWM signals to reduce electrical noise.

The prosthesis is powered by a 92 g two-cell lithium-polymer battery pack (nominal 14.8 V) rated at 910 mAh, and is housed within the prosthesis frame (posterior to the embedded system). Based on data recorded during subject testing, the battery provides sufficient energy for approximately 25,000 steps. The embedded system generates the regulated voltages depicted in Fig. 2.7 and monitors both battery voltage and current for safety, shutting down during sustained over-current conditions or when the battery is depleted. A photo of the custom embedded system can be seen in Fig. 2.8.

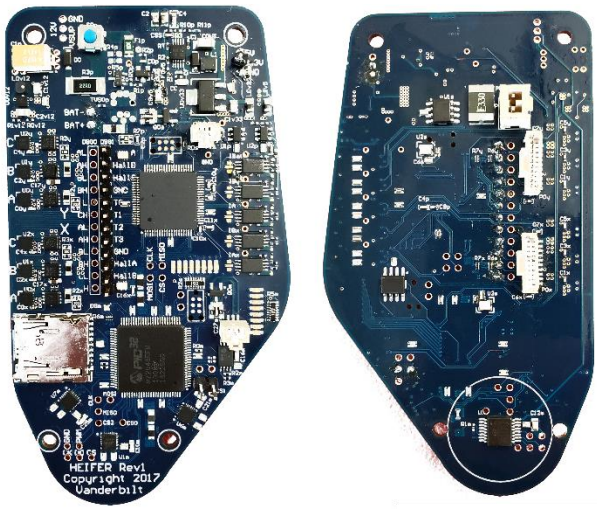

Fig. 2.8: Front and back of the custom embedded system.

2.1.4 Level Walking Control

A finite state machine controller was developed and implemented in the ankle to allow for level ground walking with the device. The level walking controller requires the use of all three of the experimental ankle device's functionalities: damping (during heel strike), stiffness (during middle and late stance), and repositioning (during swing).

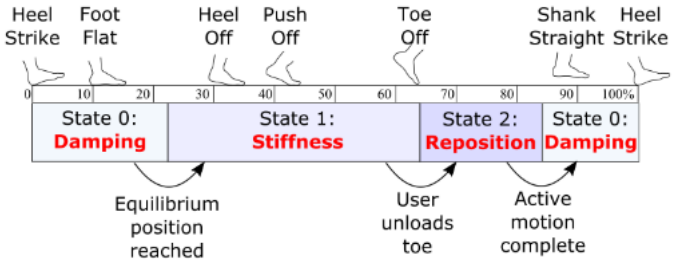

Fig. 2.9: Level walking finite state machine controller with three states: 0-2 as well as transition conditions between these states.

A pictorial depiction of the level walking finite state machine controller can be seen in Fig. 2.9. The controller is initialized in the stance state in which the valve is closed, thereby making the ankle joint very stiff. This ankle stiffness provides support to the user during the stance phase of gait and allows the carbon fiber foot plate to absorb and subsequently release energy. To transition from the stance state to the swing state, the prosthesis must experience a dorsiflexive torque above a threshold value followed by an unloading of the ankle (i.e. the torque value subsequently drops below a second threshold value). This torque signal is used to indicate that the user has unloaded the prosthesis and is about to enter swing. During the swing state, the valve opens in order to decrease the hydraulic impedance, and the prosthesis dorsiflexes to provide toe clearance. After the ankle is finished with the dorsiflexive motion

(as indicated by a threshold ankle angle value being reached), the ankle enters the ground conformation state in which the valve is partially closed in order to provide ankle damping. This damping state allows the ankle to adjust to the local slope of the ground and is active during the early part of the stance phase. The stance state is active during the late part of the stance phase of gait and is initiated based on the shank angle reaching a predetermined threshold value relative to the gravity vector (where the shank is approximately parallel with the gravity vector). Similar shank-based methods for controlling an ankle prosthesis were utilized in [61].

2.1.5 Subject Testing

The prosthesis and walking controller were assessed on an individual with a transtibial amputation. The subject was male, 51 years old, 11 years post-amputation, and had a body mass of 83 kg. Informed consent and approval for the experiments were obtained prior to testing through Vanderbilt University's Institutional Review Board.

After various control parameters were tuned and the subject became acquainted with the device, the subject walked on a treadmill at 0.8 m/s. A photo of the subject walking on the treadmill is shown in Fig. 2.10.

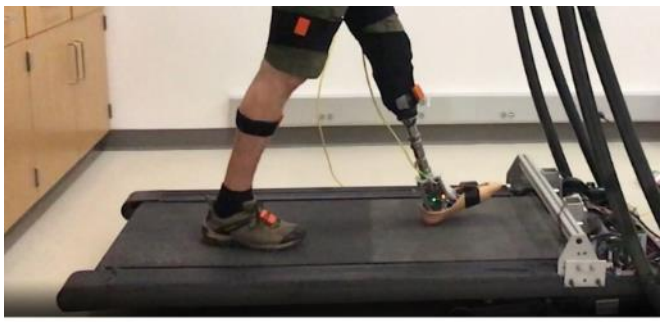

Fig. 2.10: Photograph of transtibial amputee subject walking on the experimental prosthesis. Motion capture sensors can be seen in orange.

Data from this walking trial are shown in Fig. 2.11. Specifically, the plots show the average ankle angle and shank angle over 34 strides of treadmill walking, along with plus and minus one standard deviation for each. The data were collected using an Xsens motion capture system and the MVN software analysis package (note the motion capture sensors in the photo). The plot also shows, for reference, similar data corresponding to the average of 10 healthy subjects (walking at 1.2 m/s). The plot additionally indicates the average time of the controller state transitions as indicated by the solid vertical lines. Note that the ankle angle provided by the DSR ankle provides similar early and middle stance behavior to the healthy data. Unlike the healthy subject ankle data, however, the DSR ankle (by design) does not provide the late-stance plantarflexion (corresponding to active healthy push-off). It should also be noted that the state transition from the swing state to the conformal damping state occurs at approximately 85% of stride, indicating that the ankle is able to dorsiflex quickly enough to complete the swing trajectory well before the end of a stride (15% of stride before the subsequent foot strike). Additionally, unlike the healthy data, the DSR ankle provides a somewhat exaggerated ankle dorsiflexion in swing, which is intended to add a measure of safety for the user. Thus, these preliminary ankle data indicate that the DSR provides the intended prosthesis behaviors relative to corresponding healthy data. Further,

the similarity of the shank angle data between the subject with a transtibial amputation and healthy data indicate that whole-body motion between the two is similar, which is among the objectives of a transtibial prosthesis.

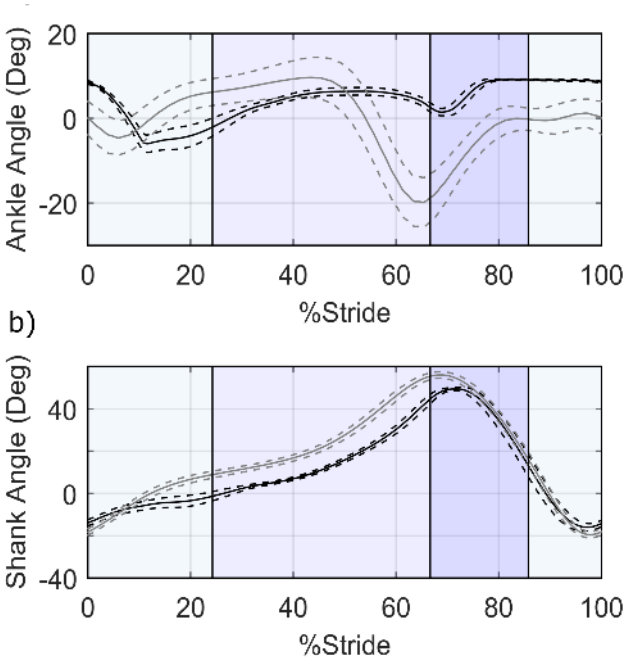

Fig. 2.11. (a) Healthy subject ankle angle data (gray) as a function of stride and experimental prosthesis data (black) plotted against percent stride. Vertical lines indicate state transitions in the finite state machine controller (shaded region colors match colors of controller state in Fig. 2.9); (b) Healthy subject and experimental prosthesis shank angle data plotted against percent stride. Dashed lines indicate +/- one standard deviation.

2.1.6 Conclusion

This paper describes the design of a semi-powered ankle prosthesis capable of providing the three following functionalities: 1) high-torque lockable conformal damping; 2) selectable ankle stiffness equilibrium angle; and 3) swing phase repositioning. A novel power-asymmetric actuator was developed for this purpose and integrated into an ankle prosthesis structure. A custom embedded system was developed for this application, and a finite state machine controller was implemented on the prosthesis to allow for level ground

walking. The prosthesis and walking controller were tested on an amputee subject, evaluated with a motion capture system, and shown to provide the intended behaviors.

2.1.7 Future Work

Future work with this device will include further control development in order to accommodate a wide variety of gait activities. Additionally, the biomechanical benefit of this device for amputee gait should be assessed for various activities. It is expected that the conformal damping functionality of this ankle will allow for comfortable gait across sloped and uneven terrain. Additionally, the locked support functionality of this ankle is expected to show benefit to amputees during standing (including sloped standing) as well as during the energy storage and release portion of many different activities. The active repositioning functionality of this ankle is expected to show benefit with regard to increasing toe clearance during the swing phase of walking as well as actively repositioning the ankle in order to properly make toe contact with a step during stair descent. Control for these various activities will be developed and assessed.

Chapter 3

Stair Descent Functionality in a Semi-Powered Ankle Prosthesis

Currently available passive and primarily-passive prosthetic ankle are incapable of providing appropriate biomechanical stair descent behavior. Namely, currently-available devices are not able to provide a foot-strike behavior and subsequent center-of-mass lowering behaviors that are seen in intact ankles. These two behaviors are characterized by small positive powers during ankle repositioning and large negative powers during lowering, which complement the capabilities of the power-asymmetric actuator utilized in the semi-powered ankle prosthesis. This chapter presents the development and assessment of a controller for stair descent functionality. The following manuscript was submitted for possible publication as a journal article in *IEEE Transactions on Neural Systems & Rehabilitation Engineering* and is currently under review.

3.1 Manuscript 2: Stair Descent Functionality in a Semi-Powered Ankle Prosthesis

3.1.1 Abstract

This paper describes a semi-powered ankle prosthesis and controller that offer enhanced stair descent functionality relative to a standard ankle prosthesis. Among the functional differences, the device uses a small motor to plantarflex the ankle during swing phase to prepare for foot contact with a stair and subsequently employs a hydraulic damper during early stance phase to lower the heel to the stair following foot contact. A controller to provide this functionality is described, and following this description, the results of a

functional assessment are reported comparing stair descent functionality on a single transtibial amputee subject relative to stair descent functionality with the subject's daily-use prosthesis. The experimental results indicate that the semi-powered device may provide more desirable behavior during stair descent relative to a standard prosthesis.

3.1.2 Introduction

Stairs are commonplace in most environments and can pose substantial challenges to individuals with lower limb amputation (ILLA). Conventional prosthetic ankles do little to replicate healthy human gait [62], particularly with regard to stair descent. For example, the healthy ankle plantarflexes during the swing phase of stair descent in order to contact the stair with the forefoot. Additionally, during the early stance phase of stair descent, the ankle dissipates substantial energy, thus providing a controlled descent. These two defining features of healthy human gait are not provided by the dynamic-elastic-response (DER) feet currently available to ILLAs. Specifically, DER feet cannot configure (i.e., reposition) themselves in swing to prepare for such dissipation, and further are unable to dissipate substantial power due to their spring-like nature.

Over the past decade, there have been substantial advances in the design and control of powered transtibial microprocessor-controlled prosthetic devices [22-25, 52, 53, 63-65], including works that describe the use of powered ankle prostheses for stair descent locomotion [4, 49, 66]. Researchers have also studied stair ambulation with powered prostheses [5-12], and associated methods of intent recognition [10-12].

Among this prior work, the authors have previously described the control of a fully powered prosthesis for stair descent [4]. Although the powered transtibial prosthesis

described in that work was shown to provide improvements in stair functionality relative to a conventional ankle, that device was heavier, larger, and produced more audible noise than a conventional (i.e., non-powered) prosthesis. Observation of stair descent characteristics of that device helped motivate the work described here. Specifically, for the ankle joint, healthy stair descent gait is characterized by substantial plantarflexive resistive ankle torque and substantial corresponding power dissipation during stance, along with a relatively small amount of powered plantarflexive torque and a correspondingly small amount of power generation during swing [67]. As such, the torque and power characteristics employed in an ankle during stair descent are highly asymmetric, characterized by small amounts of power generation and active torque, and large amounts of power dissipation and dissipative torque. In the case of a powered transtibial device performing this activity, such as the device described in [4], which is characterized by nominally symmetric power and torque characteristics, the size of the actuator (typically an electric motor) and transmission is based on the maximum torque and power requirements, in this case dissipative, which renders it large and heavy compared to commercially available DER prostheses. Rather than employ a nominally power-symmetric device, this paper describes a "semi-powered" device and associated control method that uses a hydraulic actuator to provide large dissipative torque and power, in combination with a small motor and transmission to provide relative small amounts of low-torque positive power. This design leverages the power-asymmetric nature of stair descent activity, and in doing so allows the semi-powered device to be smaller in both size and weight compared to the powered device, and yet to provide similar stair descent functionality. This paper briefly describes the device design; describes a device controller to provide stair descent functionality; and presents data from experiments on a single transtibial

amputee subject demonstrating stair descent behavior of the semi-powered device relative to a conventional ankle prosthesis.

3.1.3 Device Design

3.1.3.1 *Hardware*

Semi-powered prostheses have recently been described in the research literature in response to the desire for adaptable behaviors, without the full weight associated with fully-powered prostheses [28-30]. The prosthesis utilized in this work is able to generate small amounts of positive power and dissipate large amounts of negative power, consistent with the requirements for stair descent gait. This power asymmetry is achieved mechanically through the use of a custom power-asymmetric linear (PAL) actuator as described in [58]. The PAL is able to dissipate power controllably via a hydraulic cylinder with a controllable variable damper valve, and is able to generate low-torque power via a lead-screw-based electromechanical drive system. The size of the actuator is minimized by placing the lead screw coaxially within the hydraulic cylinder (lead screw is concentric with the cylinder rod), as illustrated schematically in Fig. 3.1.

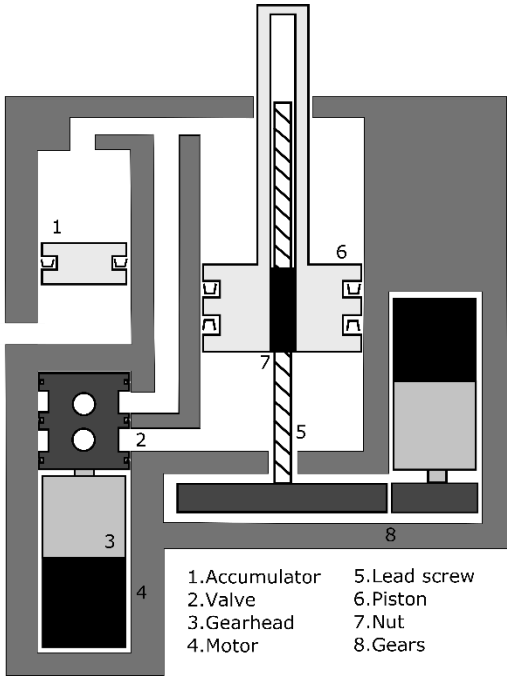

Fig. 3.1: Diagram of the power asymmetric linear (PAL) actuator.

The variable damper valve consists of a pressure-balanced rotary spool and sleeve valve driven by a 10 W Faulhaber 1226 motor in series with a 64:1 planetary gearhead. Position sensing of the valve is provided by Hall Effect sensors within the motor. The electromechanical drive system consists of a second 10 W Faulhaber 1226 motor in series with a 16:1 planetary gearhead, which drives a set of helical gears (ratio 2.25:1), which in turn drive a backdriveable lead screw. As previously mentioned, the lead screw is concentric with the rod of the hydraulic cylinder, driving a nut that is affixed to the piston within the cylinder. This mechanical transmission was designed using methods described in [1, 60]. A detailed description of the actuator design and characterization is given in [58].

The linear motion of this actuator is translated into a rotary ankle motion through the use of a slider-crank arrangement configured as shown in Fig. 3.2. In order to measure ankle torque, the PAL actuator is mounted on the end of a cantilevered piece of spring steel (Fig. 3.2). Spring deflection is measured via differential measurement of the linear actuator length

(x) and the ankle angle (θ_a) reflected into the linear actuator domain through assumed rigid kinematics. Ankle torque is then calculated by combining the known spring stiffness (k) and the measured deflection, then converting the calculated force to torque via the known system geometry.

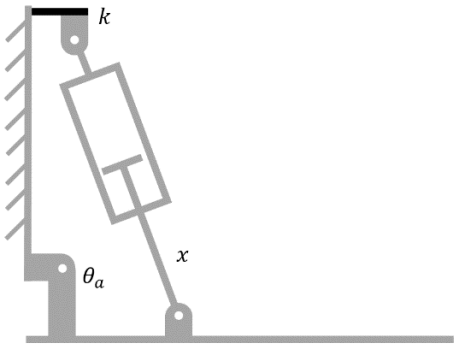

Fig. 3.2: Slider crank configuration of ankle with elastic element (black bar) in series with the PAL actuator.

A photo of the prosthetic ankle is shown in Fig. 3.3. The prosthesis uses a standard pyramid connector for interfacing with a standard socket, and also uses a carbon fiber footplate that can be changed to adapt the stiffness of the foot to a specific user. A custom embedded system developed for this device is also shown embedded in the structural frame of the prosthesis.

Fig. 3.3: Constructed prototype of the semi-powered transtibial prosthesis with visible embedded system.

3.1.3.2 *Sensing and Electronics*

Prosthesis sensing includes an absolute ankle angle encoder, a 6-axis IMU, and the Hall Effect sensors on both the drive and valve motors to measure ankle angle, global reference frame orientation, PAL actuator position, and valve position.

The custom embedded system (Fig. 3.3) incorporates two processors: a main processor and a digital signal processor. The onboard processors provide current control inner loops and position control outer loops for both brushless motors. Although the embedded system is capable of untethered operation, the experiments described herein were conducted with a high-level state-machine running remotely on a laptop computer in a MATLAB Simulink runtime environment, connected to the onboard processor via a CAN bus, which was employed for rapid prototyping of the controller and simplified data collection. The state machine issued position-control commands to the embedded system via the CAN bus, which were executed by the onboard system. A depiction of this cascaded control structure is shown in Fig. 3.4. All power for the prosthesis was provided by an onboard two-cell, 910 mAh, lithium polymer battery pack with a mass of 92 g (14.8 V).

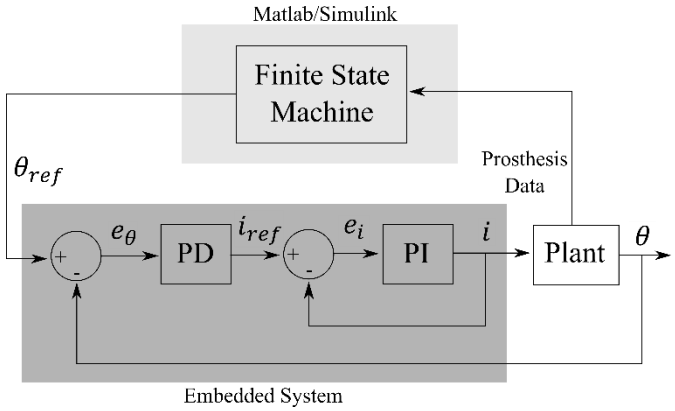

Fig. 3.4: Control loop of prosthesis illustrating the distribution of control between a computer running Matlab/Simulink (lightly shaded region) and the onboard embedded system (dark shaded region) as well as the cascaded low level control. This approach to control applies to the control of both motors. θ, i, and e is the notation for angle, current, and error, respectively. Subscripts of ref, θ, and i denote a reference or that the error pertains to angle or current.

3.1.4 Stair Descent Controller

As previously mentioned, the stair descent controller takes the form of a finite state machine, which sends position references to the two brushless motors on the prosthesis. The state machine consists of three states: Swing, Stance, and Lock and during stair descent progresses through states in that order. The Swing state plantarflexes the ankle in anticipation of contact with a stair. During the Swing state, the valve opens fully and allows the ankle to plantarflex in preparation for stair contact. Once the ankle has plantarflexed past a predetermined threshold angle (ankle is fully plantarflexed) or the ankle angular velocity becomes positive (stair contact has been made), the ankle moves into the Stance state. Once in the Stance state, the valve moves to a pre-specified position to provide the appropriate level of stance damping in order to provide stability to the user. Upon loading, as the user progresses though the stance phase, the ankle dorsiflexes, first to foot flat, then continues to dorsiflex as the user progresses downstairs. Once the ankle has dorsiflexed to a

predetermined threshold angle, the finite state machine transitions to the Lock state at which time the valve closes entirely to provide an ankle stiffness, similar to a conventional carbon-fiber device, albeit at a more appropriately dorsiflexed angle. This stiffness state allows the user to roll over the ankle without the ankle continuing to dorsiflex in preparation for the subsequent swing phase. As the user begins to lift his or her foot for the subsequent swing phase, the ankle torque decreases, indicating to the state machine a transition back to the Swing state. A diagram of the finite state machine controller, showing states and the transitions between them, is shown in Fig. 3.5, and a table containing transition thresholds can be seen in Table 3.1.

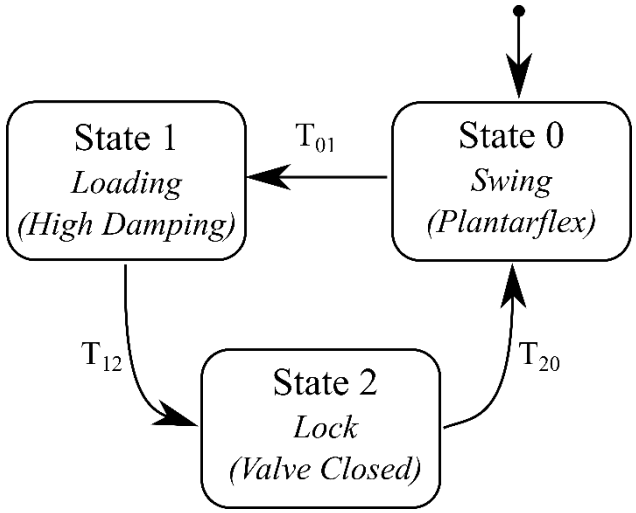

Fig. 3.5: Stair descent finite state machine controller initializing in state 0 and transitioning between states according to the transition conditions outlined in Table 3.1.

TABLE 3.1
FINITE STATE TRANSITIONS FOR THE STAIR DESCENT CONTROLLER

Transition	Description	Condition
T_{01}	Ankle has completed plantarflexion motion or ankle has made contact with stair	$\theta_a < \theta_{th,01}$ $\dot{\theta}_a > 0$
T_{12}	Ankle dorsiflexes past threshold angle as user rolls over foot	$\theta_a > \theta_{th,12}$
T_{20}	Ankle is unloaded as user enters swing phase	$\tau < \tau_{th,20}$

3.1.5 Controller Assessment

3.1.5.1 *Subject Testing*

The controller was evaluated on a single transtibial amputee subject. This subject was male, 83 kg, 51 years of age, 11 years post amputation, and left side affected. Informed consent and approval for the experiments were obtained prior to testing through Vanderbilt University's Institutional Review Board. The subject's daily use prosthesis is a Fillauer Allpro (a passive carbon-fiber prosthesis). During testing, the subject descended a flight of 4 stairs, as illustrated in Fig. 3.6, 13 times, alternating the starting foot during each descent. The descents occurred at the subject's self-selected speed. The subject performed these descents in entirety first wearing his daily-use device, and then with the semi-powered device. This order was chosen so that any effects of fatigue would favor the control condition (daily-use device).

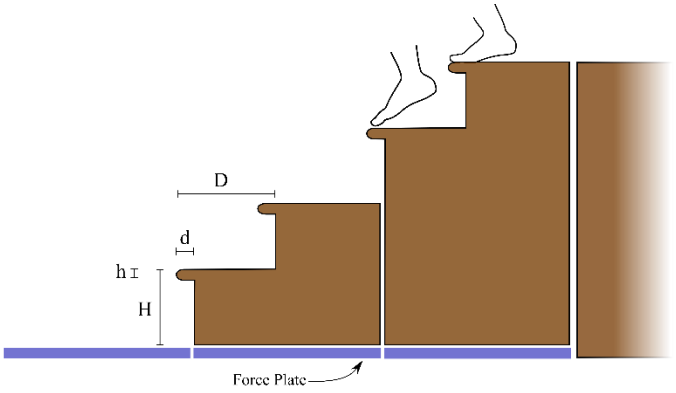

Fig. 3.6: Instrumented staircase (four stairs) with sections of the staircase mounted on over-ground force plates. Stair dimensions are also indicated.

3.1.5.2 *Data Collection and Analysis*

During the experiments, ground reaction force data were collected under each foot at 1000 Hz using a split-tread custom force-instrumented staircase, and lower-body kinematics were recorded at 200 Hz via a synchronized motion capture system (Vicon). The instrumented staircase is pictured in profile in Fig. 6. The staircase is split into separate right and left steps, with each of the resulting four stair modules mounted rigidly to a different 6-axis force plate (AMTI model OPT400600), such that the forces associated with each foot strike are recorded exclusively by a single force plate. The dimensions of the stairs are as marked in Fig. 3.6 where h=2.5 cm, H=17.8 cm, d=3.8 cm, and D=29.2 cm. Passive reflective markers were placed bilaterally on the anterior/posterior superior iliac spine, medial/lateral epicondyle and malleolus, calcaneus, 1st and 5th metatarsal, and navicular. Clusters of four markers were placed bilaterally on the thigh and shank segment for segment tracking purposes. Six markers were placed on the prosthetic socket (cluster of four on the body of socket and two on the medial/lateral epicondyle), and six were placed on the prosthetic foot (estimated location of medial/lateral malleolus, calcaneus, 1st and 5th

metatarsal and navicular).

Biological joint angles, moments and powers were calculated over the stride using biomechanics modeling software (Visual 3D) and previously published techniques for 6 degree of freedom inverse dynamics [68].

All data were divided into strides normalized to 100% stride cycle, then averaged across strides prior to reporting. Ground reactions forces and motion capture data were filtered in post-processing with a zero-phase, 3rd order low-pass Butterworth filter at 15 Hz and 6 Hz, respectively.

In order to assess the efficacy of the controller, ankle angle, ankle torque, ground reaction forces, and energy dissipated by the ankle during the stride were all assessed. These data were compared between the semi-powered ankle and the subject's daily-use prosthesis. Healthy subject data from [67] was utilized as a reference where possible.

The stair descent controller was designed to function on stairs of any geometry. To assess this capability of the controller, kinematic data was recorded using the aforementioned motion capture system on a second set of (non-instrumented) stairs of different geometry. This second set of stairs consists of three steps, with dimensions of h=2.5 cm, H=16.5 cm, d=3.2 cm, and D=28.6 cm (i.e., 8% less rise, 2% less run, 6% difference in slope). The subject descended this set of stairs five times with the semi-powered prosthesis (allowing for motion capture data from five stair descent strides to be recorded).

3.1.6 Results

Ankle angle was recorded from the motion capture system and averaged across strides for both the semi-powered and daily-use prostheses and can be seen in Fig. 3.7. A

healthy ankle angle curve is provided as a point of comparison [67].

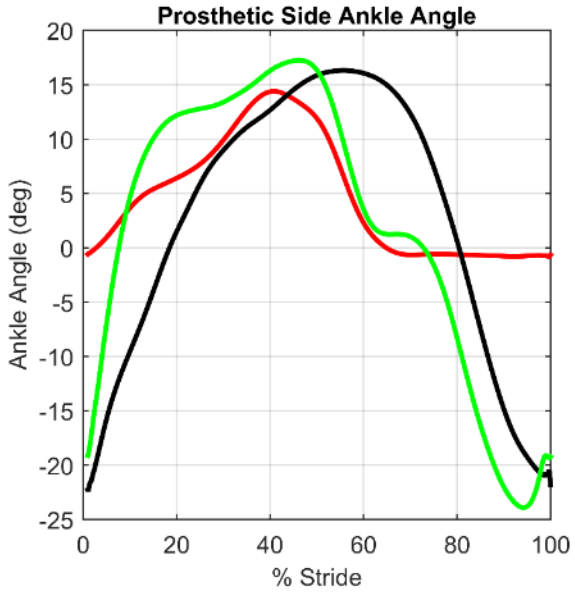

Fig. 3.7: Average ankle angle during stair descent stride for the semi-powered prosthesis (black), daily-use prosthesis (red), and healthy subjects (green).

Ankle torque was computed (using Visual 3D software) based on an inverse dynamics analysis, and is shown for the different experimental conditions in Fig. 3.8.

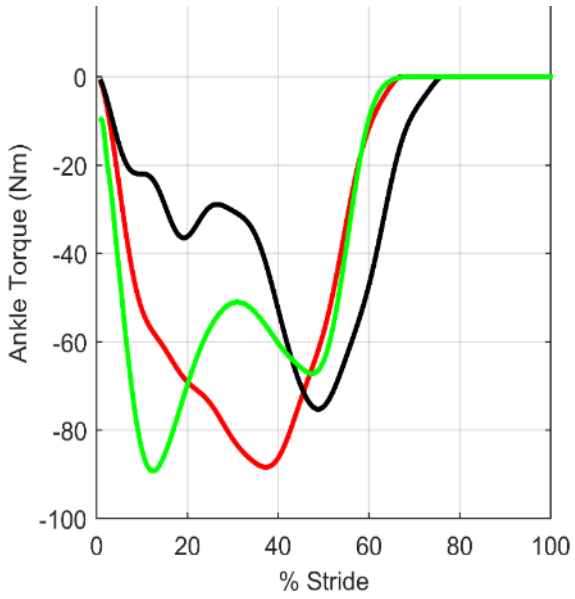

Fig. 3.8: Average ankle torque for the semi-powered prosthesis (black), daily-use prosthesis (red), and healthy subjects (green).

The instrumented staircase allowed for ground reaction forces to be directly measured during stair descent. The ground reaction force magnitudes during descent are shown in Fig. 3.9.

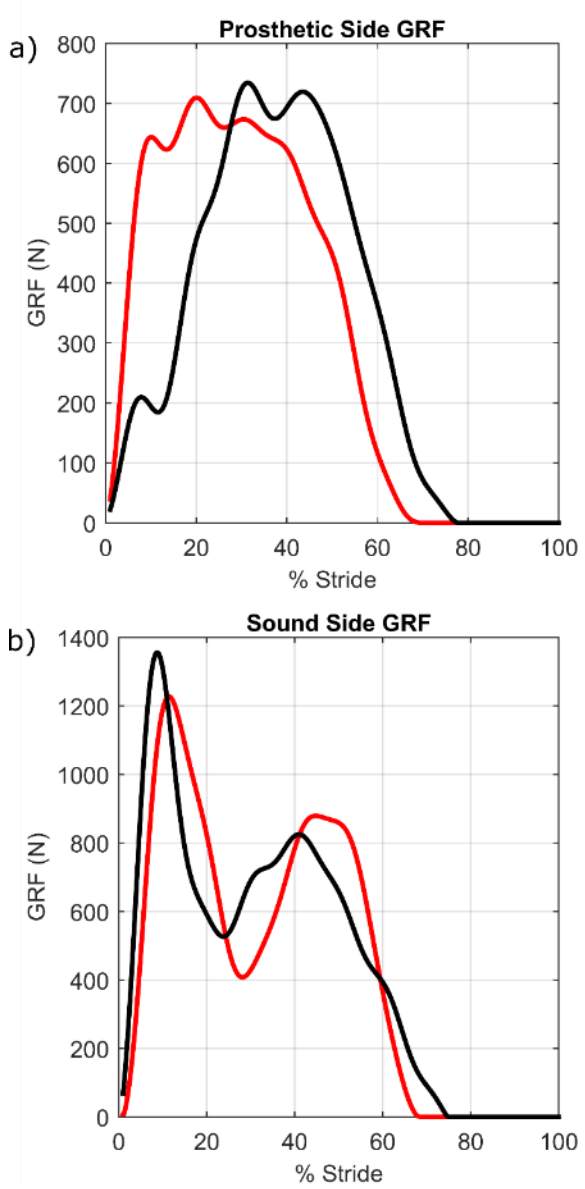

Fig. 3.9: Average ground reaction force magnitudes on the prosthetic side (a) and sound side (b) for the semi-powered prosthesis (black) and daily-use prosthesis (red).

Additionally, the energy dissipated by the ankle during descent was calculated for each of the experimental conditions, as shown in Fig. 3.10.

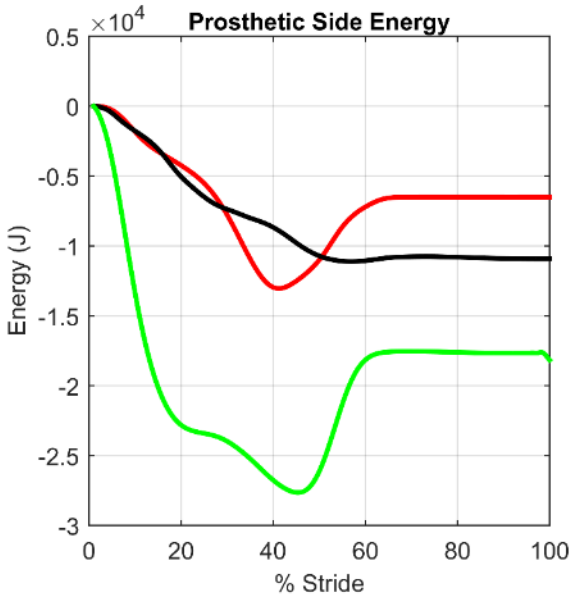

Fig. 3.10: Average energy dissipated during a stair descent stride for a semi-powered prosthesis (black), daily-use prosthesis (red), and healthy subjects (green).

Finally, Fig. 3.11 shows averaged ankle angle over five strides from the second stair geometry.

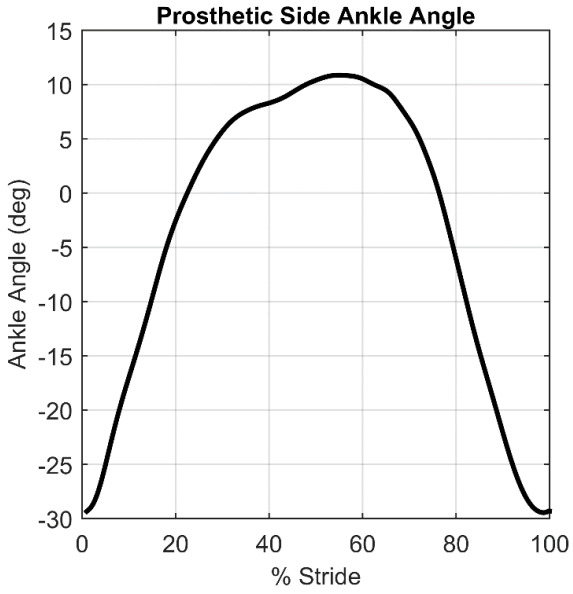

Fig. 3.11: Average ankle angle (five strides) from descending stairs with a different geometry from the instrumented staircase.

3.1.7 Discussion

As can be seen from Fig. 3.7, the semi-powered ankle provides the alternate dorsiflexion and plantarflexion characteristic of healthy stair descent, while the daily-use prosthesis does not. Namely, due to the passive, spring-like nature of the daily-use device, the ankle does not plantarflex during the swing phase. The dorsiflexion is initiated by contact with the stair (0% of stride) in a plantarflexed position, and is associated with a heavily damped behavior that lowers the user's heel to the stair tread and provides ankle stability during the first 50% of stride. The semi-powered ankle then plantarflexes the ankle joint in an effort to anticipate the subsequent foot strike.

The ankle torque across a stride is shown in Fig. 3.8. It should be noted from Fig. 3.8 that the semi-powered prosthesis exhibits the same double-hump shape of the healthy curve. The magnitude of the first torque peak, however, is much lower in magnitude than that of the healthy curve. This reduction in magnitude may have been due to the hydraulic damping valve being positioned such that not enough damping was provided to the user. The damping properties of the ankle were tuned to the subject's preference, and as such, the subject may have been attempting to achieve other objectives such as minimizing socket discomfort. It should also be noted from Fig. 3.8 that the semi-powered prosthesis torque curve and the healthy torque curve peak at approximately the same portion of a stride while the daily-use device experiences a torque peak out of phase with the other curves. All three curves show a decrease in ankle torque at approximately the same point in stride (as the user enters swing phase), indicating a similar stance and swing time ratio for both devices.

The plantarflexive position of the ankle at terminal swing (Fig. 3.7) allows the ankle to absorb the shock of the subsequent stair contact. This shock-absorbing effect can be seen

in Fig. 3.9a in which the prosthetic side ground reaction force magnitudes are plotted for both the daily-use and semi-powered device. It should be noted from Fig. 3.7 that the loading rate is significantly different across these two devices with a maximum loading rate of 9.6 kN per percent stride (762 kN/sec) and 4.9 kN per percent stride (301 kN/sec) for the daily-use and semi-powered prostheses, respectively (61% decrease in loading rate with respect to time). This rate difference is shown with the impulsive loading associated with the daily-use device as compared to the gradual loading of the semi-powered device. It should be noted that many studies have linked high loading rates to bone degeneration/injury [69-73]. The sound-side ground reaction force magnitudes are shown in Fig. 3.9b. As can be seen from this figure, the sound-side forces are very similar between the two devices. Overall, the semi-powered device decreases the ground reaction force rate of the prosthetic side without having a discernable effect on the sound side forces.

Fig. 3.10 shows the energy dissipated by the ankle during stair descent. As can be seen in Fig. 3.10, the healthy ankle dissipates more energy per stride than the prostheses at 1.76 J. The semi-powered and daily used ankles dissipated 1.1 J and 0.65 J, respectively. The semi-powered ankle did not dissipate as much energy as the healthy ankle, possibly due to the lower-than-optimal damping setting that may have been applied to the device as previously discussed. The semi-powered ankle does, however, dissipate substantially more energy than the daily-use device. Because the daily-use device is essentially a leaf spring, it's limited in its ability to dissipate power (i.e., dissipation is due strictly to inefficiencies in the spring).

The stair descent controller was designed such that the prosthesis can descend stairs of different geometries. This is demonstrated in Fig. 3.11. As can be noted from Fig. 3.11,

the semi-powered prosthesis was able to perform similarly on this staircase as it did on the instrumented staircase (Fig. 3.7). When comparing the ankle kinematics for these two staircases, it can be seen that the maximum dorsiflexion angle reached on the instrumented staircase (approximately 16 degrees) is different than that reached on the second staircase (approximately 11 degrees). This is due the steeper descent associated with the pitch of the first staircase. Nonetheless, the ankle controller is able to accommodate this change in geometry without altering controller settings. This is accomplished by designing the transitions between the stance and swing states (State 0 to 1 and State 2 to 0 transitions) to be load-based, thereby minimizing the effect of stair geometry on transitions.

Finally, as discussed in the introduction of this paper, a major motivation for the device described here is the ability to provide stair descent functionality in a smaller and lighter device, relative to a fully-powered prosthesis. In that regard, a powered transtibial prosthesis previously described by the authors [13] has a mass of 2.7 kg, while the device described here, which provides similar stair descent functionality using a different means to do so, has a mass of 1.4 kg. As such, although the devices are not equivalents, the semi-powered device is able to provide essentially the same stair descent functionality as the fully-powered device with approximately half the mass.

3.1.8 Conclusion

This paper presents the design and single-subject assessment of a semi-powered transtibial prosthesis and associated controller for stair descent. Testing on the single amputee subject suggests that the semi-powered prosthesis may provide benefit to the user relative to commonly-used passive prostheses. Specifically, the semi-powered device and

controller provided a reduction in prosthetic-side ground reaction force loading rate, and increased energy dissipation relative to the daily-use prosthetic device, both of which better match the characteristics of the healthy ankle during stair descent. Additionally, for users who prefer improved symmetry of gait, the semi-powered device provided a movement kinematics that closely reflects that of healthy stair descent.

Chapter 4

Design and Characterization of a Constant-Volume Hydraulic Actuator

The semi-powered ankle utilizes a single-rod hydraulic actuator, which necessitates the use of a hydraulic accumulator to accommodate volume changes in the hydraulic cylinder as a function of piston stroke. The use of a non-constant-volume hydraulic cylinder imposes some functional limitations on the ankle prosthesis that preclude its ability to lock or dissipate substantial power in both the dorsiflexion and plantarflexion directions. To address these limitations while attempting to simultaneously minimize the size of the ankle prosthesis, a single-rod constant-volume hydraulic actuator was developed and is presented here. This work was performed by a visiting summer undergraduate student, Beau Johnson, under my advisement. This manuscript was submitted to the *International Journal of Fluid Power* and is currently under review.

4.1 Manuscript 3: Design and Characterization of a Five-Chamber Constant-Volume Hydraulic Actuator

4.1.1 Abstract

This paper describes a new design for a constant-fluid-volume, also known as a symmetrical, hydraulic cylinder. Rather than the two fluid volume chambers of a typical hydraulic cylinder, the constant-fluid-volume cylinder contains five potential fluid chambers. Relative to a three or four chamber design, both previously described in the engineering literature, the five-chamber design enables a minimum-diameter solution with a simpler porting implementation. Following a general description of the five-chamber design and its motivation, a five-chamber cylinder prototype is described and presented.

Experimental results are presented comparing some behavioral characteristics of the five-chamber cylinder to a double-rod cylinder, and to two variations of single-rod implementations. Finally, a minimum-diameter five-chamber cylinder variant is described, and its geometric characteristics compared to an equivalent double-rod cylinder implementation.

4.1.2 Introduction

Hydraulic actuation systems provide among the highest force and power density of any actuator. Among the most commonly used hydraulic actuators is the single-rod hydraulic cylinder. Such cylinders are often employed in an actuation system that includes a pump, accumulator, and reservoir, along with a separate directional control valve for each cylinder. In this type of system, the pump and accumulator together provide a pressure source, and the directional control valve meters hydraulic fluid between the pressure source and one side of the hydraulic cylinder, and between the opposing side of the cylinder and the reservoir, from which the pump draws hydraulic fluid. For purposes of this paper, this type of hydraulic system is considered an "open" hydraulic system, since the reservoir is able to accommodate the variable fluid volume associated with movement of the single-rod cylinder (i.e., the amount of fluid in the reservoir will increase when the cylinder is fully retracted, and will decrease when it is fully extended).

In contrast to open-type hydraulic systems, some hydraulic actuators operate within a "closed" hydraulic system, in which the system does not include a fluid reservoir, and therefore is not able to directly accommodate fluctuations in fluid volume. A common closed-type hydraulic actuation system is a hydrostatic transmission [74, 75], which typically employ rotary piston pumps and motors in a closed hydraulic system to transmit (rotational)

shaft power between a hydraulic pump and motor. Since rotary piston pumps and motors are constant-volume hydraulic elements, no accommodation of variable fluid volume is required.

Although rotary-type hydrostatic actuation systems are common, a similar "closed" system approach can also be applied to linear actuation systems. Such systems can offer potential advantages relative to open-type linear actuation systems, such as the potential for greater efficiency and better leveraging of electrical power distribution, combined with the force density of hydraulic cylinders. Discussion of the framework and characteristics of such systems is given by Habibi [13-15]. As described in these references, due to the absence of a fluid reservoir in a closed system, an important component of a hydrostatic actuation system is a "symmetrical actuator," which is a hydraulic actuator characterized by a constant fluid volume as a function of stroke. This type of actuator is referred to as a "constant-volume hydraulic actuator" (CVHA) here, since the amount of fluid contained within the actuator must always be constant over the full cylinder stroke.

The most common CVHA is a double-rod cylinder, which mirrors the piston rod about the piston, such that a cylinder rod extends from the piston through each end of the cylinder and maintains a constant fluid volume over the stroke. Although this type of cylinder provides constant fluid volume, it also requires a design envelope that must accommodate the stoke length of the piston extended symmetrically on both sides of the cylinder, and thus requires a considerably larger design envelope, relative to a single-rod cylinder, for the same nominal output characteristics. Additionally, fewer options are available with respect to mounting such a cylinder, particularly since bending moments on the piston rods must generally be avoided. A rodless cylinder is another cylinder configuration that provides a

constant fluid volume. Rather than use a piston rod that extends axially through the end of the cylinder to transmit power to an external point of attachment, a rodless cylinder incorporates a carriage attached to the piston laterally through the wall of the cylinder. This configuration provides constant fluid volume, but the nature of sealing along the length of the cylinder limits its use to very low pressures, relative to rod-type cylinders. As such, performance with rodless cylinders is compromised substantially, relative to rod-type cylinders. Another cylinder configuration that provides constant fluid volume is a tandem cylinder configuration [76], which employs a pair of single-rod cylinders in which the rod side of one cylinder is in fluid communication with the non-rod side of a duplicate cylinder. Given this configuration, retraction of the rod in one cylinder is accompanied by extension of the rod in the other cylinder, and the coupled motion results in a constant fluid volume. In this configuration, only one of the two cylinders is used for actuation, while the other is used strictly to maintain a constant fluid volume, and as such, this configuration effectively doubles the size and weight of the actuator.

4.1.3 Constant Volume Single-Rod Cylinder

In order to provide a constant fluid volume linear actuator without the size, weight, packaging, and/or performance penalties associated with the aforementioned actuators, researchers have proposed alternative CVHA designs. Among the unifying aspects of these designs is the fact that, rather than two fluid chambers as is characteristic of typical hydraulic cylinders, these designs incorporate multiple fluid chambers. Specifically, previously-published multi-chamber cylinders contain either three fluid chambers (i.e., the designs described by Habibi [13-15] and Pastrakuljic [16]) or four (i.e., the designs described by

Linjama et al [17, 18], Heybroek and Norlin [19] and Wu et al. [20]). Figure 1 (a) and (b) schematically depict the designs of the three and four chamber hydraulic cylinders, respectively. Note that, although a subset of the three or four chambers can be pressurized, implementation of these designs as a CVHA is subject to the following two essential symmetry conditions: 1) pressurization of at least one chamber must extend the piston rod, while pressurization of at least one other chamber must retract it; and 2) the effective area on the extension portion of the piston must equal the effective area on the retraction portion. For example, for the three-chamber design in Fig. 4.1(a), only chamber 2 retracts the rod, and therefore chamber 2 must always be used. Although both chambers 1 and 3 extend the rod, it is not physically possible to establish equal piston areas between chambers 1 and 2 (due to the piston rod), since the area 1 will always be greater than area 2. As such, the only valid (two-pressure) combination is to use chamber 3 to extend the rod and 2 to retract it (while chamber 1 is left vented to atmosphere), where the piston and cylinder are designed such that piston areas exposed to chambers 2 and 3 are equal. In the case of the four-chamber cylinder (Fig. 4.1(b)), the summation of areas of 2 and 4 (the retraction chambers) will always be less than area 1, and therefore (as in the three-chamber design) chamber 1 cannot be used. As such, chamber 3 must be used for extension, and retraction can either be restricted to either chamber 2 or chamber 4, or the combination of the two. Employing the combination of the two will enable a smaller overall cylinder diameter, since it more completely fills the rod-side of the piston with fluid. Specifically, in addition to the conditions for symmetry previously stated, in order to provide a minimum-diameter solution, the rod-side of the piston must be fully filled with pressurized fluid. Such is the chief advantage of a four-chamber design relative to the three-chamber design (i.e., smaller

achievable theoretical diameter). This theoretical advantage, however, requires a more complex porting geometry, since simultaneous access to both chambers 3 and 4 in a compact space is a challenge (i.e., these ports would most likely be located in the center of the cylinder, which increases the cylinder diameter). As such, the theoretical advantage of the four-chamber design relative to the three-chamber design may not be realized, depending on the nature of the application.

This paper proposes a new CVHA cylinder design, shown in Fig. 4.1(c),that incorporates five chambers. The inclusion of five chambers enables a combination of chambers that satisfies both the symmetry conditions of a CVHA, and satisfies the minimum diameter condition for a CVHA, without requiring use of chamber 3, which alleviates substantial challenges associated with porting. Specifically, meeting the minimum diameter criterion requires the use of chambers 2 and 4. Unlike the three and four chamber designs, however, the symmetry requirement can be satisfied using strictly chamber 1 to balance the piston area associated with chamber 2 and 4, and therefore chamber 3 need not be used. The result is a minimum diameter design with relatively simple porting, as described subsequently in this paper.

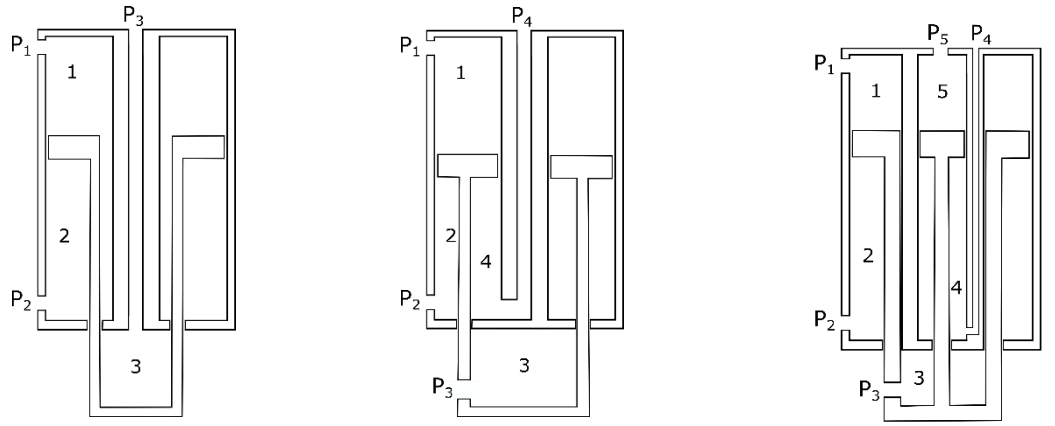

(a) (b) (c)

Fig. 4.1. Schematic diagram of multi-chamber constant-fluid-volume linear cylinder actuators, specifically: a) three-chamber cylinder; b) four-chamber cylinder; and c) five-chamber cylinder as described here

This paper presents two variations of the novel 5-chamber cylinder design: a "simplest porting" configuration, and a "minimum-diameter" configuration. A prototype of the simplest-porting variation was constructed, and experiments were conducted to validate the behavioral characteristics of the actuator, relative to standard single-rod and double-rod cylinder configurations. Following presentation of the experimental results, the minimum-diameter design variation is described, and the resulting cylinder size is compared to that of a single-rod cylinder, and to the simplest-porting variation of the 5-chamber actuator.

4.1.4 Prototype Five-Chamber Cylinder Design

In order to experimentally validate the five-chamber concept, a five-chamber CVHA was designed, fabricated, and experimentally tested. Since multiple variations of the five-chamber design meet the aforementioned symmetry requirement, the authors selected as an initial prototype the simplest-porting variation – specifically, a variation that uses only two chambers (chambers 2 and 5), each of which can be accessed via a standard cylinder port

configuration (i.e., one port in each end of the cylinder body).

This cylinder variation is shown schematically in Fig. 4.2(a), and as a solid-model design in Fig. 4.2(b). As shown in the figures, the CVHA consists of a cylinder nested concentrically inside another cylinder, along with a piston and rod assembly that moves axially within the cylinders. Rather than a simple piston, as in a typical single-rod cylinder, the piston assembly in the CVHA actuator includes a piston arranged concentrically within another piston. The inner piston has a circular cross section and moves inside the inner cylinder, while the outer piston is annular such that it moves between the inner and outer cylinder. Note that end caps are sealed with O-rings, while the piston and rod seals employ U-cup seals to reduce sliding friction. Since chambers 1, 3, and 4 were not used, vent holes in those chambers vent the respective volumes to atmosphere.

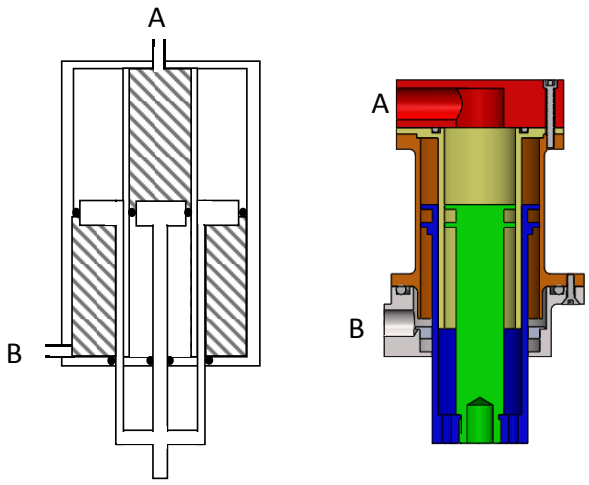

(a) (b)

Fig. 4.2. (a) Schematic depiction of the five-chamber CVHA cylinder in a "simplest porting" configuration, where the shaded regions indicate volumes that are filled with hydraulic fluid, and non-shaded regions indicate chambers vented to atmosphere. (b) Solid model of the corresponding prototype actuator, where A and B indicate complementary fluid ports. The inner piston and rod is shown in green and was fabricated separately from the annular outer piston and rod shown in blue. The inner cylinder is shown in yellow, and the outer cylinder in orange. The cylinder endcaps are shown in red and grey, respectively.

In order to compare the cylinder characteristics to a standard-sized cylinder, the dimensions of the prototype were selected to match the maximum actuation force of a 1.9 cm (0.75 in) inside-diameter hydraulic cylinder with an approximate stroke length of 4.4 cm (1.75 in). As such, the prototype was designed with an inner-cylinder bore of 1.9 cm (0.75 in) and an outer-cylinder bore of 3.2 cm (1.26 in), which resulted in a total outer-diameter of the CVHA of 3.4 cm (1.34 in). The resulting actuator prototype was fabricated from 7075 aluminum, and is shown assembled in the retracted and extended positions, respectively, in Fig. 4.3.

(a) (b)

Figure 4.3. Functional CVHA prototype in (a) retracted and (b) extended configurations.

4.1.5 Experimental Characterization

The behavior of the five-chamber CVHA prototype was characterized and compared

to three other hydraulic actuator configurations (i.e., a total of four configurations), each under two experimental conditions. The four configurations tested, shown in Fig. 4.4 (a-d), are as follows: a) standard double-rod cylinder; b) standard single-rod cylinder; c) standard single-rod cylinder with accumulator on rod-side of piston; and d) the five-chamber CVHA prototype. All cylinders had an effective cylinder bore of 1.9 cm (0.75 in) diameter and approximately 4.4 cm (1.75 in) stroke. In the experiment, for each cylinder configuration, the two cylinder fluid ports were connected using rigid (i.e., steel) tubing, with a ball valve positioned in between the two ports, as shown in the schematics of Fig. 4.4. The test setup for the CVHA case is shown in Fig. 4.5. Given this setup, the cylinder force-displacement relationship was measured under two test conditions: 1) the cylinder ports connected with the ball valve open, and 2) the cylinder ports connected with the ball valve closed. For a constant-volume cylinder, the first condition (ball valve open) should allow free movement of the cylinder rod throughout the cylinder stroke, and as such the ideal force-displacement relationship would be zero force through the range of motion. The second condition (ball valve closed) corresponds to what is commonly called a "hydraulic lock," where the desired behavior is to be locked against motion in both directions. As such, the two experimental conditions are essentially complements: the first should produce (approximately) zero force, while the second should provide (approximately) zero motion.

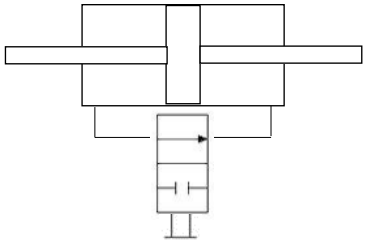

(a)

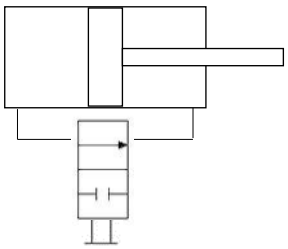

(b)

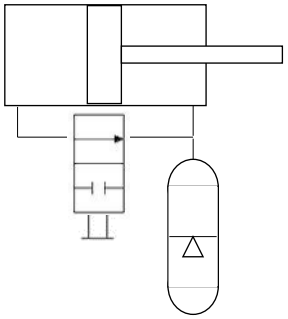

(c)

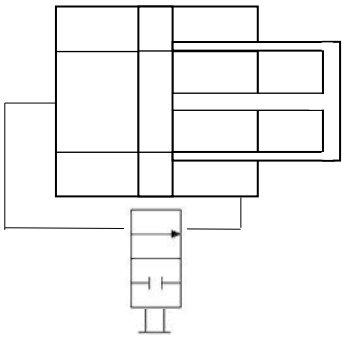

(d)

Fig. 4.4. Schematic diagrams of four hydraulic actuator configurations used in experimental comparisons: (a) double rod cylinder, (b) a single rod cylinder, (c) singe rod cylinder with accumulator attached to the rod end, and (d) five-chamber CVHA. All cylinders were tested under two conditions: 1) ball valve open, and 2) ball valve closed.

Fig. 4.5. CVHA shown in closed test circuit with ball valve in between cylinder ports. The capped connected shown was used for filling, but sealed off during the experimental characterization.

In order to measure the force-displacement relationship for each, a test setup was constructed using a string potentiometer (Space Age Controls L021-00) to measure actuator displacement, and using a load cell (Transducer Techniques MLP500) in series with the actuator to measure force. Forces were applied bidirectionally to the actuator rod manually using a lever press connected to each cylinder rod. For the valve-open (VO) test condition, the lever press was used to incrementally move the rod through its range of motion in approximately 4 mm increments, stopping to measure displacement and force at each increment. This process was repeated throughout the range of motion, or until the load cell measured 500 N, whichever came first. Note that taking the measurements at zero velocity avoided viscous damping effects. This process was repeated for three cycles of measurement (i.e., three actuator strokes). For the valve-closed (VC) test condition, the piston was started in the center of the stroke when the ball valve was closed, and the lever press was subsequently used to apply forces bidirectionally in approximately 50 N increments, up to

500 N. This process was repeated for three cycles. For each test condition, the displacement and force measurements were recorded by an oscilloscope, saved to digital storage media, and were subsequently plotted using MATLAB.

4.1.6 Results

The experimental results for each case shown in Fig. 4.4 and for both the VO and VC test conditions are shown in Fig. 6, with force plotted on the vertical axis and position plotted on the horizontal axis. Positive force values indicate tensile rod force and negative forces indicate compressive force. The middle of the stroke for each cylinder corresponds to a position of zero, such that positive displacement values represent extension and negative displacement values represent retraction.

As shown in the top row, the double-rod cylinder is characterized by near ideal constant-volume behavior (i.e., near zero-force in the VO condition, and near zero-displacement in the VC). Note that the cylinder differs only slightly from the ideal, due to seal friction in the VO case, and due to fluidic, structural, and seal compliance in the VC case. The second row in Fig. 4.6 shows the results of the same tests performed on the single-rod cylinder. In this case, as shown in the VC case (second column), the single-rod cylinder provides a near ideal hydraulic lock behavior. As shown in the first column, however, due to the non-constant-volume (i.e., non-symmetric) nature of the single-rod cylinder, it fails to provide appropriate zero-force behavior in the VO case. Rather, in the rod retraction direction the cylinder is essentially locked, since the rod volume cannot be introduced into the closed volume of the fluid circuit. The rod is able to move in the rod extension direction, although doing so creates a vacuum in the fluid that acts to pull the rod towards the zero

position. As such, the single-rod is unable to provide appropriate constant-volume behavior. The problem of variable fluid volume can be accommodated via use of an accumulator on the rod-side of the cylinder, as illustrated in Fig. 4.4(c), which is the configuration tested in the third row of Fig. 4.6. In this case, under the VO condition, the rod is able to move throughout the stroke with near ideal (i.e., zero-force) behavior, since the accumulator accommodates the change of fluid volume introduced by the piston rod. As seen in the second column, however, the system is unable to provide a bidirectional hydraulic lock in the VC case. Rather, the system is able to provide a hydraulic lock against retraction, but can at most sustain a vacuum against rod extension. Finally, the last row in Fig. 4.6 shows the VO and VC cases for the five-chamber CVHA prototype. As can be seen in the figure, the CVHA prototype, like the double-rod cylinder, provides essentially ideal constant-volume behavior under both test conditions. A more direct comparison of the data comparing only the double-rod and CVHA results under both conditions is shown in Fig. 4.7. As seen in the figure, both provide essentially identical behavior, different from the ideal only in seal friction for the VO condition, and system compliance for the VC condition.

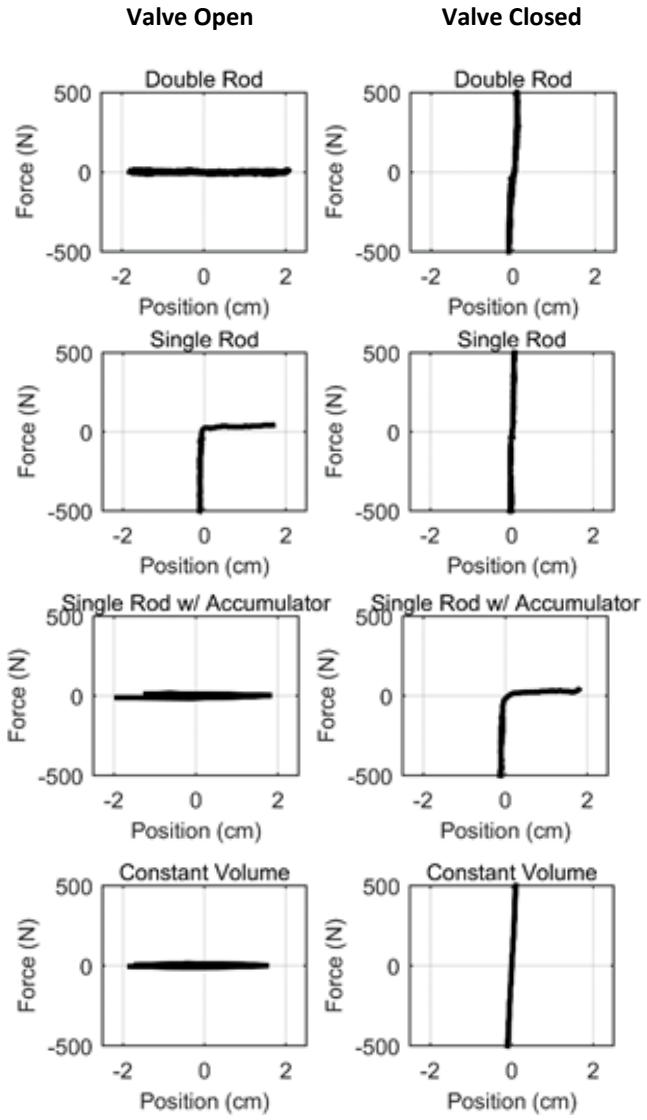

Fig. 4.6. Experimental force-displacement results for each test configuration shown in Fig. 4.4, under both valve open and valve closed test conditions.

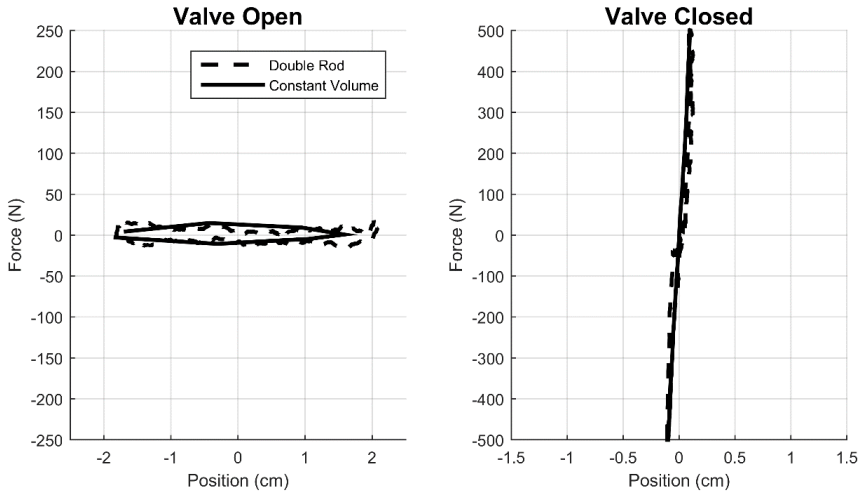

Fig. 4.7. Direct comparison of double-rod cylinder and CVHA configurations under both VO and VC test conditions.

4.1.7 Discussion

4.1.7.1 *Test Results*

As shown in the data of Fig. 4.6, the single-rod variants are unable to provide appropriate constant-volume behavior. Specifically, although an accumulator allows the free motion condition desired in the VO test condition, it precludes a bidirectional hydraulic lock in the VC condition. Although the accumulator case tested here was an atmospheric accumulator, one could alternatively use a gas-charged or spring-charged accumulator. Doing so would improve the behavior in the VC condition, but at the cost of compromising the behavior in the VO condition. As the accumulator stiffness increases from zero (as tested) to ideally infinite, the behavior of the single-rod system with accumulator transitions from the second row in Fig. 4.6 to the first, where the ideal VC behavior is restored as the ideal VO behavior is lost.

As shown in Fig. 4.7, the CVHA and double-rod behaviors are essentially identical. Therefore, the primary difference between these two actuators is the geometric envelope

each requires, and the associated mounting conditions. Specifically, the CVHA design requires an increased diameter relative to its single-rod counterparts, but requires substantially less axial length than an equivalent double-rod cylinder, and also enables in most cases simpler mounting arrangements.

4.1.7.2 *Minimum-Diameter Design*

Recall that the five-chamber CVHA prototype was configured using chambers 2 for retraction and 5 for extension, since that configuration was relatively simple to implement, and thus selected for the experimental proof of concept. As previously mentioned, however, that variation does not satisfy the minimum-diameter criterion, which requires that the rod-side of the piston be fully filled with pressurized fluid. Doing so requires the use of both chambers 2 and 4 for retraction, which in the five-chamber design can be balanced by using chamber 1 for extension, as illustrated schematically in Fig. 4.8. In order to compare the relative sizes of the double-rod and five-chamber CVHA designs, this minimum-diameter configuration is considered. In this configuration, chambers 2 and 4 are in fluid communication, which is enabled by: 1) ports between chambers 2 and 4 near the rod seals and 2) ports in the outer piston rod near the piston. Note that, alternatively, the outer piston rod can be constructed from several different rods, rather than a single annular rod. Configuring the chamber 1 piston area to equal the combined chambers 2 and 4 piston area will satisfy the symmetry condition and provide CVHA behavior. A cylinder of the same fluid dimensions as those tested (i.e., effective bore of 1.9 cm (0.75 in) and stroke of 4.4 cm (1.75 in) can be constructed with this design with an outer bore diameter of 2.1 cm (0.83 in). By comparison, the proof-of-concept prototype shown in Figs. 2 and 3 required an outer bore

diameter of 3.2 cm (1.26 in). The theoretical design envelope differences can be compared by considering the outer diameter bore and the total stroke length. For a 1.9 cm (0.75 in) bore, 4.4 cm (1.75 in) stroke cylinder, the double-rod cylinder has a bore of 1.9 cm (0.75 in) and swept stroke length of 8.8 cm (3.5 in), while the minimum-diameter configuration CVHA has a bore of 2.1 cm (0.83 in) and swept stroke length of 4.4 cm (1.75 in). As such, in terms of profile, the double-rod requires 16.7 cm^2 (2.59 in^2) while the CVHA requires 9.2 cm^2 (1.43 in^2). In terms of swept volume, defined as the actual cross-section swept through the rod movement, the double-rod requires 24.9 cm^3 (1.52 in^3), while the CVHA requires 15.2 cm^3 (0.93 in^3). As such, for this design, the CVHA requires approximately 55% of the profile and approximately 61% of the swept volume. Therefore, it is reasonable to assert that there may be several applications for which the CVHA design provides a substantially more compact solution, relative to a double-rod cylinder. The increased compactness, however, is obtained via the increased design complexity of the CVHA, and the likely increased cost to produce it.

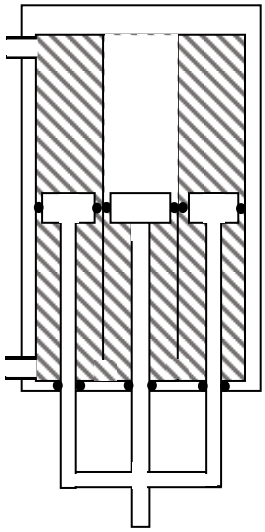

Fig. 4.8. A schematic representation of a minimum-diameter variation of the five-chamber CVHA actuator.

4.1.8 Conclusion

The authors have presented a new five-chamber hydraulic cylinder design that provides symmetrical (i.e., constant-volume) behavior in a single-rod package. One variation of the actuator was constructed and experimentally shown to provide the same constant-volume behavior as a double-rod cylinder. For the cylinder dimension tested, if constructed using a minimum-diameter variation of the five-chamber actuator, the resulting package was shown to be substantially smaller in terms of profile area and total swept volume, relative to an equivalently-size double-rod cylinder.

Chapter 5

Semi-Powered Ankle Redesign, Sloped Walking, and Sloped Standing

The semi-powered ankle as presented in Chapter 2 was redesigned to include a single-rod constant-volume hydraulic actuator as presented in Chapter 5 in order to address some of the functional limitations of the prior design. This redesign is presented in this chapter. The revised ankle hardware was then utilized for the design and assessment of controllers for sloped walking as well as sloped standing. Specifically, a slope-adaptive controller was designed leveraging observations from healthy sloped walking gait. The developed controller allows for the semi-powered ankle to accommodate walking across various slopes without explicitly measuring the local or global ground slope. Namely, the controller was designed such that no controller parameters need to be modulated as a function of the ground slope. Additionally, a sloped-standing controller was also developed that provides standing support to the user across various ground slopes by explicitly adapting the ankle of the ankle to the ground slope. These controllers were assessed relative to a passive carbon-fiber prosthesis on a single transtibial amputee subject.

5.1 Semi-Powered Ankle Redesign, Sloped Walking, and Sloped Standing

5.1.1 Semi-Powered Ankle Mechanical Design Iteration

As described in Chapter 4, in a closed hydraulic system, the use of a single-rod cylinder introduces performance limitations relative to the use of a constant-volume actuator. The linear actuator described in Chapter 2 suffers from such limitations. Recall from Chapter

2 that the hydraulic aspect of this actuator consists of a single-rod cylinder with a two-way variable damping valve connecting the two chambers of the cylinder. Additionally, the system utilizes an accumulator connected to the rod side of the cylinder. Per the discussion of single-rod actuator limitations presented in Chapter 4, an actuator such as this is able to move freely when the valve is open, but the actuator can only lock in the direction of cylinder retraction. In the direction of cylinder extension, this actuator is only able to resist motion with the force generated by atmospheric pressure acting at the accumulator. Consequently, the actuator presented in Chapter 2 is not an ideal power-asymmetric actuator in that it can only dissipate large amounts of power in a unidirectional fashion.

This linear actuator limitation imposes constraints on the capabilities of the ankle prosthesis. Namely, the ankle is able to lock in the dorsiflexion direction, but is only able to resist motion in the plantarflexion direction with a small amount of torque. With regard to activities of daily living, dissipating power and/or locking in the dorsiflexion direction is more prevalent than that of dissipating power and/or locking in the plantarflexion direction. The ankle should, however, be able to provide a resistive torque in the plantarflexion direction during the heelstrike and ground conformation events of walking. This phase of gait is sometimes called "controlled plantarflexion," and without the capability to resist large torques in the plantarflexion direction, the ankle prosthesis as previously presented has limited control authority. Additionally, the ankle should be able to provide resistive torques in both the dorsiflexion and plantarflexion directions during quiet standing in order to provide stability to the user.

The ankle's performance limitations may be addressed by utilizing a constant-volume hydraulic cylinder instead of the single-rod cylinder and accumulator. As discussed

in Chapter 4, a constant-volume hydraulic cylinder is able to lock in both directions, thereby eliminating the existing performance limitations of the previously presented ankle prototype. To integrate a constant-volume cylinder into the ankle actuator design, it must be able to accommodate a small electromechanical drive system in parallel with the hydraulic system. By using the constant volume cylinder configuration as seen in Fig. 4.8, the lead screw transmission can be placed collinear with the cylinder by positioning the lead screw within the central bore (inner-most chamber) on the non-rod side of the cylinder. Positioning the lead screw within this chamber also allows for the electromechanical drive system to be isolated from any cylinder chambers containing hydraulic fluid. This fluid isolation allows the motor and transmission to remain dry and removes some of the mechanical complexity associated with passing electrical signals across an interface that must remained sealed to high pressures. Additionally, the cylinder configuration in Fig. 4.8 achieves the minimum diameter criteria as described in Chapter 4, allowing for a compact design envelope. A schematic of the constant-volume power asymmetric actuator is shown in Fig. 5.1.

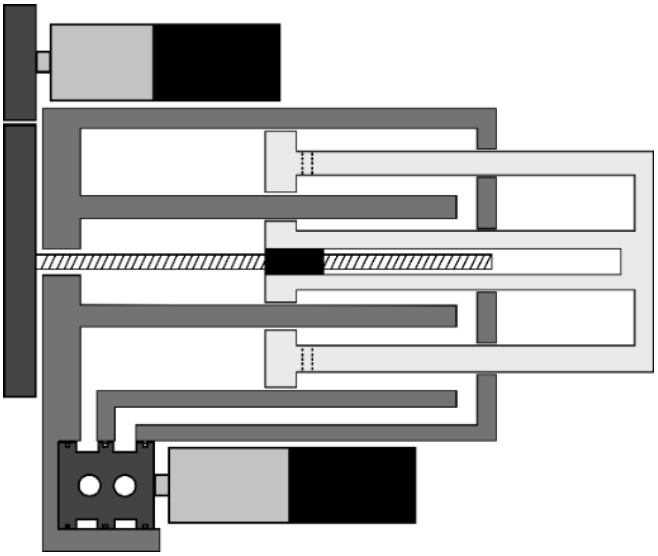

Fig. 5.1. Schematic of constant-volume power asymmetric actuator illustrating the single rod, cylinder housing, damper valve and associated motor, and electromechanical transmission with associated motor. The lead screw of the transmission is concentric with the central bore of the cylinder.

The schematic shown in Fig. 5.1 was designed, built, and implemented in the preexisting structure of the ankle. The constant-volume version of the actuator was designed and fabricated in conjunction with Dr. Brian Lawson. This iteration of the ankle was designed to provide bidirectional power dissipation and locking while maintaining a compact design envelope. This iteration of the actuator was able to fit within the preexisting ankle structure while simultaneously increasing the cross sectional area of the cylinder, thereby decreasing the maximum system pressure. The effective cross sectional area of the new hydraulic cylinder is 3.7 cm^2 as compared to the previous cylinder's cross sectional area on the non-rod side of 2.6 cm^2. The new iteration of the actuator also includes changes to the electromechanical transmission including a modification to the helical gear transmission ratio (2.4:1 as opposed to 2.25:1 in the previous design iteration) and a different lead screw (with the same travel distance per rotation as the screw utilized in the previous iteration). The prosthetic ankle with installed constant volume power asymmetric actuator is shown in

Fig. 5.2.

Fig. 5.2. Photograph of semi-powered prosthetic ankle with constant-volume power-asymmetric actuator installed

5.1.2 Sloped Walking and Standing Introduction

The current standard of care in ankle prostheses is the fixed angle stiffness (FAS) prosthesis. These devices are designed to replicate the passive stiffness-like properties of the healthy foot and ankle during the mid-stance phase of level ground walking. These FAS devices are passive, however, and cannot modulate their behavior across tasks commonly encountered outside of the laboratory, such as slopes. For example, when walking or standing on slopes, FAS prostheses remain configured for level ground walking, and as such, can provide inappropriate behavior on such terrain. When walking up slopes, the FAS prosthesis is nominally configured at a right angle (zero degrees dorsiflexion) and tends to "fight" the user's movement during the stance phase. When walking down slope, an FAS prosthesis similarly provides inappropriate behavior. When standing on an up or down slope,

the FAS prosthesis may provide a disturbance torque if the user fully loads the device with their body weight. Alternatively, the user may choose to offload their FAS prosthesis while standing on slopes to avoid such disturbance toques; such a strategy was observed in [64, 77].

It has been suggested that by adjusting the equilibrium position of a passive prosthesis based on the ground slope may allow for the ankle to provide appropriate behavior across slopes, especially with regard to sloped walking [78, 79]. This idea was proposed by Hans Mauch in the late 1950's when he developed a passive hydraulic ankle that was able to adapt to slopes with each step [80]. The ankle relied on a passive mechanism to "lock" when the shank became vertical, but the mechanical design suffered from leakage issues and was eventually abandoned. In the modern era of prostheses, microprocessor-controlled devices have gained attention with many research groups developing devices that are able to modulate their passive behavior using sensors and actuators [28-30]. The behavioral adaptability that is provided by these microprocessor devices may allow for the passive behavior of an ankle to be adapted step-by-step in order to adapt to slopes.

Slope adaptability may be provided through the use of multiple controllers to be used for different values of the ground slope as well as a method of classifying the current stride into one of these discrete controllers. A classification approach such as this has been utilized for the control of a fully powered transfemoral prosthesis across level terrain and positive slopes [81]. Another approach may be to find qualities of healthy gait that are consistent or that vary continuously across various ground slopes and develop a single control policy for all ground slopes. This approach is proposed in [82] for the control of a powered transfemoral prosthesis. The work presented in [21] took a unified control policy approach to uneven

terrain walking with a powered transtibial prosthesis in which the idea of an external quasi-stiffness is presented and is shown to be consistent across local ground slopes in an uneven terrain environment.

This work is an extension of the ideas presented in [21] where the concept of external quasi-stiffness is leveraged to provide a unified control policy for a semi-powered prosthesis across slopes. This work presents the development and assessment of this controller on a single transtibial amputee subject across both up and down-slope terrain. The semi-powered ankle and slope-adaptive controller are assessed relative to the subject's daily-use prosthesis. Additionally, the semi-powered ankle is assessed while standing on various ground slopes relative to the subject's daily-use prosthesis.

5.1.3 Sloped Walking, Sloped Standing, and Activity-Level Control

In [21], it was shown that healthy subjects maintain a consistent external quasi-stiffness (slope of the ankle torque vs. shank angle plot) during the mid-stance phase of walking across uneven terrain, independent of the local ground slope. This insight was leveraged to develop a controller in which this external quasi-stiffness was virtually enforced via a control law implemented in a fully-powered transtibial prosthesis. This control law commanded ankle torque as an output given a sensed shank angle as an input. Additionally, this controller utilized software-tunable parameters for both the quasi-stiffness as well as the equilibrium position (shank angle at which zero ankle torque occurs). This controller also included a push off state in which the large motor and transmission deliver net positive power into the gait cycle.

The hardware and field of application of the work presented here required that the

concepts previously presented in [21] be modified and extended in order to prove useful with regard to sloped walking with a semi-powered prosthesis. Namely, this prior work was limited in scope to uneven terrain walking across globally level ground. The degree to which the external quasi-stiffness being conserved generalizes across globally sloped terrain is unknown. Additionally, the hardware used in this work is a semi-powered device. The fully powered prosthesis used in [21] had the control authority to specify shank-based quasi-stiffness as well as the shank-based equilibrium position via software. The semi-powered prosthesis used in this work is constrained to enforce a pre-specified stiffness (determined by the foot passive foot plate) about the ankle joint when the valve is fully closed. Additionally, the semi-powered ankle cannot enforce an arbitrary shank-based equilibrium position (as can be set in software in a fully powered prosthesis), and instead, must engage an ankle-based equilibrium position when the ankle is in that position. In other words, the equilibrium point of the spring cannot be arbitrarily set, but instead, the ankle can only set the ankle-based equilibrium point by locking the joint in its current position. These hardware and field-of-application differences preclude the adoption of the methods presented in [21].

In order to determine the degree to which the external quasi-stiffness is maintained across slopes, the averaged ankle torque for 10 healthy subjects was plotted against the averaged shank ankle over a normalized stride performed at 1 m/s. This process was repeated for trials recorded at slopes ranging from -6 to +6 degrees in 3 degree increments, and the resulting plot is shown in Fig. 5.3 (level walking plotted as a black dashed line). Trajectories in Fig. 5.3 begin at the left-most position on the plot and follow the curve from left to right with the torque fluctuating across the stance phase; once reaching the far right of the plot, the trajectory returns back to its starting position with a zero-torque swing phase. The initial

positive torque hump is associated with controlled plantarflexion, and the torque begins to become negative at the onset of the stance phase (approximately foot flat). As can be seen from Fig. 5.3, the trajectories for walking on these various slopes are fairly aligned, especially during stance (initial torque zero-crossing). Of particular note, is that these trajectories form a consistent external quasi-stiffness with approximately the same shank-based equilibrium angle (approximately zero degrees shank angle or aligned with the gravity vector) and quasi-stiffness. In other words, the healthy "slope-adaptive controller" attempts to leverage this consistency to allow for consistent and appropriate ankle functionality across slopes.

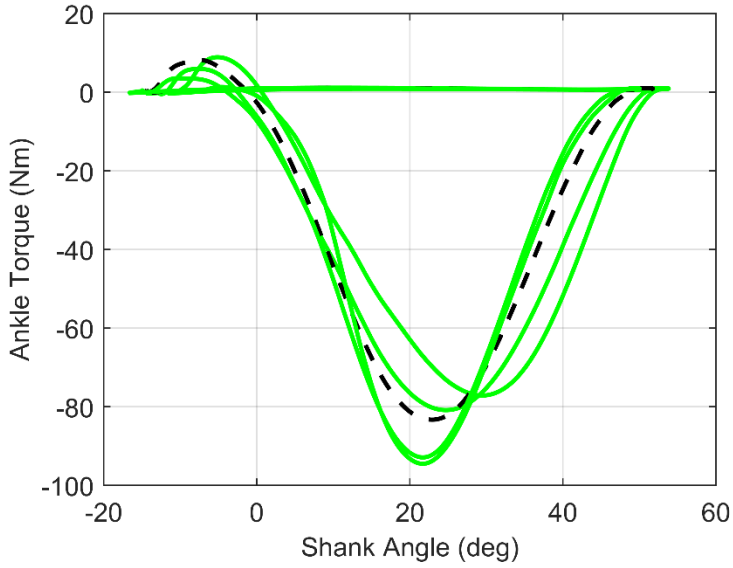

Figure 5.3. Ankle torque vs. shank angle for averaged across 10 healthy subjects for walking at 0.8 m/s across slopes ranging from -6 to +6 degrees in 3 degree increments. Level walking trajectory is plotted as a black dashed line.

In order to provide similar ankle behavior to that observed in the healthy subject data, a semi-powered prosthesis ankle controller can enforce a consistent external quasi-stiffness, as seen across slopes in healthy subjects, by properly engaging the ankle equilibrium spring. The ankle spring is engaged in the prosthesis by closing the variable damping valve as the

ankle passes through the appropriate angle such that the external quasi-stiffness is enforced. The ankle, however, only has control authority over the shank if the foot cannot move relative to the ground (foot is flat on the ground). If the foot is approximately flat on the ground during stance, then the ankle equilibrium angle that enforces the external quasi-stiffness is the ankle angle when the shank passes through the shank equilibrium angle (Fig. 5.4). As such, the slope controller is designed such that the variable damping valve closes after the foot is flat on the ground and when the shank passes through the pre-determined shank-based equilibrium angle (approximately aligned with the gravity vector).

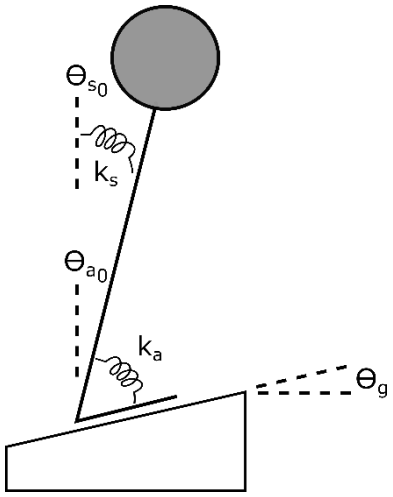

Fig. 5.4: Schematic of pendulum-like human walking up a slope that is angled at θ_g relative to level. The pendulum exhibits a virtual shank-based equilibrium position of θ_{s_0} and a shank-based stiffness of k_s. This virtual spring behavior may be emulated by a spring joint at the ankle with equilibrium angle and stiffness of θ_{a_0} and k_a, respectively, provided that the foot is flat on the ground.

The slope-adaptive walking controller was implemented as a finite state machine as depicted in Fig. 5.5. The transition conditions for this state machine are shown in Table 5.1. The state machine consists of four states: controlled plantarflexion (state 0), resistive dorsiflexion (state 1), lock (state 2), and swing (state 3). A stride begins at heel strike, when the controller is in the controlled plantarflexion state. During this state, the ankle is

configured such that the damping valve provides the appropriate heel strike damping as the ankle conforms to the ground. Once the shank angular velocity is positive and the foot is flat on the ground, as measured by near zero foot angular velocity for a short period of time, the controller transitions to the resistive dorsiflexion state (state 1). While in the resistive dorsiflexion state, the ankle provides a separately tunable level of damping that is typically higher than the damping from the previous state. Additionally, while in the resistive dorsiflexion state, the damping increases as the shank angle increases (becomes more aligned with the gravity vector). This gradual increase in damping allows the ankle torque trajectory to remain continuous in order to feel "smooth" to the user. Once the shank angle has reached a predefined threshold angle and the shank angular velocity is positive, the controller transitions into the lock state (state 2), at which point, the valve fully closes. During this state, the hydraulic actuator is locked, and the carbon fiber foot plate in series with the device dominates the ankle's dynamic behavior. The ankle exhibits this spring-like behavior during the stance phase of walking. Once the ankle has reached terminal stance, the ankle is unloaded as measured by the torque signal. After the ankle is unloaded, the device moves into the swing state (state 3), at which point, the valve fully opens and the ankle actively dorsiflexes. Once the ankle has dorsiflexed past a threshold angle, the controller transitions back to the controlled plantarflexion state (state 0) in preparation for the subsequent heel strike. This controller is designed to allow for walking on positive, negative, and neutral slopes without the identification of the ground slope and without adjusting any parameters across ground slopes.

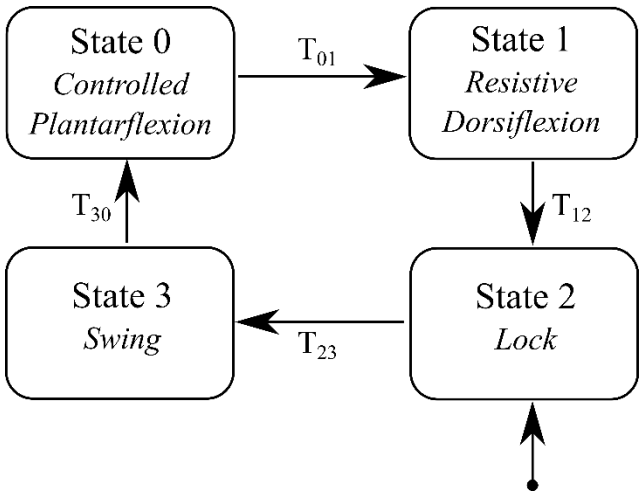

Fig. 5.5. Depiction of slope-adaptive finite state machine controller.

TABLE 5.1
FINITE STATE TRANSITIONS FOR THE SLOPED WALKING CONTROLLER

Transition	Description	Condition
T_{01}	Shank has positive angular velocity as the foot is flat on ground	$\dot{\theta}_s > 0$ $\dot{\theta}_f \approx 0$ for $t > t_{th,01}$
T_{12}	Shank crosses virtual equilibrium position and has positive angular velocity	$\theta_s > \theta_{th,12}$ $\dot{\theta}_s > 0$
T_{23}	Ankle is unloaded	$\tau_a < \tau_{th,23_2}$ after $\tau_a > \tau_{th,23_1}$
T_{30}	Ankle has fully dorsiflexed	$\theta_a > \theta_{th,30}$ $t_{ST} > t_{th,30}$

The sloped standing controller is also implemented as a finite state machine consisting of two states: one for dorsiflexion and one for plantarflexion. This finite state machine is depicted in Fig. 5.6 and its associated state transitions are listed in Table 5.2. If the ankle is plantarflexing, as measured by a sufficiently negative ankle angular velocity, the valve is configured for a certain level of standing damping that can be adjusted for the user. If the ankle is dorsiflexing, as measured by a sufficiently positive ankle angular velocity, the ankle assumes a separate level of damping that can also be adjusted for the user.

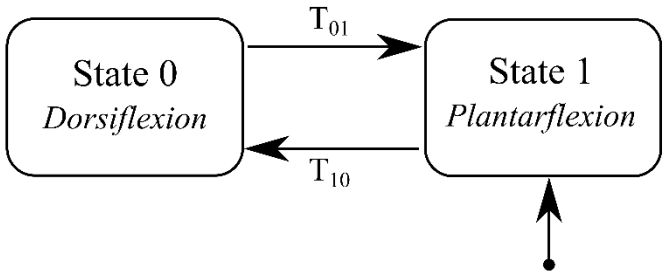

Fig. 5.6. Depiction of sloped standing finite state machine controller.

TABLE 5.2
FINITE STATE TRANSITIONS FOR THE SLOPED STANDING CONTROLLER

Transition	Description	Condition
T_{01}	Ankle plantarflexing	$\dot{\theta}_a < \dot{\theta}_{th,01}$
T_{10}	Ankle dorsiflexing	$\dot{\theta}_a > \dot{\theta}_{th,10}$

An activity-level controller was also designed to allow a user to switch naturally between walking and standing functionality. This activity-level controller and its associated state transition conditions are depicted in Fig. 5.7 and Table 5.3. The ankle begins in the walking controller. If the walking controller has remained in any one state for longer than a threshold time period, the ankle transitions into the standing controller, entering the standing controller in the plantarflexive state. The activity-level controller transitions back into the walking controller if the ankle is unloaded, the shank angle is sufficiently negative, and the shank angular velocity has been sufficiently negative during a window of time of tunable duration preceding the state transition. These transition conditions are satisfied when the user extends their leg in order to take a walking step.

These controllers were implemented in MATLAB/Simulink and were tested utilizing the hardware platform seen in Fig. 5.2. Low level position control of the motors was implemented on the embedded system and power was supplied via the onboard battery.

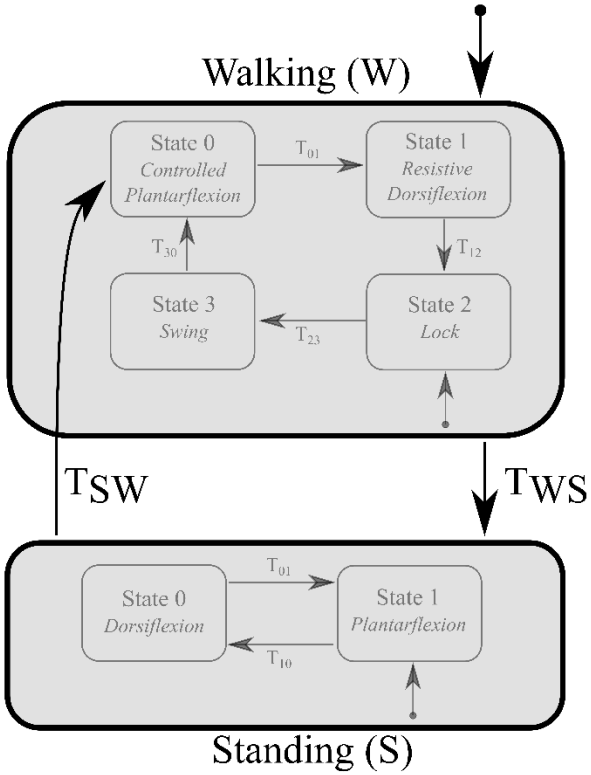

Fig. 5.7. Depiction of activity-level finite state machine controller allowing transitions between walking and standing controllers

TABLE 5.3
FINITE STATE TRANSITIONS FOR THE ACTIVITY-LEVEL CONTROLLER

Transition	Description	Condition
T_{WS}	Time out	$t_{ST} > t_{th,WS}$
T_{SW}	Shank positioned for heelstrike, ankle unloaded, and sufficiently negative shank angular velocity during recent time period	$\theta_s < \theta_{th,SW}$ $\tau_a < \tau_{th,SW}$ $\dot{\theta}_s < \dot{\theta}_{th,SW}$ while $(t - t_{th,SW}) < t_{event} \leq t$

5.1.4 Sloped Walking and Standing Assessment

The semi-powered prostheses was assessed while walking and standing on slopes on a single transtibial amputee subject relative to the subject's daily-use prosthesis. Approval to perform these experiments was granted by the Vanderbilt Institutional Review Board, and informed consent was obtained from the subject prior to the assessments. The subject was a 51-year-old male with a left-side amputation and a mass of 81 kg. The subject's daily-use

prosthesis was a Fillauer Allpro.

5.1.4.1 *Sloped Walking*

The slope-adaptive controller was assessed relative to the subject's daily-use prosthesis across a series of five slope conditions: 6 and 3 degree decline/incline (a positive slope angle will here forth indicate an incline while negative values will indicated a decline) as well as level ground. Each walking trial (conducted with both the semi-powered and daily-use devices) consisted of walking at 0.8 m/s for one minute on a split-belt instrumented treadmill (Bertec). Lower-body kinematic data was recorded using a motion capture system (Vicon) while ground reaction forces were recorded using the treadmill.

5.1.4.2 *Sloped Standing*

The sloped standing capabilities of the semi-powered ankle were also assessed relative to the subject's daily-use device across 11 different slope conditions ranging from -15 degrees to +15 degrees in the three degree increments. In each standing trial, the subject first adjusted to the slope, and then data was recorded for 15 seconds of quiet standing. Lower-body kinematic data and ground reaction forces were recorded using a motion capture system (Vicon) and the instrumented treadmill (Bertec), respectively.

5.1.4.3 *Data Processing and Analysis*

During the experiments, ground reaction force data were collected under each foot at 1000 Hz using a split-belt instrumented treadmill (Bertec), and lower-body kinematics were recorded at 200 Hz via a synchronized motion capture system (Vicon). Biological joint

angles, moments and powers were calculated over the stride using biomechanics modeling software (Visual 3D). All data were divided into strides normalized to 100% stride cycle, then averaged across strides prior to reporting. Ground reactions forces and motion capture data were filtered in post-processing with a zero-phase, 3rd order low-pass Butterworth filter at 15 Hz and 6 Hz, respectively.

In order to assess the efficacy of the semi-powered device, ankle angle, ankle torque, ground reaction force magnitude, shank angle, toe clearance, and time between heel strike and foot flat during the stride were all assessed. These data were compared between the semi-powered ankle and the subject's daily-use prosthesis. Healthy subject data from was utilized as a reference where possible [83].

The majority of these output metrics are directly reported from the biomechanics modeling software package (Visual 3D). Toe clearance was, however, calculated in post-processing based on the position of three markers denoting the plane of the treadmill and the position of a single marker placed on the toe of the foot. Specifically, the Cartesian position of the toe marker relative to the plane defined by the treadmill markers (using the corner of the treadmill as the origin) was calculated to indicate the trajectory of the toe marker across a stride. The time between heel strike and foot flat was calculated using video footage of the walking trials.

5.1.5 Results

5.1.5.1 *Level Walking*

The ankle angles of the semi-powered and passive daily use prostheses are plotted as a function of percentage of stride for level ground walking at 0.8 m/s in Fig. 5.8. The semi-

powered prosthesis is plotted in black while the passive device is plotted in red. A healthy ankle trajectory is provided as a reference and is plotted in green.

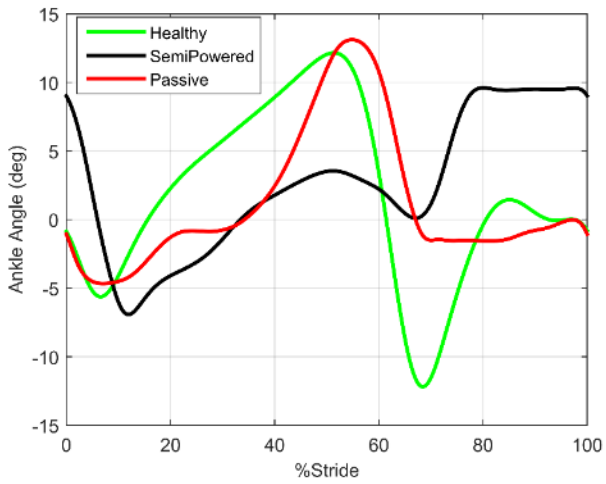

Fig. 5.8. Ankle angle vs. percent stride for healthy subjects (green), semi-powered ankle (black), and passive prosthesis (red).

The minimum foot clearance trajectory is shown in Fig. 5.9 for the semi-powered ankle (shown in black) and the passive ankle (shown in red). This trajectory shows the path taken through space by a point near the ball of the foot from the point of view of a moving reference frame traveling at the speed of the treadmill (0.8 m/s). This trajectory can be thought of as the path that the ball of the foot traverses during a stride in the reference frame of the treadmill. In this figure, the subject is walking in the positive x direction. A point on the ball of the foot was chosen to be tracked such that the minimum foot clearance during swing could be estimated. The point at which minimum foot clearance occurs is denoted by a small dot along the trajectory traced for each prosthesis in Fig. 5.9. The minimum foot clearance while wearing the semi-powered prosthesis was 4.20 cm +/- 0.22 cm while the minimum foot clearance while wearing the passive prosthesis was 0.55 cm +/- 0.23 cm, where the differences were verified via a two-sample t-test to be statistically significant with confidence greater than 99%.

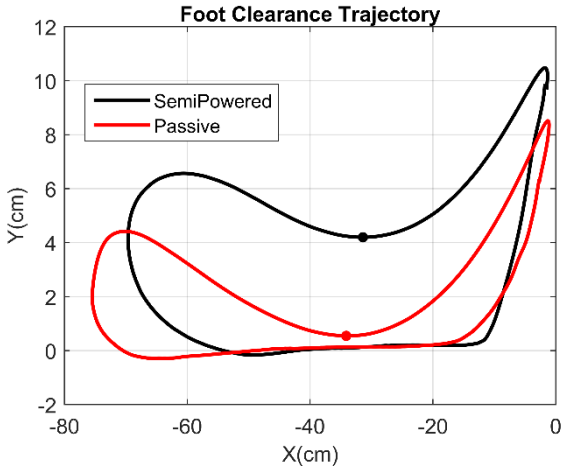

Fig. 5.9. Foot clearance trajectory for the semi-powered ankle (black) and the passive ankle (red). This trajectory shows the path taken through space by a point near the ball of the foot from the point of view of a moving reference frame traveling at the speed of the treadmill (0.8 m/s). Minimum foot clearance during the swing phase is marked with a small circle.

5.1.5.2 *Sloped Walking*

Fig. 5.10 shows ankle torque plotted against shank angle data walking at five different slopes for ten averaged healthy subjects (Fig. 5.10 top); for the transtibial amputee subject walking at the same speed and slopes on the semi-powered prosthesis (Fig. 5.10 middle); and for the transtibial amputee subject walking on the passive prosthesis (Fig. 5.10 bottom). Each trace on each plot corresponds to the average relationship between ankle torque and shank angle (where 0 degrees shank angle is aligned with gravity) over multiple strides, and for the healthy subject plot, over multiple subjects. Gray bands highlight the region over which the ankle torque crosses zero.

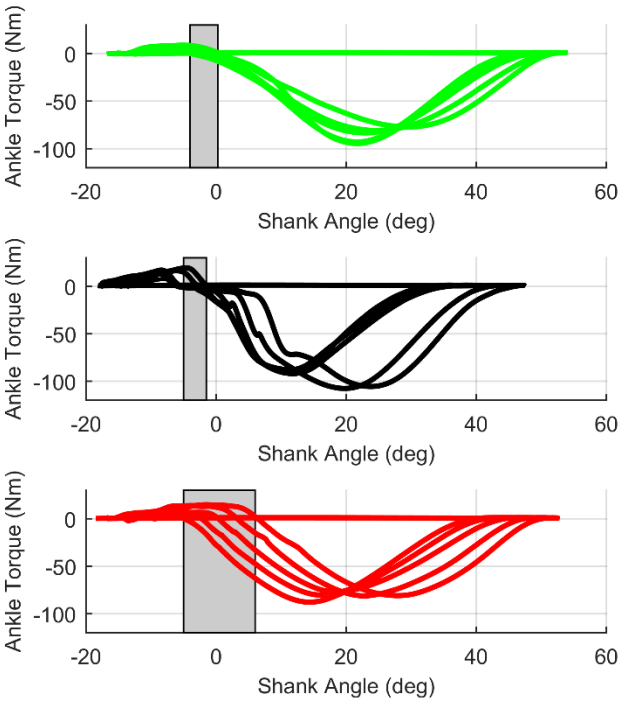

Fig. 5.10. Ankle torque plotted against shank angle data walking at five different slopes for ten averaged healthy subjects (Fig. 5.10 top); for the transtibial amputee subject walking at the same speed and slopes on the semi-powered prosthesis (Fig. 5.10 middle); and for the transtibial amputee subject walking on the passive prosthesis (Fig. 5.10 bottom). Gray bands highlight the region over which the ankle torque crosses zero.

Time to foot flat (length of time between heel strike and foot flat) was also calculated for the trials in which the subject descended the steepest slope (-6 degrees). The average time to foot flat (TTFF) was measured to be 0.20 +/- 0.022 seconds for the passive prosthesis and 0.15 +/- 0.025 seconds for the semi-powered prosthesis. This difference is statistically significant (with greater than 99% confidence) as measured by a two-sample t-test.

5.1.5.3 *Sloped Standing*

Photographs of the subject standing on the two most extreme slopes with his passive prosthesis are shown in Fig. 5.11. Fig. 5.12 shows the subject standing on the same two slopes with the semi-powered prosthesis. It should be noted that the semi-powered prosthesis

is able to adapt to the ground slope (Fig. 5.12) more so than the daily-use prosthesis (Fig. 5.11).

Fig. 5.11. Sloped standing on most extreme slopes with passive prosthesis

Fig. 5.12. Sloped standing on most extreme slopes with semi-powered prosthesis

The mean ground reaction force (GRF) magnitudes while standing are shown across the eleven different slopes tested for both the sound side and prosthetic side as a set of double bar plots in Fig. 5.13. The measured GRFs while wearing the semi-powered device are shown in the top plot while the GRFs while wearing the passive prosthesis are shown in the bottom plot.

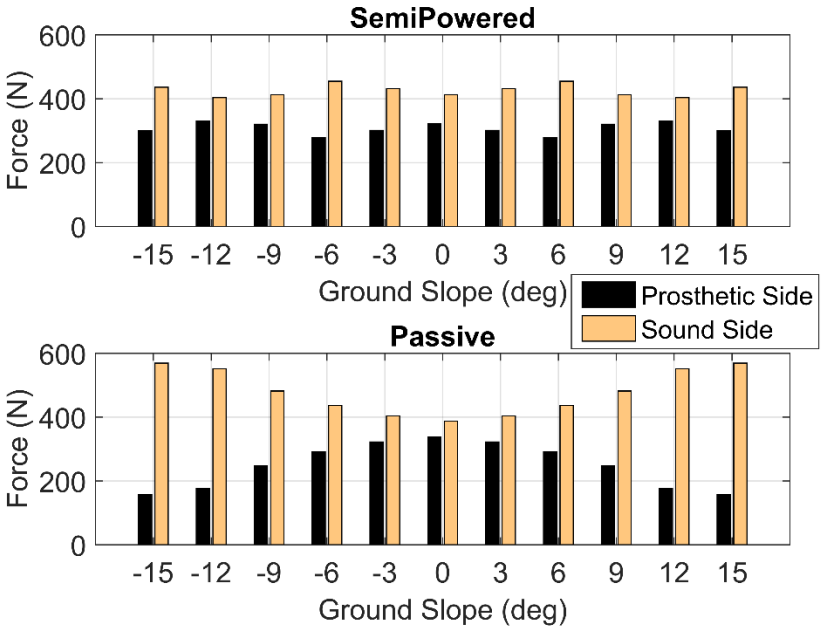

Figure 5.13. The mean ground reaction force (GRF) magnitudes while standing across the eleven different slopes tested for both the sound side and prosthetic side as a set of double bar plots. The measured GRFs while wearing the semi-powered device are shown in the top plot while the GRFs while wearing the passive prosthesis are shown in the bottom plot.

The average ankle torque while standing are shown across slopes for both the sound side and prosthetic side as a set of double bar plots in Fig. 5.14. The ankle torques while wearing the semi-powered prosthesis are shown in the top plot while the torques while wearing the passive prosthesis are shown in the bottom plot.

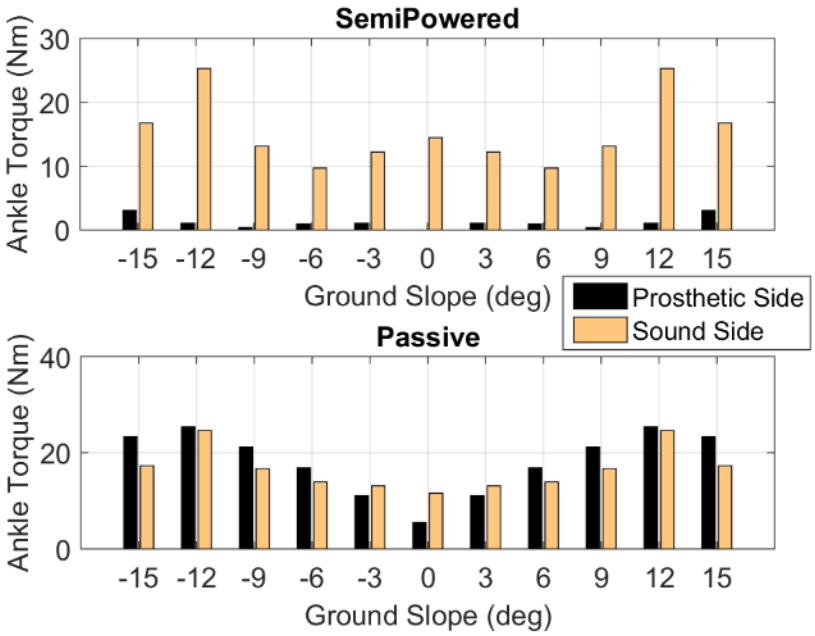

Fig. 5.14. The average ankle torque while standing across slopes for both the sound side and prosthetic side as a set of double bar plots. The ankle torques while wearing the semi-powered prosthesis are shown in the top plot while the torques while wearing the passive prosthesis are shown in the bottom plot.

5.1.6 Discussion

5.1.6.1 *Level Walking*

As can be seen in Fig. 5.8, the semi-powered ankle generally exhibits the appropriate ankle kinematic behavior during level walking. Specifically, the semi-powered device conforms to the ground during approximately the first 15% of stride. At this point, the ankle exhibits an appropriate stance behavior such that the ankle tends to dorsiflex as the user's shank progresses (15-55% of stride). During the swing phase, the semi-powered ankle is also able to dorsiflex in order to provide toe clearance (65-100%). This feature was intentionally exaggerated during the control design phase in order to further reduce the likelihood of a stumble. It should be noted that the minimal dorsiflexion of the semi-powered prosthesis during stance relative to the healthy reference curve is most-likely due to the use of a carbon

fiber foot plate that is too stiff. This may be remedied in future work by selecting a foot plate with reduced torsional stiffness. During level walking, the passive prosthesis exhibited appropriate stance behavior between 15% and 55% of stride, however, the passive prosthesis is not able to dorsiflex during swing phase as can be seen in Fig. 5.8. The semi-powered prosthesis does not attain as much dorsiflexion during the stance phase when compared to the passive prosthesis or the healthy reference data. This is due to the stiff carbon-fiber foot plate used in the system. In future work, the foot plate stiffness may be chosen to allow for appropriate deformation during stance. It should also be noted that neither the semi-powered nor passive prosthesis provided the plantarflexive motion associated with powered push off (55-65% of stride on the healthy reference curve) because neither of these devices are capable of delivering net positive power.

The foot clearance trajectory during level ground walking is shown in Fig. 5.9, and this figure shows that the semi-powered ankle obtains significantly more foot clearance as compared to the passive ankle prosthesis (a mean difference of 3.7 cm). Studies of healthy subjects indicate an average minimum foot clearance during level walking between 1 and 3 cm [84]. The minimum foot clearance with the passive prosthesis is well below the average healthy subject range, which may contribute to the higher incidence of falls and fear of falling that has been observed in the amputee population [42, 43, 85]. The increased foot clearance observed while using the semi-powered prosthesis may help to decrease the likelihood of falls in this population.

5.1.6.2 *Sloped Walking*

Fig. 5.10 shows ankle torque plotted against shank angle for sloped walking on

terrain with global slope ranging from -6 degrees to 6 degrees. As can be seen from the top plot in Fig. 5.10, healthy subjects adopt an almost constant "virtual" impedance about the shank with a similar stiffness and shank-based equilibrium position (approximately aligned with gravity) regardless of the ground slope. The zero-torque crossing region of each plot in this figure is highlighted in gray to show the range of "virtual" equilibrium positions adopted by the human/prosthesis. The gray region in the top plot is narrow, indicating a consistent "virtual" equilibrium position adopted by the human across all slope conditions. As can be seen in the middle plot in Fig. 5.10, the semi-powered prosthesis is able to mimic healthy behavior in order to maintain a consistent "virtual" equilibrium position across the various ground slopes. This behavior requires that the ankle angle shift its equilibrium angle by the ground slope angle for each slope. As seen in the middle plot of the semi-powered prosthesis, the prosthesis shifts its equilibrium angle similarly to the healthy ankle behavior, as represented by the gray band representing the spread of zero-torque crossing. As can be seen in the bottom plot, however, the passive ankle is unable to shift its equilibrium point according to ground slope, and as such is characterized by a large spread of zero-crossing, as indicated by the gray band in the bottom plot. In summary, healthy slope walking behavior is characterized by a shift in the ankle stiffness equilibrium angle in such a manner that renders the "virtual" shank angle equilibrium essentially invariant, as shown in Fig. 5.10 (top). The unique characteristics of the semi-powered prosthesis enable it to provide this behavior, while the inability of the passive prosthesis to shift its ankle equilibrium angle prevents it from providing the appropriate behavior.

5.1.6.3 *Sloped Standing*

As is visible in Fig. 5.12, the semi-powered prosthesis adapts to the slope, in contrast with the passive prosthesis shown in Fig. 5.11, which cannot. Due to the incongruence between the passive prosthesis and ground in both upslope and downslope conditions, the subject cannot load the prosthesis without creating a destabilizing moment at his prosthetic ankle. In the case of the passive prosthesis, the subject is able to fully load the prosthetic foot, without introducing a destabilizing moment. This effect is clearly seen in the associated ground reaction force and ankle moment data, respectively. Specifically, Fig. 5.13 shows that with the passive prosthesis (Fig. 5.13, top), the subject loads both the prosthesis and sound legs nearly equally, thus establishing a broad support polygon between the two legs. With the passive prosthesis (Fig. 5.13, bottom), however, the subject loads the prosthesis in inverse proportion to slope, and thus is primarily standing on his sound side as the ground slopes away from level. The cause of his limited ability to load the passive prosthesis when the ground is not level is elucidated by the data in Fig. 5.14, which shows that, as the passive prosthesis is loaded at increasing slope magnitudes, the incongruence between the prosthesis and slope results in increasing ankle moments (Fig. 5.14, bottom), which are both destabilizing, and also create socket discomfort. As seen in the corresponding data for the semi-powered prosthesis (Fig. 5.14, top), however, the subject prefers to minimize the moment on the prosthesis, which corresponds directly to the moment on his socket. Therefore, the adaptive nature of the semi-powered prosthesis is able to provide increased stability by increasing the base of support and eliminating destabilizing moments, while simultaneously minimizing socket torques and thus presumably enhancing comfort.

5.1.7 Conclusion

This chapter presents the redesign of the ankle actuator such that the ankle can provide controlled damping and locking in a bidirectional manner. Controllers for sloped standing and walking were then developed and implemented on the redesigned ankle. The controller exhibited beneficial behavior while walking on level terrain; the semi-powered prosthesis was able to provide a statistically significant increase in foot clearance during mid-swing, which may result in a decrease in the likelihood of stumbles for amputee users. The sloped walking controller leverages observations from healthy walking data to provide appropriate behavior across slopes without identifying the ground slope or modulating any control parameters across slopes. The sloped waking controller was shown to provide more appropriate biomechanical behavior across slopes relative to the subject's passive daily-use prosthesis, specifically with regard to enforcing a "virtual" shank-based equilibrium angle. The developed standing controller was able to show reduced socket moments while standing on highly sloped ground and was also to show more equal ground reaction force distribution between the prosthetic and sound side limbs while standing on sloped ground. In summary, the semi-powered prosthesis may provide biomechanically beneficial behavior to amputee users while walking and standing on slopes of various terrains.

Chapter 6

Conclusion

6.1 Contributions

This dissertation described the design, control, and assessment of a semi-powered prosthetic ankle. The ankle prosthesis was developed with the aim of improving both the safety and mobility of individuals with lower limb amputations while simultaneously minimizing the size and mass of the prosthesis. The resulting ankle prosthesis leverages the concept of a power-asymmetric actuator (an actuator capable of dissipating more power than it can generate) in order to minimize the device size. Specifically, the prosthetic ankle utilizes the high passive power density of hydraulic actuators for power dissipation and the controllability and compactness of electromechanical actuation for power generation. Novel mechanical designs architectures were developed in order to combine these two actuation approaches in a compact package. One such novel mechanical design is a single-rod constant-volume hydraulic cylinder that allows bidirectional damping and locking capabilities while maintaining a smaller design envelope than comparable double-rod constant volume hydraulic cylinders. The ankle design also employs a lead-screw-based electromechanical actuator concentric with the central bore of the hydraulic cylinder to minimize the design envelope.

Controllers for multiple different activities of daily living were designed and implemented on the semi-powered prosthesis hardware. State machine controllers were developed for the following activities: stair descent, level/sloped walking, and level/sloped standing. An activity-level controller was also developed that allows for transitioning

between the standing and walking controllers.

The stair descent controller allows users to adopt more natural kinematics when descending stairs as the ankle plantarflexes in preparation for foot strike. Studies on a single subject indicated that the loading rate associated with prosthetic foot strike during stair descent decreased while wearing the semi-powered prosthesis relative to a passive device. This decrease in loading rate may help to improve comfort for amputee users.

The walking controller leverages observations from healthy walking data across multiple slopes in order to design a single control policy for the semi-powered ankle that provides the appropriate behavior across multiple slopes without modulating any control parameters or identifying the ground slope. In the single-subject studies, this controller was shown to effectively adapt to various slopes and was shown to significantly increase foot clearance during the swing phase of level walking. This increase in foot clearance may help to decrease the likelihood of stumbles or falls for users.

The standing controller was developed in order to allow for quiet standing on various ground slopes. In the single-subject studies, the controller was shown to more equally distribute ground reaction forces between the subject's prosthetic side and sound side limbs for all ground slopes tested relative to the user's daily use passive device. Simultaneously, the standing controller reduced ankle (and subsequently, socket) torques across slopes. This reduction of socket torques during sloped standing may help to improve comfort for amputee users.

6.2 Clinical Significance

The primary goal of this work was to develop a semi-powered ankle prosthesis and

accompanying controllers for activities of daily living. This work focused primarily on hardware design and controller development in the context of a mechanical engineering laboratory, and as such, statistically-powered studies on multiple subjects were not performed. All studies run in the course of this work were performed with a single subject. In the author's option, the promising results obtained with the single subject in the assessments described here warrant future assessments involving multiple subjects, to see if the results hold across subjects, and if the results have clinical value.

BIBLIOGRAPHY

[1] H. L. Bartlett, B. E. Lawson, and M. Goldfarb, "Optimal Transmission Ratio Selection for Electric Motor Driven Actuators With Known Output Torque and Motion Trajectories," *Journal of Dynamic Systems, Measurement, and Control,* vol. 139, pp. 101013-101013-7, 2017.

[2] H. L. Bartlett, B. E. Lawson, and M. Goldfarb, "On the design of power gear trains: Insight regarding number of stages and their respective ratios," *PLOS ONE,* vol. 13, p. e0198048, 2018.

[3] H. L. Bartlett and M. Goldfarb, "A Phase Variable Approach for IMU-Based Locomotion Activity Recognition," *IEEE Transactions on Biomedical Engineering,* vol. PP, pp. 1-1, 2017.

[4] S. Culver, H. Bartlett, A. Shultz, and M. Goldfarb, "A Stair Ascent and Descent Controller for a Powered Ankle Prosthesis," *IEEE Transactions on Neural Systems and Rehabilitation Engineering,* vol. PP, pp. 1-1, 2018.

[5] B. E. Lawson, H. A. Varol, A. Huff, E. Erdemir, and M. Goldfarb, "Control of stair ascent and descent with a powered transfemoral prosthesis," *Neural Systems and Rehabilitation Engineering, IEEE Transactions on,* vol. 21, pp. 466-473, 2013.

[6] C. D. Hoover, G. D. Fulk, and K. B. Fite, "Stair ascent with a powered transfemoral prosthesis under direct myoelectric control," *IEEE/ASME Transactions on Mechatronics,* vol. 18, pp. 1191-1200, 2013.

[7] E. D. Ledoux and M. Goldfarb, "Control and evaluation of a powered transfemoral prosthesis for stair ascent," *IEEE Transactions on Neural Systems and Rehabilitation Engineering,* vol. 25, pp. 917-924, 2017.

[8] M. Wu and X. Shen, "Walking-Stair Climbing Control for Powered Knee Prostheses," in *ASME 2016 Dynamic Systems and Control Conference*, 2016, pp. V001T07A006-V001T07A006.

[9] A. Parri, E. Martini, J. Geeroms, L. Flynn, G. Pasquini, S. Crea, *et al.*, "Whole body awareness for controlling a robotic transfemoral prosthesis," *Frontiers in neurorobotics,* vol. 11, p. 25, 2017.

[10] A. J. Young, A. M. Simon, and L. J. Hargrove, "A training method for locomotion mode prediction using powered lower limb prostheses," *Neural Systems and Rehabilitation Engineering, IEEE Transactions on,* vol. 22, pp. 671-677, 2014.

[11] H. Zhao, J. Reher, J. Horn, V. Paredes, and A. D. Ames, "Realization of stair ascent and motion transitions on prostheses utilizing optimization-based control and intent recognition," in *Rehabilitation Robotics (ICORR), 2015 IEEE International Conference on*, 2015, pp. 265-270.

[12] A. M. Simon, K. A. Ingraham, J. A. Spanias, A. J. Young, S. B. Finucane, E. G. Halsne, *et al.*, "Delaying ambulation mode transition decisions improves accuracy of a flexible control system for powered knee-ankle prosthesis," *IEEE Transactions on Neural Systems and Rehabilitation Engineering,* vol. 25, pp. 1164-1171, 2017.

[13] S. Habibi and A. Goldenberg, "Design of a new high performance electrohydraulic actuator," in *1999 IEEE/ASME International Conference on Advanced Intelligent Mechatronics (Cat. No.99TH8399)*, 1999, pp. 227-232.

[14] S. Habibi, V. Pastrakuljic, and A. Goldenberg, "Model identification and analysis of a high performance hydrostatic actuation system," SAE Technical Paper 0148-

7191, 2000.
[15] S. Habibi, R. Burton, and E. Sampson, "High precision hydrostatic actuation systems for micro-and nanomanipulation of heavy loads," *Journal of dynamic systems, measurement, and control*, vol. 128, pp. 778-787, 2006.
[16] V. Pastrakuljic, "Design and modeling of a new electro hydraulic actuator," National Library of Canada= Bibliothèque nationale du Canada, 1995.
[17] M. Linjama, M. Paloniitty, L. Tiainen, and K. Huhtala, "Mechatronic design of digital hydraulic micro valve package," *Procedia engineering*, vol. 106, pp. 97-107, 2015.
[18] M. Linjama, H.-P. Vihtanen, A. Sipola, and M. Vilenius, "Secondary controlled multi-chamber hydraulic cylinder," in *The 11th Scandinavian International Conference on Fluid Power, SICFP*, 2009, pp. 2-4.
[19] K. Heybroek and E. Norlin, "Hydraulic multi-chamber cylinders in construction machinery," in *Hydraulikdagarna 2015, Linköping University, Linköping, Sweden, March 16-17, 2015*, 2015.
[20] W. Xiao-Ming, L. Qian, and L. Xin, "The four-chamber hydraulic cylinder," in *Aircraft Utility Systems (AUS), IEEE International Conference on*, 2016, pp. 686-689.
[21] A. H. Shultz and M. Goldfarb, "A Unified Controller for Walking on Even and Uneven Terrain with a Powered Ankle Prosthesis," *IEEE Transactions on Neural Systems and Rehabilitation Engineering*, vol. PP, pp. 1-1, 2018.
[22] R. D. Bellman, M. A. Holgate, and T. G. Sugar, "SPARKy 3: Design of an active robotic ankle prosthesis with two actuated degrees of freedom using regenerative kinetics," in *2008 2nd IEEE RAS & EMBS International Conference on Biomedical Robotics and Biomechatronics*, 2008, pp. 511-516.
[23] S. K. Au and H. M. Herr, "Powered ankle-foot prosthesis," *IEEE Robotics & Automation Magazine*, vol. 15, pp. 52-59, 2008.
[24] M. Cempini, L. J. Hargrove, and T. Lenzi, "Design, Development, and Bench-top Testing of a Powered Polycentric Ankle Prosthesis."
[25] P. Cherelle, V. Grosu, M. Cestari, B. Vanderborght, and D. Lefeber, "The AMP-Foot 3, new generation propulsive prosthetic feet with explosive motion characteristics: design and validation," *BioMedical Engineering OnLine*, vol. 15, p. 21, 2016.
[26] J. Realmuto, G. Klute, and S. Devasia, "Nonlinear Passive Cam-Based Springs for Powered Ankle Prostheses," *Journal of Medical Devices*, vol. 9, p. 011007, 2015.
[27] A. H. Shultz, J. E. Mitchell, D. Truex, B. E. Lawson, and M. Goldfarb, "Preliminary evaluation of a walking controller for a powered ankle prosthesis," in *Robotics and automation (ICRA), 2013 IEEE international conference on*, 2013, pp. 4838-4843.
[28] M. K. Shepherd and E. J. Rouse, "The VSPA Foot: A Quasi-Passive Ankle-Foot Prosthesis with Continuously Variable Stiffness," *IEEE Transactions on Neural Systems and Rehabilitation Engineering*, vol. PP, pp. 1-1, 2017.
[29] J. Lee, L. Mooney, and E. Rouse, "Design and Characterization of a Quasi-Passive Pneumatic Foot-Ankle Prosthesis," *IEEE Transactions on Neural Systems and Rehabilitation Engineering*, vol. PP, pp. 1-1, 2017.
[30] T. Lenzi, M. Cempini, J. Newkirk, L. J. Hargrove, and T. A. Kuiken, "A

lightweight robotic ankle prosthesis with non-backdrivable cam-based transmission," in *Rehabilitation Robotics (ICORR), 2017 International Conference on*, 2017, pp. 1142-1147.

[31] A. LaPrè and F. Sup, "A semi-active damper design for use in a terrain adaptive ankle prosthesis," in *ASME 2011 International Mechanical Engineering Congress and Exposition*, 2011, pp. 1289-1294.

[32] S. K. Au, J. Weber, and H. Herr, "Powered Ankle--Foot Prosthesis Improves Walking Metabolic Economy," *Robotics, IEEE Transactions on*, vol. 25, pp. 51-66, 2009.

[33] S. R. Koehler-McNicholas, E. A. Nickel, J. Medvec, K. Barrons, S. Mion, and A. H. Hansen, "The influence of a hydraulic prosthetic ankle on residual limb loading during sloped walking," *PloS one*, vol. 12, p. e0173423, 2017.

[34] A. R. De Asha, R. Munjal, J. Kulkarni, and J. G. Buckley, "Impact on the biomechanics of overground gait of using an 'Echelon'hydraulic ankle–foot device in unilateral trans-tibial and trans-femoral amputees," *Clinical Biomechanics*, vol. 29, pp. 728-734, 2014.

[35] N. J. Rosenblatt, A. Bauer, D. Rotter, and M. D. Grabiner, "Active dorsiflexing prostheses may reduce trip-related fall risk in people with transtibial amputation," *J Rehabil Res Dev*, vol. 51, pp. 1229-1242, 2014.

[36] B. J. Darter and J. M. Wilken, "Energetic consequences of using a prosthesis with adaptive ankle motion during slope walking in persons with a transtibial amputation," *Prosthetics and orthotics international*, vol. 38, pp. 5-11, 2014.

[37] K. Ziegler-Graham, E. J. MacKenzie, P. L. Ephraim, T. G. Travison, and R. Brookmeyer, "Estimating the prevalence of limb loss in the United States: 2005 to 2050," *Archives of physical medicine and rehabilitation*, vol. 89, pp. 422-429, 2008.

[38] C. Gauthier-Gagnon, M.-C. Grisé, and D. Potvin, "Enabling factors related to prosthetic use by people with transtibial and transfemoral amputation," *Archives of physical medicine and rehabilitation*, vol. 80, pp. 706-713, 1999.

[39] C. Gauthier-Gagnon and M.-C. Grisé, "Tools to measure outcome of people with a lower limb amputation: Update on the PPA and LCI," *JPO: Journal of Prosthetics and Orthotics*, vol. 18, pp. P61-P67, 2006.

[40] H. Burger, Č. Marinček, and E. Isakov, "Mobility of persons after traumatic lower limb amputation," *Disability and rehabilitation*, vol. 19, pp. 272-277, 1997.

[41] B. Larsson, A. Johannesson, I. H. Andersson, and I. Atroshi, "The Locomotor Capabilities Index; validity and reliability of the Swedish version in adults with lower limb amputation," *Health and quality of life outcomes*, vol. 7, p. 44, 2009.

[42] W. C. Miller, A. B. Deathe, M. Speechley, and J. Koval, "The influence of falling, fear of falling, and balance confidence on prosthetic mobility and social activity among individuals with a lower extremity amputation," *Archives of physical medicine and rehabilitation*, vol. 82, pp. 1238-1244, 2001.

[43] W. C. Miller, M. Speechley, and B. Deathe, "The prevalence and risk factors of falling and fear of falling among lower extremity amputees," *Archives of physical medicine and rehabilitation*, vol. 82, pp. 1031-1037, 2001.

[44] L. E. Pezzin, T. R. Dillingham, E. J. MacKenzie, P. Ephraim, and P. Rossbach, "Use and satisfaction with prosthetic limb devices and related services," *Archives of*

physical medicine and rehabilitation, vol. 85, pp. 723-729, 2004.
[45] A. Vrieling, H. Van Keeken, T. Schoppen, E. Otten, J. Halbertsma, A. Hof, *et al.*, "Uphill and downhill walking in unilateral lower limb amputees," *Gait & posture*, vol. 28, pp. 235-242, 2008.
[46] K. James and R. Stein, "Improved ankle-foot system for above-knee amputees," *American journal of physical medicine*, vol. 65, pp. 301-314, 1986.
[47] T. Schmalz, S. Blumentritt, and B. Marx, "Biomechanical analysis of stair ambulation in lower limb amputees," *Gait & posture*, vol. 25, pp. 267-278, 2007.
[48] M. Alimusaj, L. Fradet, F. Braatz, H. J. Gerner, and S. I. Wolf, "Kinematics and kinetics with an adaptive ankle foot system during stair ambulation of transtibial amputees," *Gait & posture*, vol. 30, pp. 356-363, 2009.
[49] S. Au, M. Berniker, and H. Herr, "Powered ankle-foot prosthesis to assist level-ground and stair-descent gaits," *Neural Networks*, vol. 21, pp. 654-666, 2008.
[50] C.-Y. Ko, S.-B. Kim, J. K. Kim, Y. Chang, S. Kim, J. Ryu, *et al.*, "Comparison of ankle angle adaptations of prosthetic feet with and without adaptive ankle angle during level ground, ramp, and stair ambulations of a transtibial amputee: A pilot study," *International journal of precision engineering and manufacturing*, vol. 15, pp. 2689-2693, 2014.
[51] F. Sup, H. A. Varol, J. Mitchell, T. J. Withrow, and M. Goldfarb, "Preliminary Evaluations of a Self-Contained Anthropomorphic Transfemoral Prosthesis," *IEEE ASME Trans Mechatron*, vol. 14, pp. 667-676, 2009.
[52] B. J. Bergelin, J. O. Mattos, J. G. Wells, and P. A. Voglewede, "Concept through preliminary bench testing of a powered lower limb prosthetic device," *Journal of mechanisms and robotics*, vol. 2, p. 041005, 2010.
[53] M. Grimmer, M. Holgate, J. Ward, A. Boehler, and A. Seyfarth, "Feasibility study of transtibial amputee walking using a powered prosthetic foot," in *Rehabilitation Robotics (ICORR), 2017 International Conference on*, 2017, pp. 1118-1123.
[54] R. C. Browning, J. R. Modica, R. Kram, and A. Goswami, "The effects of adding mass to the legs on the energetics and biomechanics of walking," *Medicine & Science in Sports & Exercise*, vol. 39, pp. 515-525, 2007.
[55] T. D. Royer and P. E. Martin, "Manipulations of leg mass and moment of inertia: effects on energy cost of walking," *Medicine and science in sports and exercise*, vol. 37, pp. 649-656, 2005.
[56] Q. Wang, K. Yuan, J. Zhu, and L. Wang, "Walk the Walk: A Lightweight Active Transtibial Prosthesis," *IEEE Robotics & Automation Magazine*, vol. 22, pp. 80-89, 2015.
[57] A. R. Wu and A. D. Kuo, "Determinants of preferred ground clearance during swing phase of human walking," *Journal of Experimental Biology*, vol. 219, pp. 3106-3113, 2016.
[58] H. L. Bartlett, B. E. Lawson, and M. Goldfarb, "Design of a power-asymmetric actuator for a transtibial prosthesis," in *Rehabilitation Robotics (ICORR), 2017 International Conference on*, 2017, pp. 1531-1536.
[59] I. W. Hunter, J. M. Hollerbach, and J. Ballantyne, "A comparative analysis of actuator technologies for robotics," *Robotics Review*, vol. 2, pp. 299-342, 1991.
[60] K. W. Hollander and T. G. Sugar, "Design of lightweight lead screw actuators for wearable robotic applications," *Journal of Mechanical Design*, vol. 128, pp. 644-

648, 2006.
[61] A. H. Shultz, B. E. Lawson, and M. Goldfarb, "Walking on uneven terrain with a powered ankle prosthesis: A preliminary assessment," in *2015 37th Annual International Conference of the IEEE Engineering in Medicine and Biology Society (EMBC)*, 2015, pp. 5299-5302.
[62] R. Versluys, P. Beyl, M. Van Damme, A. Desomer, R. Van Ham, and D. Lefeber, "Prosthetic feet: State-of-the-art review and the importance of mimicking human ankle–foot biomechanics," *Disability and Rehabilitation: Assistive Technology*, vol. 4, pp. 65-75, 2009.
[63] A. Kennedy LaPrè, B. R. Umberger, and I. V. F. C. Sup, "A Robotic Ankle–Foot Prosthesis With Active Alignment," *Journal of Medical Devices*, vol. 10, pp. 025001-025001, 2016.
[64] A. H. Shultz, B. E. Lawson, and M. Goldfarb, "Variable cadence walking and ground adaptive standing with a powered ankle prosthesis," *IEEE Transactions on Neural Systems and Rehabilitation Engineering*, vol. 24, pp. 495-505, 2016.
[65] Y. Feng and Q. Wang, "Combining Push-Off Power and Nonlinear Damping Behaviors for a Lightweight Motor-Driven Transtibial Prosthesis," *IEEE/ASME Transactions on Mechatronics*, vol. 22, pp. 2512-2523, 2017.
[66] O. A. Kannape and H. M. Herr, "Volitional control of ankle plantar flexion in a powered transtibial prosthesis during stair-ambulation," in *Engineering in Medicine and Biology Society (EMBC), 2014 36th Annual International Conference of the IEEE*, 2014, pp. 1662-1665.
[67] R. Riener, M. Rabuffetti, and C. Frigo, "Stair ascent and descent at different inclinations," *Gait & posture*, vol. 15, pp. 32-44, 2002.
[68] F. L. Buczek, T. M. Kepple, K. L. Siegel, and S. J. Stanhope, "Translational and rotational joint power terms in a six degree-of-freedom model of the normal ankle complex," *Journal of biomechanics*, vol. 27, pp. 1447-1457, 1994.
[69] B. J. Ewers, V. M. Jayaraman, R. F. Banglmaier, and R. C. Haut, "Rate of blunt impact loading affects changes in retropatellar cartilage and underlying bone in the rabbit patella," *Journal of Biomechanics*, vol. 35, pp. 747-755.
[70] A. Hreljac, "Impact and overuse injuries in runners," *Medicine and science in sports and exercise*, vol. 36, pp. 845-849, 2004.
[71] A. Hreljac, R. N. Marshall, and P. A. Hume, "Evaluation of lower extremity overuse injury potential in runners," *Medicine & Science in Sports & Exercise*, vol. 32, pp. 1635-1641, 2000.
[72] C. E. Milner, R. Ferber, C. D. Pollard, J. Hamill, and I. S. Davis, "Biomechanical factors associated with tibial stress fracture in female runners," *Medicine & Science in Sports & Exercise*, vol. 38, pp. 323-328, 2006.
[73] F. R. Noyes, J. L. DeLucas, and P. J. Torvik, "Biomechanics of Anterior Cruciate Ligament Failure: An Analysis of," *J. Bone Joint Surg. Am*, vol. 56, pp. 236-253, 1974.
[74] N. Manring and G. R. Luecke, "Modeling and designing a hydrostatic transmission with a fixed-displacement motor," *Journal of dynamic systems, measurement, and control*, vol. 120, pp. 45-49, 1998.
[75] A. Kugi, K. Schlacher, H. Aitzetmüller, and G. Hirmann, "Modeling and simulation of a hydrostatic transmission with variable-displacement pump," *Mathematics and*

computers in simulation, vol. 53, pp. 409-414, 2000.
[76] P. Beater, *Pneumatic drives*: Springer, 2007.
[77] B. E. Lawson, H. A. Varol, and M. Goldfarb, "Standing stability enhancement with an intelligent powered transfemoral prosthesis," *Biomedical Engineering, IEEE Transactions on,* vol. 58, pp. 2617-2624, 2011.
[78] E. Nickel, "Passive prosthetic ankle-foot mechanism for automatic adaptation to sloped surfaces," *Journal of rehabilitation research and development,* vol. 51, p. 803, 2014.
[79] D. E. Amiot, R. M. Schmidt, A. Law, E. P. Meinig, L. Yu, K. M. Olesnavage, *et al.*, "Development of a Passive and Slope Adaptable Prosthetic Foot," in *ASME 2017 International Design Engineering Technical Conferences and Computers and Information in Engineering Conference*, 2017, pp. V05AT08A066-V05AT08A066.
[80] T. Sowell, "A preliminary clinical evaluation of the Mauch hydraulic foot-ankle system," *Prosthetics and orthotics international,* vol. 5, pp. 87-91, 1981.
[81] F. Sup, H. A. Varol, and M. Goldfarb, "Upslope walking with a powered knee and ankle prosthesis: initial results with an amputee subject," *IEEE Transactions on Neural Systems and Rehabilitation Engineering,* vol. 19, pp. 71-78, 2011.
[82] K. R. Embry, D. J. Villarreal, and R. D. Gregg, "A unified parameterization of human gait across ambulation modes," in *2016 38th Annual International Conference of the IEEE Engineering in Medicine and Biology Society (EMBC)*, 2016, pp. 2179-2183.
[83] D. A. Winter, *Biomechanics and motor control of human gait: normal, elderly and pathological*, 1991.
[84] R. Begg, R. Best, L. Dell'Oro, and S. Taylor, "Minimum foot clearance during walking: strategies for the minimisation of trip-related falls," *Gait & posture,* vol. 25, pp. 191-198, 2007.
[85] W. C. Miller, A. B. Deathe, and M. Speechley, "Lower extremity prosthetic mobility: a comparison of 3 self-report scales," *Archives of physical medicine and rehabilitation,* vol. 82, pp. 1432-1440, 2001.
[86] H. J. Van de Straete, P. Degezelle, J. De Schutter, and R. J. Belmans, "Servo motor selection criterion for mechatronic applications," *IEEE/ASME Transactions on mechatronics,* vol. 3, pp. 43-50, 1998.
[87] K. A. Pasch, "On drive systems for high performance machines and design of an air motor/particle brake actuator," Massachusetts Institute of Technology, 1984.
[88] H. J. Van de Straete, J. De Schutter, and R. Belmans, "An efficient procedure for checking performance limits in servo drive selection and optimization," *Mechatronics, IEEE/ASME Transactions on,* vol. 4, pp. 378-386, 1999.
[89] F. Roos, H. Johansson, and J. Wikander, "Optimal selection of motor and gearhead in mechatronic applications," *Mechatronics,* vol. 16, pp. 63-72, 2006.
[90] G. Cusimano, "Optimization of the choice of the system electric drive-device—transmission for mechatronic applications," *Mechanism and Machine Theory*, vol. 42, pp. 48-65, 1// 2007.
[91] G. Cusimano, "Choice of electrical motor and transmission in mechatronic applications: The torque peak," *Mechanism and Machine Theory,* vol. 46, pp. 1207-1235, 2011.
[92] G. Cusimano, "Influence of the reducer efficiencies on the choice of motor and

transmission: Torque peak of the motor," *Mechanism and Machine Theory*, vol. 67, pp. 122-151, 9// 2013.
[93] G. Cusimano, "Choice of motor and transmission in mechatronic applications: Non-rectangular dynamic range of the drive system," *Mechanism and Machine Theory*, vol. 85, pp. 35-52, 3// 2015.
[94] C. Choi, S. Jung, S. Kim, J. Lee, T. Choe, S. Chung, *et al.*, "A motor selection technique for designing a manipulator," in *Control, Automation and Systems, 2007. ICCAS'07. International Conference on*, 2007, pp. 2487-2492.
[95] M. Pettersson and J. Olvander, "Drive Train Optimization for Industrial Robots," *Robotics, IEEE Transactions on*, vol. 25, pp. 1419-1424, 2009.
[96] S. Rezazadeh and J. W. Hurst, "On the optimal selection of motors and transmissions for electromechanical and robotic systems," in *2014 IEEE/RSJ International Conference on Intelligent Robots and Systems*, 2014, pp. 4605-4611.
[97] H. Giberti, S. Cinquemani, and G. Legnani, "Effects of transmission mechanical characteristics on the choice of a motor-reducer," *Mechatronics*, vol. 20, pp. 604-610, 2010.
[98] H. Giberti, S. Cinquemani, and G. Legnani, "A practical approach to the selection of the motor-reducer unit in electric drive systems," *Mechanics based design of structures and machines*, vol. 39, pp. 303-319, 2011.
[99] H. Giberti, A. Clerici, and S. Cinquemani, "Specific accelerating factor: One more tool in motor sizing projects," *Mechatronics*, vol. 24, pp. 898-905, 10// 2014.
[100] J. W. Sensinger, "Selecting motors for robots using biomimetic trajectories: optimum benchmarks, windings, and other considerations," in *Robotics and Automation (ICRA), 2010 IEEE International Conference on*, 2010, pp. 4175-4181.
[101] J. E. Shigley and C. R. Mischke, "Standard handbook of machine design," 1986.
[102] H. M. Paynter, *Analysis and design of engineering systems*: MIT press, 1961.
[103] D. C. Karnopp, D. L. Margolis, and R. C. Rosenberg, "System dynamics: a unified approach," 1990.
[104] J. Braun, "Formulae Handbook," ed: Maxon Motors, 2012.
[105] "Technical Information," ed: Faulhaber, 2016.
[106] N. Paine and L. Sentis, "Design and Comparative Analysis of a Retrofitted Liquid Cooling System for High-Power Actuators," in *Actuators*, 2015, pp. 182-202.
[107] T. Reichert, T. Nussbaumer, and J. W. Kolar, "Torque scaling laws for interior and exterior rotor permanent magnet machines," *A A*, vol. 3, p. 1, 2009.
[108] J. W. Sensinger, S. D. Clark, and J. F. Schorsch, "Exterior vs. interior rotors in robotic brushless motors," in *Robotics and Automation (ICRA), 2011 IEEE International Conference on*, 2011, pp. 2764-2770.
[109] J. E. Gibson and F. B. Tuteur, *Control system components* vol. 320: McGraw-Hill, 1958.
[110] D. P. Peterson, "Power Gear Trains," *Machine Design*, vol. 26, p. 161, 1954.
[111] X. Tang, X. Hu, W. Yang, and H. Yu, "Novel Torsional Vibration Modeling and Assessment of a Power-Split Hybrid Electric Vehicle Equipped with a Dual Mass Flywheel," *IEEE Transactions on Vehicular Technology*, 2017.
[112] X. Tang, W. Yang, X. Hu, and D. Zhang, "A novel simplified model for torsional vibration analysis of a series-parallel hybrid electric vehicle," *Mechanical Systems and Signal Processing*, vol. 85, pp. 329-338, 2017.

[113] E. Burgess Jr, "Minimization of gear-train inertia," *Trans. of the ASME,* vol. 76, pp. 493-496, 1954.
[114] F. a. M. Freudenstein, M., "On the algorithms for the minimization of gear trains," *ASME Computers in Engineering,* pp. 199-202, 1982.
[115] M. Krön, "Minimum Inertia Design for Gear Trains," *JPL Technical Report 32-1256,* vol. XV, pp. 102-108.
[116] R. Selfridge, "Compound gear trains of minimum equivalent inertia," *Mechanism and Machine Theory,* vol. 15, pp. 287-294, 1980.
[117] B. Rosic, "Multicriterion optimization of multistage gear train transmission," *Facta Universitatis, series: Mechanical Engineering,* vol. 1, pp. 1107-1115, 2001.
[118] J. Stefanović-Marinović, M. Petković, I. Stanimirović, and M. Milovančević, "A model of planetary gear multicriteria optimization," *Transactions of FAMENA,* vol. 35, 2011.
[119] A. Swantner and M. I. Campbell, "Topological and parametric optimization of gear trains," *Engineering Optimization,* vol. 44, pp. 1351-1368, 2012.
[120] V. Savsani, R. V. Rao, and D. P. Vakharia, "Optimal weight design of a gear train using particle swarm optimization and simulated annealing algorithms," *Mechanism and Machine Theory,* vol. 45, pp. 531-541, 3// 2010.
[121] S. i. Golabi, J. J. Fesharaki, and M. Yazdipoor, "Gear train optimization based on minimum volume/weight design," *Mechanism and Machine Theory,* vol. 73, pp. 197-217, 2014.
[122] T. Yokota, T. Taguchi, and M. Gen, "Selected Papers from the 22nd ICC and IE ConferenceA solution method for optimal weight design problem of the gear using genetic algorithms," *Computers & Industrial Engineering,* vol. 35, pp. 523-526, 1998/12/01 1998.
[123] C. Gologlu and M. Zeyveli, "A genetic approach to automate preliminary design of gear drives," *Computers & Industrial Engineering,* vol. 57, pp. 1043-1051, 10// 2009.
[124] D. F. Thompson, S. Gupta, and A. Shukla, "Tradeoff analysis in minimum volume design of multi-stage spur gear reduction units," *Mechanism and Machine Theory,* vol. 35, pp. 609-627, 5// 2000.
[125] A. H. Gandomi, G. J. Yun, X.-S. Yang, and S. Talatahari, "Chaos-enhanced accelerated particle swarm optimization," *Communications in Nonlinear Science and Numerical Simulation,* vol. 18, pp. 327-340, 2// 2013.
[126] K. Deb and M. Goyal, "Optimizing Engineering Designs Using a Combined Genetic Search," in *ICGA*, 1997, pp. 521-528.
[127] F. Roos, "Towards a methodology for integrated design of mechatronic servo systems," 2007.
[128] T. H. Chong, I. Bae, and G.-J. Park, "A new and generalized methodology to design multi-stage gear drives by integrating the dimensional and the configuration design process," *Mechanism and Machine Theory,* vol. 37, pp. 295-310, 3// 2002.
[129] S. Prayoonrat and D. Walton, "Practical approach to optimum gear train design," *Computer-Aided Design,* vol. 20, pp. 83-92, 1988/03/01 1988.
[130] H. Wang and H.-P. Wang, "Optimal engineering design of spur gear sets," *Mechanism and Machine Theory,* vol. 29, pp. 1071-1080, 1994/10/01 1994.
[131] H.-Z. Huang, Z.-G. Tian, and M. J. Zuo, "Multiobjective optimization of three-

stage spur gear reduction units using interactive physical programming," *Journal of Mechanical Science and Technology,* vol. 19, pp. 1080-1086, 2005.
[132] T. Black, "Designing low-inertia instrument drives," *Product Engineering,* vol. 50, pp. 31-33, 1979.
[133] P. Velex and F. Ville, "An analytical approach to tooth friction losses in spur and helical gears—influence of profile modifications," *Journal of Mechanical Design,* vol. 131, p. 101008, 2009.
[134] S. J. Preece, J. Y. Goulermas, L. P. Kenney, D. Howard, K. Meijer, and R. Crompton, "Activity identification using body-mounted sensors—a review of classification techniques," *Physiological measurement,* vol. 30, p. R1, 2009.
[135] A. Avci, S. Bosch, M. Marin-Perianu, R. Marin-Perianu, and P. Havinga, "Activity recognition using inertial sensing for healthcare, wellbeing and sports applications: A survey," in *Architecture of computing systems (ARCS), 2010 23rd international conference on*, 2010, pp. 1-10.
[136] O. D. Incel, M. Kose, and C. Ersoy, "A review and taxonomy of activity recognition on mobile phones," *BioNanoScience,* vol. 3, pp. 145-171, 2013.
[137] S. J. Preece, J. Y. Goulermas, L. P. Kenney, and D. Howard, "A comparison of feature extraction methods for the classification of dynamic activities from accelerometer data," *IEEE Transactions on Biomedical Engineering,* vol. 56, pp. 871-879, 2009.
[138] H.-Y. Lau, K.-Y. Tong, and H. Zhu, "Support vector machine for classification of walking conditions using miniature kinematic sensors," *Medical & biological engineering & computing,* vol. 46, pp. 563-573, 2008.
[139] H. Huang, F. Zhang, L. J. Hargrove, Z. Dou, D. R. Rogers, and K. B. Englehart, "Continuous locomotion-mode identification for prosthetic legs based on neuromuscular–mechanical fusion," *Biomedical Engineering, IEEE Transactions on,* vol. 58, pp. 2867-2875, 2011.
[140] I. C. Gyllensten and A. G. Bonomi, "Identifying types of physical activity with a single accelerometer: evaluating laboratory-trained algorithms in daily life," *IEEE Transactions on Biomedical Engineering,* vol. 58, pp. 2656-2663, 2011.
[141] A. Mannini and A. M. Sabatini, "Gait phase detection and discrimination between walking–jogging activities using hidden Markov models applied to foot motion data from a gyroscope," *Gait & posture,* vol. 36, pp. 657-661, 2012.
[142] H. A. Varol, F. Sup, and M. Goldfarb, "Multiclass real-time intent recognition of a powered lower limb prosthesis," *Biomedical Engineering, IEEE Transactions on,* vol. 57, pp. 542-551, 2010.
[143] Y. Huang, K. B. Englehart, B. Hudgins, and A. D. Chan, "A Gaussian mixture model based classification scheme for myoelectric control of powered upper limb prostheses," *Biomedical Engineering, IEEE Transactions on,* vol. 52, pp. 1801-1811, 2005.
[144] B. Chen, E. Zheng, and Q. Wang, "A Locomotion Intent Prediction System Based on Multi-Sensor Fusion," *Sensors,* vol. 14, pp. 12349-12369, 2014.
[145] B. Chen, E. Zheng, Q. Wang, and L. Wang, "A new strategy for parameter optimization to improve phase-dependent locomotion mode recognition," *Neurocomputing,* vol. 149, Part B, pp. 585-593, 2/3/ 2015.
[146] D. J. Villarreal and R. D. Gregg, "A survey of phase variable candidates of human

locomotion," in *Engineering in Medicine and Biology Society (EMBC), 2014 36th Annual International Conference of the IEEE*, 2014, pp. 4017-4021.
[147] D. J. Villarreal, H. A. Poonawala, and R. D. Gregg, "A Robust Parameterization of Human Gait Patterns Across Phase-Shifting Perturbations," *IEEE Transactions on Neural Systems and Rehabilitation Engineering*, vol. PP, pp. 1-1, 2016.
[148] R. D. Gregg, E. J. Rouse, L. J. Hargrove, and J. W. Sensinger, "Evidence for a Time-Invariant Phase Variable in Human Ankle Control," *PLoS ONE*, vol. 9, p. e89163, 2014.
[149] M. A. Holgate, T. G. Sugar, and A. W. Bohler, "A novel control algorithm for wearable robotics using phase plane invariants," in *Robotics and Automation, 2009. ICRA '09. IEEE International Conference on*, 2009, pp. 3845-3850.
[150] R. D. Gregg and J. W. Sensinger, "Towards biomimetic virtual constraint control of a powered prosthetic leg," *Control Systems Technology, IEEE Transactions on*, vol. 22, pp. 246-254, 2014.
[151] R. D. Gregg, T. Lenzi, L. J. Hargrove, and J. W. Sensinger, "Virtual constraint control of a powered prosthetic leg: From simulation to experiments with transfemoral amputees," *Robotics, IEEE transactions on*, vol. 30, pp. 1455-1471, 2014.
[152] D. Quintero, D. J. Villarreal, and R. D. Gregg, "Preliminary Experiments with a Unified Controller for a Powered Knee-Ankle Prosthetic Leg Across Walking Speeds," in *IEEE Int. Conf. Intelligent Robot Systems*, 2016.
[153] B. J. McFadyen and D. A. Winter, "An integrated biomechanical analysis of normal stair ascent and descent," *Journal of biomechanics*, vol. 21, pp. 733-744, 1988.
[154] L. Torburn, C. M. Powers, R. Guiterrez, and J. Perry, "Energy expenditure during ambulation in dysvascular and traumatic below-knee amputees: a comparison of five prosthetic feet," *Journal of rehabilitation research and development*, vol. 32, pp. 111-111, 1995.
[155] R. Waters, J. Perry, D. Antonelli, and H. Hislop, "Energy cost of walking of amputees: the influence of level of amputation," *J Bone Joint Surg Am*, vol. 58, pp. 42-46, 1976.
[156] C. M. Powers, L. A. Boyd, L. Torburn, and J. Perry, "Stair ambulation in persons with transtibial amputation: an analysis of the Seattle LightFoot," *Journal of rehabilitation research and development*, vol. 34, p. 9, 1997.
[157] J. K. Hitt, T. G. Sugar, M. Holgate, and R. Bellman, "An Active Foot-Ankle Prosthesis With Biomechanical Energy Regeneration," *Journal of Medical Devices*, vol. 4, pp. 011003-011003-9, 2010.
[158] M. Grimmer, M. Holgate, R. Holgate, A. Boehler, J. Ward, K. Hollander, *et al.*, "A powered prosthetic ankle joint for walking and running," *Biomedical engineering online*, vol. 15, p. 141, 2016.
[159] B. E. Lawson and M. Goldfarb, "Impedance & admittance-based coordination control strategies for robotic lower limb prostheses," *Mechanical Engineering*, vol. 136, p. S12, 2014.
[160] A. H. Shultz, "Control methods for powered prostheses to improve mobility and stability in persons with lower limb amputation," Vanderbilt University, 2017.

Appendix A

Optimal Transmission Ratio Selection for Electric Motor Driven Actuators with Known Output Torque and Motion Trajectories

This work concerns motor selection and transmission ratio optimization for applications in which the desired output kinematics and kinetics are known. The objectives of minimizing motor torque and actuator power consumption are treated. A bond graph modeling approach is taken, and analytical optima are presented wherever possible. This work was published as a journal article in the *ASME Journal of Dynamic Systems Measurement and Control* in October of 2017.

A.1 Manuscript A: Optimal Transmission Ratio Selection for Electric Motor Driven Actuators with Known Output Torque and Motion Trajectories

A.1.1 Abstract

This paper presents a method for selecting the optimal transmission ratio for an electric motor for applications for which the desired torque and motion at the transmission output are known a priori. Representative applications for which the desired output torque and motion are periodic and known include robotic manipulation, robotic locomotion, powered prosthetics, and exoskeletons. Optimal transmission ratios are presented in two senses: one that minimizes the root mean square (RMS) of electrical current and one that minimizes the RMS electrical power. An example application is presented in order to demonstrate the method for optimal transmission ratio selection.

A.1.2 Introduction

For a given motor, a common method for the selection of a transmission ratio is to employ a "quasistatic" approach that scales the continuous or short-term torque and/or speed operating characteristics of the motor to the continuous or short-term torque and/or speed operating requirements at the output. This approach essentially uses the transmission ratio to map the rated performance limits of the motor to those of the application. Since this type of approach does not consider motor dynamics, however, it may in the presence of significant dynamic effects in the motor provide a sub-optimal, and in some cases, inappropriate determination of the transmission ratio [86].

In order to provide a more optimal selection of motor and/or transmission ratio, a number of researchers have presented various methods of motor and/or transmission selection that account for the passive dynamic elements present in the motor, transmission, and/or load. In [87], the authors describe a means of selecting an optimal transmission ratio for a motor, assuming a point-to-point motion and a purely inertial load. In [86, 88], the authors present a method for motor selection for an a priori known torque-speed trajectory (i.e., for a generic load). The essential method of [86, 88] was further refined and extended by [89-98]. The work in this field has primarily focused on motor selection [97, 99, 100], setting feasible bounds on transmission ratio selection [86, 91-94], and the optimal selection of the transmission ratio [87, 89, 90, 95, 97, 98].

The work presented in this paper is a further extension and refinement of [86, 88] and the associated extensions of it. This work specifically extends these aforementioned prior works by: 1) providing optimal solutions in terms of minimizing root-mean-squared (RMS) current and RMS electrical power, respectively; 2) presenting these respective optimal

solutions as closed-form analytical solutions (where possible); and 3) presenting the feasible limits of the motor in the context of rated electrical characteristics. This paper also leverages a bond graph formulation to represent the energetic structure of the motor-transmission-load interaction, which the authors employ to diagram the derivation of the transmission optimization expressions. The bond graph formulation is employed to derive new findings regarding the minimization of electrical power consumption and the feasible limitations of transmission ratio choice. The utility of the presented methodology lies in the simplicity of the models presented. The method is intended to be used by designers to quickly size electromechanical actuator components and to quantify the tradeoffs associated with different design decisions.

A.1.3 Methods

The components of an actuator for an electromechanical system, consisting of motor and transmission driving a load, can be schematically represented as shown in Figure 1. In this model, the motor has a torque constant K_τ, rotor inertia J, and electrical terminal resistance R; the transmission has a ratio of N:1 and mechanical efficiency η; and the load is described by a desired angular velocity and torque trajectory defined by $\vec{\dot{\theta}}$ and $\vec{\tau}_{ext}$. It should be noted that the transmission efficiency, η, is assumed to be constant across different values of the transmission ratio, N, as well as across different values of $\vec{\dot{\theta}}$ and $\vec{\tau}_{ext}$. This assumption is reasonable for certain types of transmissions such as belts and chains, but is less reasonable for other transmission types [101]. However, the intention of this methodology is to remain agnostic with respect to transmission type. Should a designer have already decided upon a specific mechanism for the transmission, the model could be updated

with the appropriate dynamic elements associated with that mechanism.

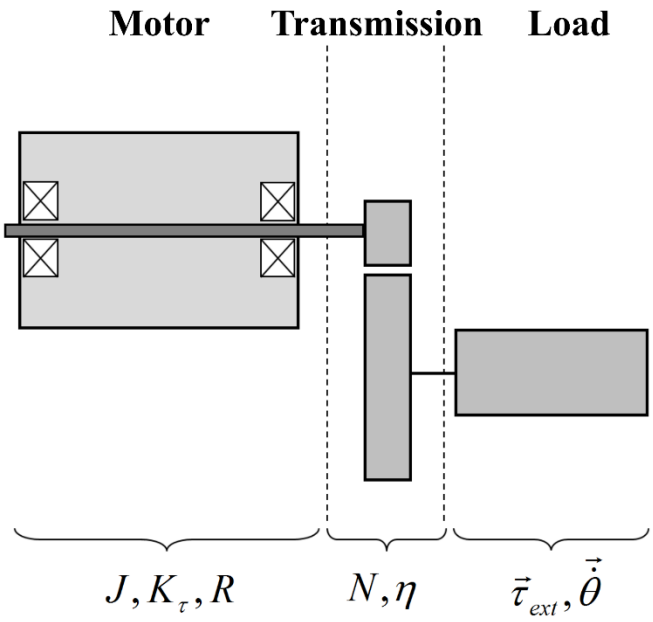

Fig. 1. The electromechanical actuator model treated here is split into three components: the motor, transmission, and load, each with associated constants and parameters.

A.1.3.1 *Minimizing Motor Torque*

For a given motor and desired output angle and torque trajectories (i.e., output kinematics and kinetics), a transmission ratio can be selected to minimize the RMS motor torque, which will in turn minimize the RMS current into the motor, and thus will minimize the Joule heating in the motor windings. A bond graph approach, as first described by [102, 103], provides a useful power-domain-independent framework for formulation of the optimization problem. A bond graph of a motor coupled with a transmission is shown in Figure 2a. In this model, the effort and flow associated with the input are given by τ_m and $\dot{\theta}_m$ (motor torque and angular velocity), respectively. The model additionally incorporates passive inertia and damping behaviors, both associated with the motor flow variable.

Additionally, the transmission is modeled as a linear transformer with transmission ratio N, and the effort and flow associated with the (mechanical) load are given by τ_{ext} and $\dot{\theta}$, respectively. The power loss associated with transmission inefficiency is modeled as a modulated resistance where η is the mechanical efficiency of the transmission. Reflecting the dynamical behavior of the actuator across the transmission and into the load domain yields the bond graph shown in Figure 2b, where the motor impedance consists of the combination of rotational inertia and damping, described by the linear coefficients J and b. It should be noted that causality is not assigned in this model because the results derived from the system are independent of such assignment.

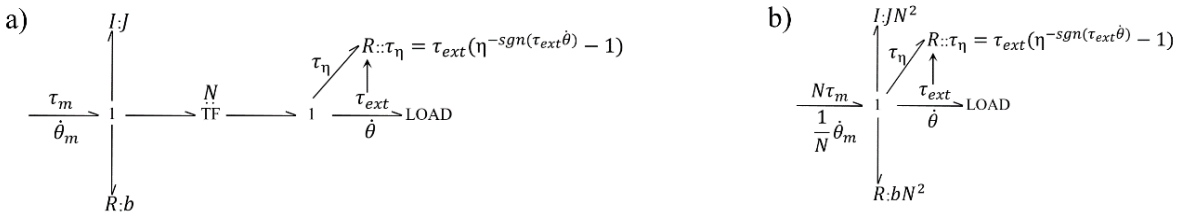

Fig. 2. (a) Shows the bond graph of a mechanical transmission with state-dependent impedances associate with its power source and known output efforts and flows. (b) Shows the same system reflected into the output domain.

In this model, τ_{ext} and $\dot{\theta}$ are known over time and defined by the desired kinematic and kinetic trajectory at the system output. Effort continuity around the 1-junction in Figure 2b yields:

$$N\tau_m = JN^2\ddot{\theta} + bN^2\dot{\theta} + \tau_{ext} + \tau_{ext}\left(\eta^{-\mathrm{sgn}\left(\tau_{ext}\dot{\theta}\right)} - 1\right) \quad (1)$$

Since all bonds are connected to the same common flow junction, the expression (1) becomes a power balance by multiplying both sides of the expression by the common flow ($\dot{\theta}$). The first two terms in the right hand side of (1) represent the output torque lost to the internal

impedance of the actuator. Factoring N^2 out of these two terms yields a simplifying variable, β, given by:

$$\beta = J\ddot{\theta} + b\dot{\theta} \tag{2}$$

The third term on the right hand side of (1) represents the torque delivered to the load of the actuator while the fourth term represents the torque required to overcome transmission inefficiencies. The transmission efficiency is dependent on the net direction of power flow, giving rise to the nonlinear nature of this fourth term. It should be noted that in this model, positive power is defined as power flowing from the motor to the load. In an effort to simplify subsequent expressions, an asymmetric efficiency-based multiplier (ε) is utilized to capture the effects of transmission efficiency:

$$\varepsilon = \eta^{-\mathrm{sgn}\left(\tau_{ext}\dot{\theta}\right)} \tag{3}$$

Utilizing the simplifying terms given in (2) and (3), (1) reduces to the more compact expression:

$$N\tau_m = \beta N^2 + \varepsilon\tau_{ext} \tag{4}$$

From (4), an explicit expression for the input effort (motor torque) can be derived:

$$\tau_m = \beta N + \frac{\tau_{ext}}{N}\varepsilon \tag{5}$$

and the transmission ratio $N = N^*_{\tau_m}$ that minimizes this effort can be found from (5) as:

$$N^*_{\tau_m} = \sqrt{\frac{\varepsilon\tau_{ext}}{\beta}} \tag{6}$$

In the case of an electric motor driven transmission, motor impedance is typically dominated by rotor inertia ($\beta = J\ddot{\theta}$). Additionally, because motor torque τ_m is proportional

to applied current i, the transmission ratio N that minimizes motor torque (6) will also minimize motor current. The solution described by (6), however, is limited to a single instance of torque and angular acceleration, due to the scalar nature of its inputs.

The analysis presented above can be extended to optimize N with respect to a complete desired drive system trajectory defined by $\vec{\tau}_{ext}$ and $\ddot{\vec{\theta}}$ where the vector notation indicates that each variable describes the respective time history over the course of the actuator's actuation cycle. In the vector case, the current consumed by the motor for this desired trajectory can be derived by substituting $\vec{\beta} = J\ddot{\vec{\theta}}$ and $\vec{\tau}_m = K_\tau \vec{\imath}$ into (5) and isolating $\vec{\imath}$:

$$\vec{i} = \frac{\vec{\tau}_{ext}\vec{\varepsilon} + J\ddot{\vec{\theta}}N^2}{K_\tau N} \tag{7}$$

Note that vector multiplication, as used herein, is intended to represent element-wise multiplication. The RMS of this current trajectory can be minimized by choosing the appropriate transmission ratio:

$$RMS(\vec{i}) = RMS\left(\frac{\vec{\tau}_{ext}\vec{\varepsilon} + J\ddot{\vec{\theta}}N^2}{K_\tau N}\right) \tag{8}$$

The transmission ratio N that minimizes (8), the derivation of which can be found in section A.1.7, is given by:

$$N^*_{RMS(\vec{i})} = \sqrt{\frac{RMS(\vec{\tau}_{ext}\vec{\varepsilon})}{RMS(J\ddot{\vec{\theta}})}} \tag{9}$$

It should be noted that (9) is a general expression that encapsulates (6). Additionally, for a purely inertial load ($\vec{\tau}_{ext} = I\ddot{\vec{\theta}}$), (9) reduces to the optimal transmission ratio found previously by Pasch and Seering [87]. Similar findings were also presented in [90, 96, 97].

However, the asymmetric efficiency term is additionally included here in the expression for the optimal transmission ratio. The model presented here also allows for the inclusion of additional impedance terms in the motor such as bearing friction. The dynamic effects considered in this work can be easily altered or extended by changing either the $\vec{\tau}_{ext}$ or β term.

A.1.3.2 *Minimizing Actuator Power Consumption*

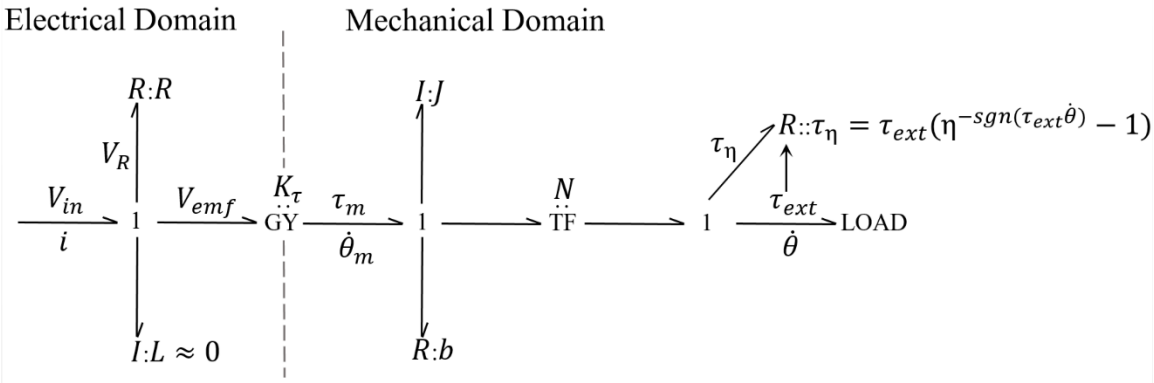

Fig. 3. Shows the bond graph of a DC motor and a mechanical transmission driving a load with desired kinematics and kinetics. The motor electrical inductance is assumed to be negligible.

Electromechanical drive systems may also be concerned with electrical power consumption. As such, a transmission ratio can alternatively be selected such that the electrical energy consumed by the actuator over a cycle is minimized. Figure 3 shows a bond graph model similar to that shown in Figure 2a, but with the electrical domain of the motor included as well. Specifically, the model includes a terminal resistance R, an applied voltage V_{in}, a voltage across the resistor V_R, a current i, and a back EMF voltage V_{emf} . The motor is also assumed here to have negligible electrical inductance ($L \approx 0$), although a non-negligible inductance could be included if needed. From this bond graph model, the below

relations follow:

$$V_{in} = iR + K_\tau N\dot{\theta} \tag{10}$$

$$i = \frac{\tau_{ext}\varepsilon + \beta N^2}{K_\tau N} \tag{11}$$

The product of (10) and (11) provides an expression for the power into the actuator:

$$P_{in} = V_{in} i = \frac{\beta N + \frac{\tau_{ext}}{N}\varepsilon}{K_\tau}\left[\frac{R}{K_\tau}\left(\beta N + \frac{\tau_{ext}}{N}\varepsilon\right) + K_\tau N\dot{\theta}\right] \tag{12}$$

which can be used to find the transmission ratio N that minimizes the input power to the motor:

$$N^*_{P_{in}} = \sqrt[4]{\frac{(\tau_{ext}\varepsilon)^2}{\beta^2 + \left[\frac{K_\tau{}^2\beta\dot{\theta}}{R}\right]}} = \sqrt[4]{\frac{(\tau_{ext}\varepsilon)^2}{\beta^2 + K_m{}^2\beta\dot{\theta}}} \tag{13}$$

where $K_m = \frac{K_\tau}{\sqrt{R}}$, which is sometimes referred to as the motor constant or the speed torque gradient [100, 104, 105].

Solving for an analytical expression for the transmission ratio that minimizes RMS motor power consumption is not tractable because it produces an 8th order polynomial. However, the minima can be found numerically using:

$$N^*_{\vec{P}_{in}} = \arg\min_N \left[RMS\left(\frac{J\ddot{\vec{\theta}}N + \frac{\vec{\tau}_{ext}}{N}\vec{\varepsilon}}{K_\tau}\left[\frac{R}{K_\tau}\left(J\ddot{\vec{\theta}}N + \frac{\vec{\tau}_{ext}}{N}\vec{\varepsilon}\right) + K_\tau N\dot{\vec{\theta}}\right]\right)\right] \tag{14}$$

In (14), it is again assumed that the motor impedance is dominated by the rotor inertia ($\vec{\beta} = J\ddot{\vec{\theta}}$).

A.1.3.3 *Applying Practical Limits to Transmission Ratios*

The solution set of transmission ratios is bounded by the torque, speed, and thermal limitations of a motor, and the optimal transmission ratio(s) previously expressed may not lie within the bounded solution set.

A.1.3.3.1 *Saturation Limits*

The current available to a motor ($\hat{\vec{\imath}}$) during a given actuator output angular velocity trajectory ($\dot{\vec{\theta}}$) is given by:

$$\hat{\vec{\imath}} = \frac{V}{R} - \frac{K_\tau N \left|\dot{\vec{\theta}}\right|}{R} \tag{15}$$

where V is the electrical supply rail voltage. In order for the actuator to satisfy a desired torque trajectory, the current available to the motor must be greater than or equal to the current required by the motor ($\hat{\vec{\imath}} \geq |\vec{\imath}|$), which can be expressed by:

$$\frac{V}{R} - \frac{K_\tau N \left|\dot{\vec{\theta}}\right|}{R} - \left| \frac{J \ddot{\vec{\theta}} N}{K_\tau} + \frac{\vec{\tau}_{ext} \vec{\varepsilon}}{K_\tau N} \right| \geq 0 \tag{16}$$

Every entry in the vector described by (16) must be greater than or equal to zero in order for the actuator to successfully perform the task. The first term in (16) represents the nominal current through the motor while the second term describes the effective current lost to back EMF. The third and fourth terms in (16) describe the current required by the desired trajectory both to overcome the motor's internal impedance and to deliver torque to the load. The range of N for which (16) is satisfied can be easily found numerically by evaluating (16) at different values of N.

The lower bound of this range describes a torque limitation of the motor while the upper bound describes an angular velocity limitation of the motor. If no value of N satisfies (16), then the motor cannot perform the desired task with the supply voltage used. A larger supply voltage (V) increases the solution range of transmission ratios, however, the motor still may encounter thermal limitations.

A.1.3.3.2 *Thermal Limits*

In addition to the saturation limitations on the transmission ratio solution range imposed by the stall torque and no load speed of the motor, the motor is also limited by its thermal dynamics. The RMS of the current trajectory must remain below the maximum continuous current capacity of the motor (i_{cont}). At low transmission ratios, a large current is required to achieve a given maximum output torque. At high transmission ratios, a large current is required to overcome the torques required to overcome passive dynamics of the motor to achieve a given output velocity (i.e., in the case of motor damping) and/or acceleration (i.e., in the case of motor inertia). It is the tradeoff between these two effects that produces the minimization described previously. A lower and upper thermal bound for the transmission ratio (N_{T_L} and N_{T_U}) will be defined as the upper and lower transmission ratios for which the following expression is satisfied:

$$RMS(\vec{i}) = i_{cont} \tag{17}$$

It should be noted that (17), while providing a useful reference regarding the thermal limitations of a motor, provides only a necessary condition on the maximum allowable amount of RMS motor current, not a sufficient one. A motor with RMS current above i_{cont} will exceed the thermal limits of the motor, but a motor with RMS current below i_{cont} will

not necessarily operate within the thermal limits. Short-term peaks in current acting through the thermal dynamics of a motor could be sufficient to exceed allowable winding temperatures. As such, although (17) provides a useful reference, the requisite motor current for a given transmission ratio could also be checked against a thermal model of the motor to ensure that both necessary and sufficient conditions are satisfied [106].

A.1.3.3.2 *Existence of a Transmission Ratio Solution*

The solution set of transmission ratios can be bracketed between the ranges specified by both the thermal limitations and the torque/speed saturation limitations of the motor (range in which the motor can accomplish the task successfully without encountering saturation or thermal limitations). A lower bound for the transmission ratio N_L is the minimum value of N in this range while N_U is the upper bound and largest value of N for this range. The upper and lower bounds are defined by the most restrictive set of transmission ratios for which the motor does not saturate or exceed its thermal limits. It should be noted that if no such range exists, then the motor cannot provide the desired torque and motion trajectories for any transmission ratio.

A.1.4 Design Application

As an example application of the method presented above, consider the design of an electromechanical drive system for the swing phase of a one degree-of-freedom transtibial prosthesis. In this example, a passive mechanism is assumed to provide ankle torque during the stance phase of walking, while an actuated system is used to provide dorsiflexion of the prosthesis during swing phase. In this drive system, the power associated with the powered

push off phase of gait is not supplied by the drive system, allowing a low-powered motor to be utilized. The actuator for this system must be compact and deliver the desired kinematics and kinetics for the application. To determine the actuator design for this system, the kinematics and kinetics of the joint must be determined, candidate motors be selected, and the transmission optimization applied to each candidate motor.

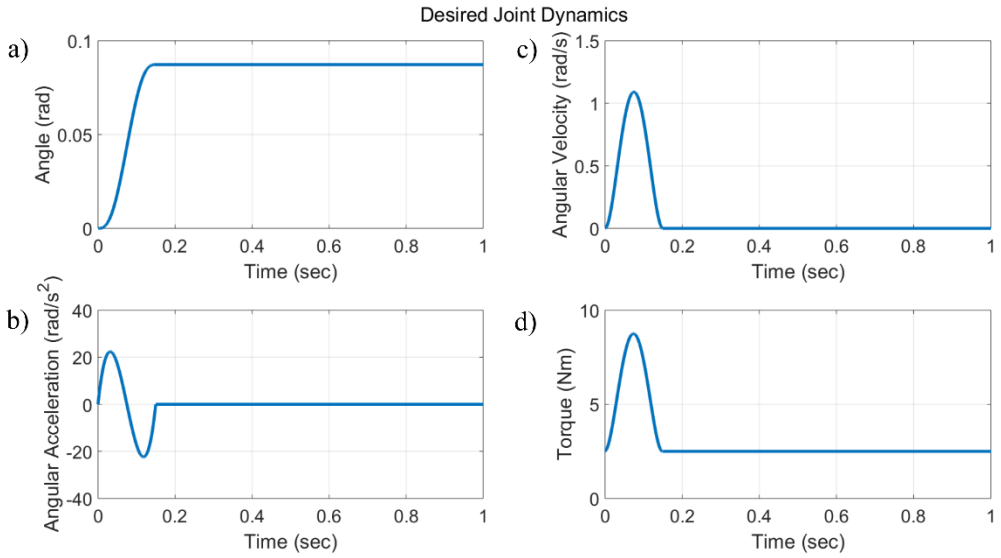

Fig. 4. Desired output dynamics of robotic ankle prosthesis actuator for dorsiflexion of the ankle during level ground walking. (a) ankle angle (b) ankle angular velocity (c) ankle angular acceleration (d) ankle torque.

The necessary actuator kinematics and torque for this application can be seen in Figure 4. It should be noted that viscous damping dominates the system dynamics, and because of this, the optimum transmission ratio described in [87] will not provide an accurate solution for this application. The product of the joint angular velocity and torque yields a curve with qualitatively the same shape as the torque curve seen in Figure 4d with a peak joint power over the cycle of 9.5 Watts.

A.1.4.1 *Candidate Motor Selection*

Based on the peak joint power requirement of 9.5 Watts, two candidate motors were selected for the application: a Maxon EC16 8 Watt motor and a Maxon EC45 12 Watt motor. A brief overview of the relevant motor specifications for both candidate motors is given in Table 1. In this design example, the supply voltage was set at 48 Volts.

Table 1: Candidate Motors

	EC 16	**EC 45**
Nominal Power (W)	8	12
Rotor Inertia (J)(gcm^2)	0.85	52.3
Torque Constant (K_τ)(mNm/A)	18.7	30.5
Supply Voltage (V)(Volts)	48	48
Max Continuous Current (i_{cont})(A)	0.461	0.766
Terminal Resistance (R)(Ω)	20.5	6.42

A.1.4.2 *Transmission Optimization*

For each of the two candidate motors and the desired kinematic and kinetic output trajectories shown in Figure 4, the RMS current and RMS power of the motor were calculated for a wide range of transmission ratios using the previously described method. In this analysis, transmission mechanical efficiency was assumed to be 80% (η=0.8). Additionally, the transmission ratios that minimize each of these two quantities were calculated using (9), (10), and (14). Transmission bounds were also calculated using (16) and (17). A plot of these curves, their minima, and the feasible transmission bounds are shown in Figure 5. The thermal limits, given by (17), are plotted as dark gray vertical dashed lines while the torque and speed saturation limits given by (16) are plotted as light gray vertical dashed lines. It should be noted that the upper thermal and saturation bounds are off the right end of the plot

for the EC 16 motor in Figure 5. The double y-axis plot allows for all of the relevant curves and points to be plotted on a single plot for each motor and transmission combination generating the desired output trajectories. The RMS motor current is plotted against the left y-axis while the RMS motor power is plotted against the right y-axis. The maximum continuous current, as given by the motor data sheets, is also plotted as a dashed horizontal line to give reference for the current curves with respect to the limitations of the motor. Transmission selection should be performed by attempting to minimize the motor current and/or power associated with performing the desired activity (minimums of the curves in Figure 5) subject to the feasible limitations imposed by saturation and thermal limits of the motor and electrical supply (vertical lines in Figure 5).

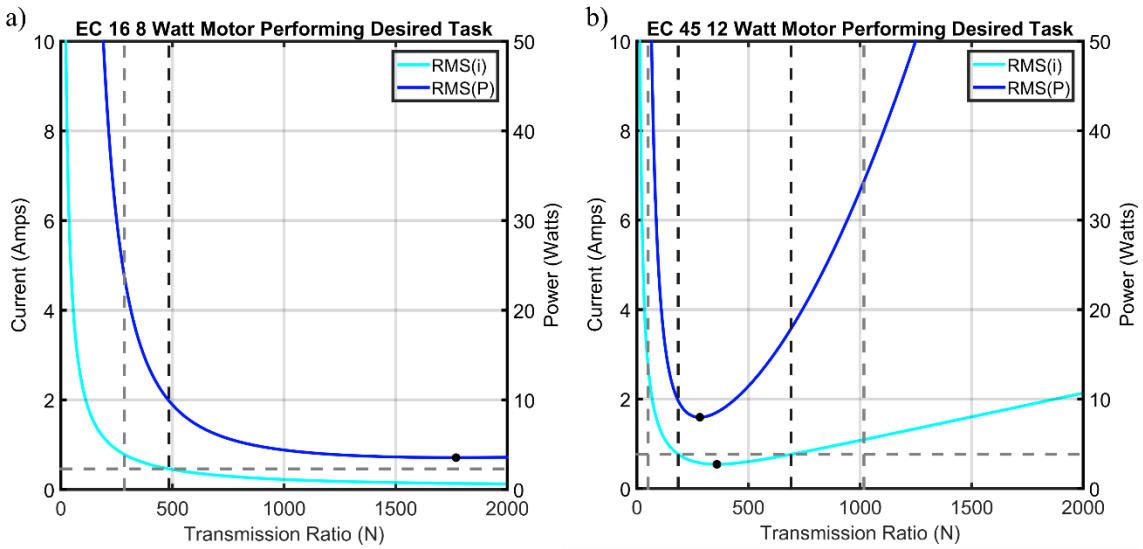

Fig. 5. Actuator RMS current, peak current, and RMS power plotted against transmission ratio with feasible transmission bounds marked by vertical dashed lines. Dark dashed lines indicate thermal bounds, gray vertical dashed lines indicate a torque or speed limitation, and the horizontal dashed lines is the motor's specified maximum continuous current. Current values are plotted against the left y axis while power values are plotted against the right y axis. Two motors executing the same task are plotted in this figure: (a) EC 16 8 Watt (The upper thermal bound is off the right end of the plot) (b) EC 45 12 Watt.

From Figure 5, a motor and transmission pairing can be made with knowledge of that

pairing's effect on important system performance parameters. The RMS current of the motor should be minimized to minimize Joule heating of the motor while the RMS power curve should be minimized for the longevity of a battery-powered device. Additionally, the flatness of the curves can be examined in the regions of interest to see if small changes in transmission ratio have large effects on the performance metric curves (RMS($\vec{\imath}$) and RMS($\vec{P}_{in}$) as a function of N). By examining the shapes of these curves, small transmission ratios can be chosen while still approaching the minima of the performance metric curves.

The difference in the shapes of the curves in Figure 5 for the two motors can be largely attributed to the motors' construction. The EC 16 motor is an internal rotor brushless motor while the EC 45 is an external rotor flat brushless motor. The difference in construction is reflected in the differences in the two motors' rotor inertias and torque constants (Table 1). The high torque density of external rotor motors allow for small transmission ratios, but at the cost of high rotor inertias [107, 108]. These high rotor inertias become significant to the system dynamics at high transmission ratios due to reflected inertia. The effects of the large rotor inertia can be seen in Figure 5b in which the performance metric curve minima are much more pronounced than the internal rotor counterpart seen in Figure 5a. At high values of N, the reflected inertia becomes very large and the motor consumes large amounts of current to in order to accelerate and decelerate the rotor inertia.

For this application, the EC 45 motor would be paired with a transmission ratio of approximately 250:1 in order to minimize both the maximum motor current and RMS motor power. The EC 16 motor would be paired with a transmission ratio of approximately 600:1 in order to stay within the transmission bounds while maintaining a minimal transmission

and minimize power consumption. The plots seen in Figure 5 help to illustrate tradeoffs in the actuator design. The shapes of the curves, the feasible transmission ratio ranges, as well as the minimums can aid in the actuator design process. The tradeoffs illustrated by this method must be balanced with other design constraints such as size or mass limits or other characteristics of the actuator.

A.1.5 Discussion

As demonstrated by the previous example, consideration of the dynamics of a motor is important in the choice of motor and transmission ratio, particularly for applications involving substantial variation in motion. By including the dynamic characteristics of a motor in a systematic process for selecting a transmission ratio, higher performance actuation systems can be designed. The method of actuator design and transmission ratio selection presented here provides a quantitative method of examining the tradeoffs between different transmission ratio choices on relevant system performance characteristics. Specifically, the tradeoffs between motor current consumption and power consumption are considered. In this regard the curves as seen in Figure 5 may be of more use to designers than the specific optima described in this paper. From this standpoint, a designer can balance the performance characteristics that are most relevant or critical for a given application. Similarly, different motors performing the same desired task can be quantitatively compared. The relative size, power consumption, and electrical requirements of different candidate actuators can be quickly examined in this way.

As can be seen from (16), increasing the supply voltage to the motor can increase the size of the solution set of transmission ratios for the motor. However, there is a limit to how

much the supply voltage can be increased. At some point, torque and speed saturation will no longer be the limiting factor constraining the range of transmission ratios for the actuator, and instead the thermal limitations of the motor will be the most constraining factor. A supply voltage and transmission ratio may be chosen simultaneously using this method so that the smallest electrical supply that still allows for successful actuator performance is chosen. This insight may enable one to more appropriately size the electrical supply voltage for a given actuator.

This simple model-based method provides a procedure by which transmission ratio, N, can be chosen, although the physical implementation of the transmission (gearhead, cable drive, etc.) must be determined by the designer. The inclusion of transmission efficiency in this model also allows designers to examine the effects of using different transmission types with different efficiencies for the same application.

The previously-mentioned method presented by [2] is intended for purely inertial loads, while the method presented in this paper can accommodate an arbitrary desired output kinematic and kinetic trajectory. For systems in which the inertial torques dominate the system kinetics, the method presented in this paper will yield similar optimal solutions to the Pasch and Seering method, and for systems with purely inertial loads ($\vec{\tau}_{ext} = I\ddot{\vec{\theta}}$), the two methods will yield identical solutions.

One limitation of this method is that it assumes that transmission efficiency is constant across different values of the transmission ratio. To accommodate for this limitation, an explicit expression for transmission efficiency as a function of transmission ratio, torque, and velocity could be substituted into the equations described above and the new minima could be found either analytically or numerically. Another limitation to the

method is that it does not include the inertia of the transmission itself. However, if the transmission inertia is significant, the torque required to accelerate and decelerate the transmission inertia can be included in the desired kinetic trajectory, thereby accounting for this impedance. It should also be pointed out that this method assumes that power can flow both into and out of the actuator. Because of this, there is an implicit assumption that the actuator is being controlled by a servoamplifier capable of regeneration.

The treatment of motor dynamics in the selection of transmission ratio also illuminates the fact that high transmission ratios are not always more beneficial for achieving a desired torque trajectory. As can be seen in Figure 5b, high transmission ratios decrease system performance due to the effects of the reflected rotor inertia. Even in cases of small motor inertia, there is a plateau beyond which larger transmission ratios produce only small gains in current and power minimization. In fact, for any motor performing any application, the motor current and power will approach infinity at both very small and very large transmission ratios, suggesting an optimum value of N will always assume an intermediate value between these two extremes.

A.1.6 Conclusion

The authors have presented here an extension of prior literature focused on the optimal selection of a transmission ratio. In particular, this work considers the influence of passive electrical and mechanical properties of the motor on transmission selection for a general load, and extends prior work on the subject by 1) providing optimal solutions in terms of electrical power, specifically in the sense of minimizing RMS current and RMS electrical power, respectively; 2) presenting these respective optimal solutions in closed-

form analytical manner (where possible); and 3) presenting the feasible limits of the motor in the context of rated electrical characteristics. In addition to providing a quantitative solution, the method makes clear that in general, an optimal transmission ratio will exist between a lower bound associated with meeting steady-state output torque requirements, and an upper bound associated with dynamic effects in the motor, which are exacerbated at higher transmission ratios.

A.1.7 Derivation of RMS Minima

It should be noted that all vector operations in the main body of the paper are element-wise multiplication, but vector operations in section A.1.7 obey standard vector operations and "$\circ$" indicates element-wise multiplication.

To minimize (8), an explicit expression of RMS($\vec{\imath}$) can be written:

$$RMS(\vec{i}) = \sqrt{\frac{\vec{i}\,\vec{i}^{\,T}}{size(\vec{i})}} \tag{18}$$

In order to minimize (18) and subsequently (8), the numerator inside the radical in (18) should be minimized. This minimization is done by taking the derivative of this numerator with respect to N, setting that expression equal to zero and solving for N:

$$\frac{\partial \vec{i}\,\vec{i}^{\,T}}{\partial N} = 2\vec{i}\left(\frac{\partial \vec{i}}{\partial N}\right)^{T} = 0 \tag{19}$$

Substituting (7) for $\vec{\imath}$ in (19), the following expression can be derived:

$$\frac{2}{K_\tau}\left(\frac{\vec{\varepsilon}\circ\vec{\tau}_{ext}}{N} + J\ddot{\vec{\theta}}N\right)\left(\frac{-\left(\vec{\varepsilon}\circ\vec{\tau}_{ext}\right)^{T}}{N^2} + J\ddot{\vec{\theta}}^{T}\right) = 0 \tag{20}$$

The expression in (20) can then be simplified to an expression in which each term is a

scalar:

$$\frac{2}{K_\tau}\left(\frac{-(\vec{\varepsilon}\circ\vec{\tau}_{ext})(\vec{\varepsilon}\circ\vec{\tau}_{ext})^T}{N^3}+J^2N\ddot{\vec{\theta}}\ddot{\vec{\theta}}^T\right)=0 \tag{21}$$

and subsequently solved for N:

$$N=\sqrt[4]{\frac{(\vec{\varepsilon}\circ\vec{\tau}_{ext})(\vec{\varepsilon}\circ\vec{\tau}_{ext})^T}{J^2\ddot{\vec{\theta}}\ddot{\vec{\theta}}^T}} \tag{22}$$

This expression for N can then be simplified to match the expression seen in the primary text (23).

$$N^*_{RMS(\vec{i})}=\sqrt{\frac{RMS(\vec{\varepsilon}\circ\vec{\tau}_{ext})}{RMS(J\ddot{\vec{\theta}})}} \tag{23}$$

Appendix B

On the Design of Power Gear Trains: Insight Regarding Number of Stages and Their Respective Ratios

This work concerns the design of multistage gear trains for maximizing efficiency, maximizing acceleration, or minimizing transmission mass. A formulation for optimally selecting the number of stages in the gear train and selecting the gear ratios of each stage is presented and used to highlight implications for the design of gear trains. This work was published as a journal article in *PLOS ONE* in June of 2018.

B.1 Manuscript B: On the Design of Power Gear Trains: Insight Regarding Number of Stages and Their Respective Ratios

B.1.1 Abstract

This paper presents a formulation for selecting the stage ratios and number of stages in a multistage transmission with a given desired total transmission ratio in a manner that maximizes efficiency, maximizes acceleration, or minimizes the mass of the transmission. The formulation is used to highlight several implications for gear train design, including the fact that minimizing rotational inertia and mass are competing objectives with respect to optimal selection of stage ratios, and that both rotational inertia and mass can often be minimized by increasing the total number of stages beyond a minimum realizable number. Additionally, a multistage transmission will generally provide maximum acceleration when the stage ratios increase monotonically from the motor to the load. The transmission will have minimum mass when the stage ratios decrease monotonically. The transmission will also provide maximum efficiency when the corresponding stages employ constant stage

ratios. This paper aims to use this optimization formulation to elucidate tradeoffs between various common objectives in gear train design (efficiency, acceleration, and mass).

B.1.2 Introduction

Electric motors are commonly employed to actuate drive systems, but generally provide power in a high speed, low torque power regime relative to the drive applications they are intended to actuate. In order to address this disparity, gear transmissions are commonly employed to transform the high speed, low torque output power of the motor to the requisite higher torque, lower speed power regime of the drive system. Such gear transmissions are commonly of the multistage [109, 110] or planetary types [111, 112]. This paper describes methods of optimally selecting gear trains of the multistage type. Drive systems with large transmission ratios (e.g., on the order of 100:1) are common in modern electric motor-driven machines. Such transmissions are typically split into multiple stages for the purposes of efficient packaging and practical constraints on transmission size. When considering the design of a multistage transmission of a given overall transmission ratio, a designer must determine the most appropriate number of stages, and the stage ratio associated with each. This paper considers the problem of selecting number of stages, and stage ratios, from the perspective of either maximizing transmission efficiency, maximizing rotational acceleration capabilities, or minimizing mass.

The general objective of optimal gear transmission design is not new – various approaches have been presented by others previously, such as those described in [95, 109, 110, 113-132]. Of the works most relevant to this paper, among the earliest is [109], in which the authors minimized the rotational inertia reflected onto the motor shaft of a two-stage

transmission with a pre-specified total transmission ratio, using the assumption of size-invariant pinions for each stage. The optimal stage ratios for multistage transmissions with more than two stages was also presented in that paper, although in a graphical manner. An iterative, numerical method for optimizing multistage transmissions with respect to minimizing transmission rotational inertia was presented in [110, 114, 116]. Numerical multi-criterion optimization methods for transmissions were also presented in [117-124], which consider objective functions such as gear train volume and efficiency. Various optimization algorithms have also been described for the problem of choosing stage ratios of a gear train in which each gear is constrained to have a predetermined number of teeth [125, 126]. In terms of selecting the number of stages in a gear train, [110] provides an analytical solution for the number of stages that should be chosen to minimize the reflected inertia of a transmission.

This paper presents a formulation for the design of a multistage gear train that selects stage ratios in a manner that maximizes transmission efficiency, maximizes rotational acceleration, or minimizes mass for a given desired total transmission ratio. The problem is formulated as a constrained multivariate optimization problem for any number of stages n, and can be used with a wide variety of stage scaling criteria. The scaling criterion employed in this manuscript is intended for power gear trains, and, as a result, is derived to provide constant tooth stress across the stages. In addition to presenting optimal stage ratio formulations, the paper describes some implications of these formulations with respect to gear train design, specifically with respect to how these performance characteristics relate to number of stages and variation in stage ratios.

Unlike prior related works [1-23], this paper provides formulations for the optimal

efficiency, acceleration, and mass, respectively, as a function of number of stages and stage ratios, for a given total transmission ratio. The authors note that, this paper also provides a topological context for the solution presented in [2]. Specifically, [2] does not provide information regarding the local curvature around the optimal solution, and thus does not provide information regarding the sensitivity of the optimal solution as a function of the number of stages. Without this information, a designer is unable to assess the trade-offs entailed in a sub-optimal solution, which is of fundamental importance in the design process. In fact, the relevant objective function, as constructed herein, is quite flat around the optimal solution for most applications, and as such, employing the solution presented in [110], although mathematically correct, would often result in an infeasibly large number of stages. By examining the topology of the objective function, the (maximum rotational acceleration) solution presented here enables a more knowledgeable selection of stages, which can provide near-optimal performance in a feasible transmission configuration. This paper additionally examines the optimal design of gear trains with respect to multiple different objective functions, and subsequently illustrates the inherent tradeoff between mass and inertia in the gear train design process. This work allows a designer to select gear train parameters with knowledge of how design decisions might affect multiple design objectives.

B.1.2 Formulation

Let n be the number of stages in a transmission with a total transmission ratio (i.e., reduction ratio) of $N:1$, and let the respective stage ratio, s_i, be the transmission ratio corresponding to the i^{th} stage of the transmission (where the stage index i increases from the motor to the load). The n stage ratios must multiply to equal the total desired

transmission ratio N, as expressed by the following constraint equation:

$$\left(\prod_{i=1}^{n} s_i\right) - N = 0 \tag{1}$$

In the following sections, expressions for the transmission efficiency, maximum achievable acceleration, and transmission mass are developed as functions of the stage ratios. A representative 3-stage ($n = 3$) transmission can be seen in Figure 1 which defines key design variables.

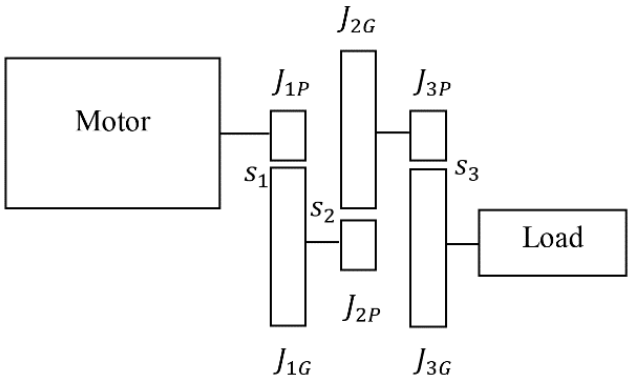

Figure 1: Schematic of a multistage transmission consisting of a motor, transmission, and load. The inertia of a gear or pinion is denoted as J with the first subscript indicating the stage of the transmission. The second subscript denotes if a component is a gear (G) or pinion (P). The stage ratio of the i^{th} stage is denoted by s_i.

B.1.2.1 *Maximum Gear Train Efficiency*

Gear train efficiency is important in applications in which power consumption or maximum output torque are primary concerns. The total transmission efficiency, η_T, is calculated as the product of the individual stage efficiencies, η_i (2).

$$\eta_T = \prod_{i=1}^{n} \eta_i \tag{2}$$

The efficiency of a single stage of a spur or helical gear train can be calculated as described in [133]:

$$\eta_i = 1 - \mu K - \mu K s_i \tag{3}$$

where μ is the coefficient of friction between the gears (typically between 0.05 and 0.15) and K is a constant containing information about the gear geometry as follows:

$$K = \frac{\pi}{Z_1} \frac{1}{\cos(\beta)} \varepsilon_\alpha \Lambda \tag{4}$$

where Z_1 is the number of teeth on the pinion in the mesh, β is the base helix angle (for helical gears), ε_α is the profile contact ratio, and Λ is the loss factor as described in [133]. These efficiency equations of a single stage (3-4) are a reorganization of equation (26) in [133]. The set of s_i that maximizes (2), subject to the constraint (1), will provide the maximum possible efficiency for the multistage transmission.

B.1.2.2 *Maximum Achievable Acceleration*

The maximum (no-load) acceleration per unit torque of the drive system (normalized to the first pinion of the gear train) can be described by:

$$\frac{\ddot{\theta}}{\tau_m} = \frac{\eta_T J_{1P}}{J_m} \tag{5}$$

where τ_m is the motor torque, $\ddot{\theta}$ is the motor acceleration, J_m is the transmission inertia reflected onto the motor, and J_{1P} is the inertia of the first stage pinion. The size of the first pinion in the gear train is fully determined by the torque and speed of the motor, and it is therefore convenient to normalize the reflected inertia by the inertia of the first stage pinion, (J_{1P}). This inertia normalization ($\frac{J_m}{J_{1P}}$) essentially removes absolute sizing and choice of gear material from the problem.

In order to maximize the acceleration capabilities of a transmission, the right hand side of (5) must be maximized with respect to the stage ratios. However, the reflected inertia of the transmission onto the motor must also be expressed in terms of the stage ratios of the transmission. This problem has been treated in other works [109, 110, 113, 114, 132] and can be written as follows for an n-stage transmission where n>1:

$$J_m = J_{1P} + \sum_{i=1}^{n-1}\left[\left(J_{iG} + J_{(i+1)P}\right)\left(\frac{1}{\prod_{j=1}^{i} s_j}\right)^2\right] + J_{nG}\left(\frac{1}{\prod_{k=1}^{n} s_k}\right)^2 \quad for \quad n > 1 \qquad (6)$$

where J_{iP} is the rotational inertia of the i^{th} pinion, and J_{iG} is the rotational inertia of the i^{th} gear. The set of s_i that maximizes (5), subject to the constraint (1), results in a multistage gear train that will provide the maximum achievable acceleration at the output.

It should be noted that several prior works consider the problem of minimizing rotational inertia [109, 110, 113, 114, 132] and the corresponding implications for maximizing output acceleration. The formulation presented here considers the objective of maximizing rotational acceleration by considering both inertia and efficiency, since both are functions of the stage configuration, and both affect output acceleration.

B.1.2.3 *Minimum Gear Train Mass*

The normalized mass of an n-stage transmission, M, can be calculated by adding the mass of the pinions and gears of each stage (m_{iP} and m_{iG}, respectively) and normalizing this quantity by the mass of the first stage pinion:

$$M = \frac{\sum_{i=1}^{n} (m_{iP} + m_{iG})}{m_{1P}} \tag{7}$$

This normalization is performed to remove absolute sizing and material selection from the problem. The set of s_i that minimizes (7), subject to the constraint (1), results in a multistage gear train with the minimum possible transmission mass.

B.1.2.4 *Scaling for Constant Gear Stress*

Although normalization of the respective objective functions by the first-stage pinion removes overall scale and material selection from the optimization problem, a relationship is still required to inform the manner in which each successive pinion (i.e., gearset) should be scaled relative to the first. A reasonable assumption in this regard is that all gears are formulated from the same material, and each is stressed to the same maximum bending stress (i.e., each gear is designed to operate with the same factor of safety). A scaling relation can be derived by considering a standard model of bending stress within a gear tooth [101]:

$$\sigma = \frac{2\tau P}{dFY} \tag{8}$$

where τ is the pinion torque, P is the diametral pitch, F is the face width, d is the pitch diameter, and Y is the Lewis form factor. For simplification, it is assumed that pinions of successive stages have the same Lewis form factor (Y remains constant across successive stages). This assumption is reasonable given that pinions typically employ the minimum number of possible teeth, and gears with similar numbers of teeth have similar Lewis form factors. Imposing constant stress at the pinions of two successive stages of a gear train leads to the following expression:

$$\frac{2\tau_i P_i}{d_i F_i Y} = \frac{2 s_i \tau_i P_{i+1}}{d_{i+1} F_{i+1} Y} \tag{9}$$

where the "i" subscript indicates the first of the two stages, a "$i+1$" subscript indicates the second of the two stages, and where s_i is the ratio of the first of these two stages. Assuming that pinions of successive stages have the same number of teeth and noting that the diametral pitch is the number of gear teeth divided by the pitch diameter, the following scaling ratio is determined:

$$\frac{d_{i+1}}{d_i} = \frac{P_i}{P_{i+1}} \tag{10}$$

A simple approximation of the relationship between diametral pitch (P) and face width of a gear (F) can also be assumed such that the face width of a gear is inversely proportional to the gear's diametral pitch ($F \propto \frac{1}{P}$), which provides a reasonable approximation of accessible geometric data for commercially available gears. This inverse proportionality assumption leads to a secondary gear scaling ratio between face width and pitch:

$$\frac{F_{i+1}}{F_i} = \frac{P_i}{P_{i+1}} \tag{11}$$

Substituting (10) and (11) in to (9) and isolating the stage ratio, s_i, yields the following pinion scaling relationship for two successive stages in a spur gear train such that each pinion is subject to the same stress:

$$\frac{F_{i+1}}{F_i} = \frac{d_{i+1}}{d_i} = \frac{P_i}{P_{i+1}} = s_i^{\frac{1}{3}} \tag{12}$$

The expression presented in (12) matches the empirical scaling recommendations described in [110]. Note that this expression assumes the meshing gears and pinions have the same

face widths. It should also be noted that this assumption neglects the effect of speed (i.e., pitch-line velocity) on gear stress, but in the context of the optimization, neglecting such effects are not expected to substantially affect the solution.

The relationships in (12) must be expressed such that the ratio of the mass and inertia of any gear or pinion to the mass or inertia of the first pinion can be expressed as a function of the stage ratios and known constants. By further assuming: 1) the inertia of each gear and pinion is modeled as that of a solid cylinder with diameter equal to the pitch diameter of the gear, and 2) all gears and pinions are assumed to be constructed of the same material (i.e., all have the same material density), the "uniform maximum stress" pinion scaling condition can be expressed as follows:

$$\frac{J_{iP}}{J_{1P}} = \begin{cases} 1 & for \quad i = 1 \\ \left(\prod_{k=1}^{i-1} s_k \right)^{\frac{5}{3}} & for \quad i > 1 \end{cases} \tag{13}$$

$$\frac{J_{iG}}{J_{1P}} = \begin{cases} s_i^{\,4} & for \quad i = 1 \\ \left(\prod_{k=1}^{i-1} s_k \right)^{\frac{5}{3}} s_i^{\,4} & for \quad i > 1 \end{cases} \tag{14}$$

$$\frac{m_{iP}}{m_{1P}} = \begin{cases} 1 & for \quad i = 1 \\ \prod_{k=1}^{i-1} s_k & for \quad i > 1 \end{cases} \tag{15}$$

$$\frac{m_{iG}}{m_{1P}} = \begin{cases} s_i^{\,2} & for \quad i = 1 \\ \left(\prod_{k=1}^{i-1} s_k \right) s_i^{\,2} & for \quad i > 1 \end{cases} \tag{16}$$

Although more complex scaling assumptions could be adopted (e.g., by incorporating velocity considerations), the expressions given by (13-16) likely capture the most salient

design relations employed in many multistage gear design problems. It should be noted, however, that different scaling assumptions (such as those for instrument gear trains or different types of transmissions) could be applied to the optimization formulation by adapting the right hand sides of (13-16).

B.1.3 Examples and Design Implications

The optimization of (2), (5), and (7) subject to the constraint expressed in (1) was performed in MATLAB for a representative design scenario using the constrained nonlinear multivariate optimization tool, *fmincon*. The optimal stage ratios can be calculated with respect to each objective function (maximum efficiency, maximum acceleration, and minimum mass) for various numbers of stages and total transmission ratios (n and N). In the example presented here, a total transmission ratio of 250:1 was examined ($N = 250$). The gear geometry and friction parameters used in the analysis were taken from [133] and are as follows: $\mu = 0.05$, $Z_1 = 12$ (consistent with assumptions of minimum teeth on the pinion), $\beta = 0$, $\varepsilon_\alpha = 1.2$, and $\Lambda = 0.5$. It should be noted that when the friction coefficient is set to zero, the gear efficiency is 100%, and the maximum acceleration optimization is the same as the minimum reflected inertia optimization performed in [110, 113, 114, 132]. For this example system, the stage ratio selection was evaluated for $n = 3$ to $n = 10$ to examine how different numbers of stages affected both the stage ratio selection and overall performance metrics (efficiency, acceleration, and mass). Transmissions with more than ten stages were not investigated since these designs exceed the optimal number of stages as determined by [110] for this design scenario.

B.1.3.1 *Implications Regarding Stage Ratios*

The optimal stage ratios with respect to the three objective functions for a 4-stage ($n = 4$) transmission with a total ratio of 250:1 can be seen in Figure 2. This figure depicts the trends in optimal stage ratios for the different optimization criteria. The authors note that these trends are consistent across large values of N common in multistage transmissions. Specifically, for purposes of achieving maximum efficiency, the stage ratios in each stage of the gear train should all be equal; for purposes of achieving maximum acceleration, the stage ratios of the various stages should increase monotonically from the motor towards the load; and for purposes of achieving minimal transmission mass, the stage ratios should decrease from the motor towards the load. There is, therefore, a direct tradeoff between mass minimization and acceleration maximization (i.e., essentially rotational inertia minimization) in the design of a multistage power gear transmission. This tradeoff is significant, as the minimum mass solution decreases the acceleration by 51% relative to its optimum, while the maximum acceleration solution increases the mass by 19% relative to its optimum, for the case ($n = 4$, $N = 250$) considered here.

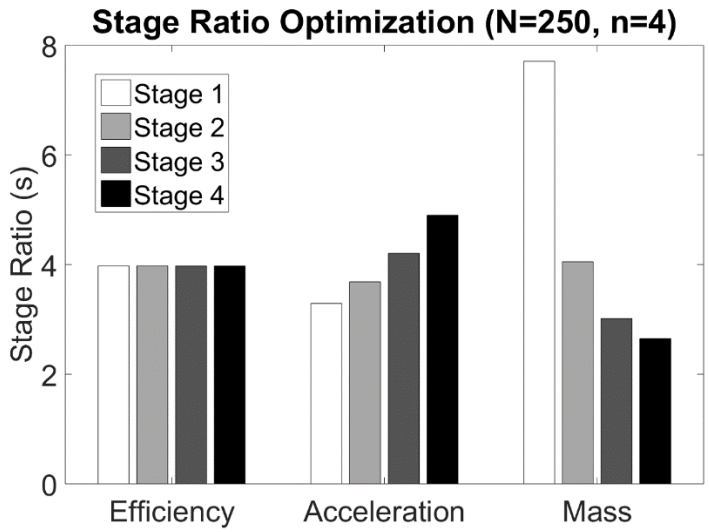

Figure 2: A bar plot showing the distribution of stage ratios for a 4-stage transmission with a total ratio of 250:1. The ratios of each of the 4 stages are selected to optimize one of three objective functions: efficiency, normalized acceleration, and normalized mass. The stage ratio values for these transmissions are shown as darker shades of gray moving from the motor to the load.

B.1.3.2 *Implications Regarding Number of Stages*

For a desired total ratio of 250:1, stage ratios were optimized with respect to the three objective functions (efficiency, acceleration, and mass) for various values of n ($3 \le n \le 10$), and the efficiency, normalized acceleration capability, and normalized mass of the resulting transmissions were then calculated using (2), (5), and (7), respectively. The results of this analysis can be seen plotted against the number of stages in Figure 3. The transmissions optimized for efficiency, acceleration, and mass are plotted in solid light blue, dashed medium blue, and dotted dark blue respectively. This analysis lends insight into the selection of the number of stages in a transmission. Specifically, as can be seen in Figure 3a, the efficiency of the various transmissions peak at approximately 4-5 stages. The transmissions designed to maximize efficiency obtain higher efficiencies than the ones optimized for acceleration and mass, but the difference between the overall efficiency values is not substantial. In fact, the range of transmission efficiency obtainable by varying the number of stages in the transmission is also very small (approximately 6% change in efficiency from $n = 3$ to $n = 10$).

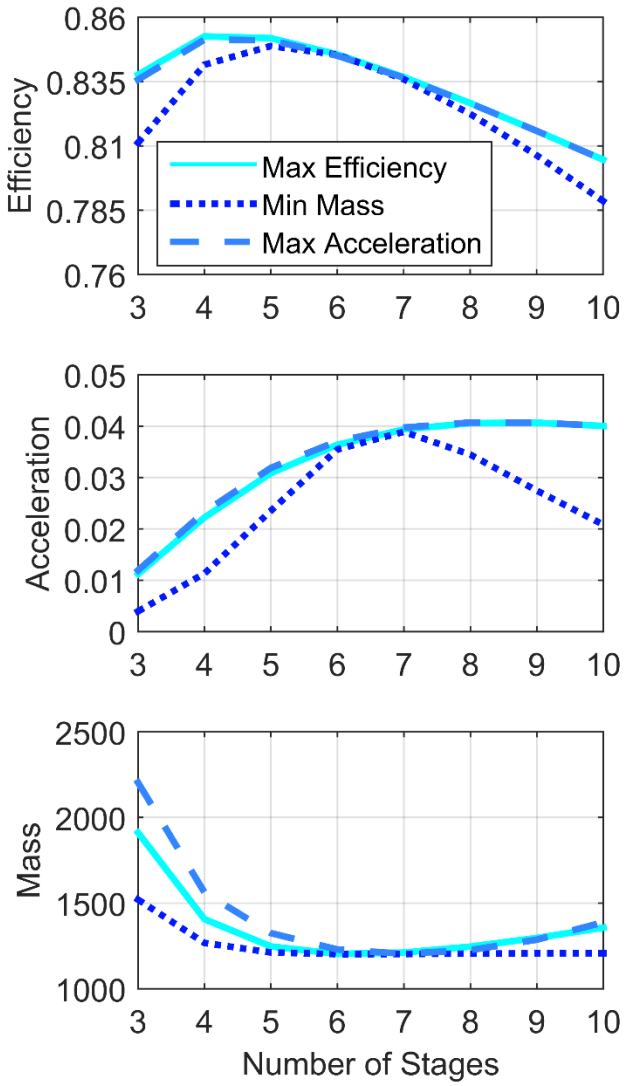

Figure 3: The objective function evaluations once the stage ratios have been selected to maximize efficiency (solid light blue), maximize normalized acceleration (dashed medium blue), or minimize normalized mass (dotted dark blue). The objective functions evaluated are transmission efficiency (a), normalized acceleration (b), and normalized mass (c).

Figure 3b shows how the normalized acceleration properties vary with the number of stages in the transmission. As can be seen, adding additional stages to the transmission significantly increases the acceleration capabilities of the system up to a point, but an upper limit exists in all cases. In this example, the acceleration capabilities increase rapidly from 3

to 4 stages, but the performance increases become less significant as more stages are added. In fact, the local curvature of this objective function around the maxima ($n = 8$) is relatively flat, indicating that a designer could choose significantly fewer than the optimal number of stages without substantially compromising maximum acceleration.

Figure 3c shows that adding additional stages to a transmission can significantly decrease its mass, up to a point. It should be noted that the local curvature of Figure 3c is relatively flat around its minima ($n = 6$), but relatively steep between 3 and 5 stages indicating that the most of the improvements that can be made in terms of minimizing mass can be done with fewer than 6 stages. It should also be noted that when the stage ratios are selected to minimize mass, the transmission mass is significantly less than if the stage ratios are selected to maximize either of the other two objective functions, particularly for 3 or 4 stage transmissions.

It is important to note that when optimizing the stage ratios for efficiency, acceleration, or mass, the same general trends hold with respect to the number of stages in Figure 3a-c. This indicates that the selection of the number of stages of a transmission has a larger effect on the performance metrics treated here than does the selection of the individual stage ratios of the transmission.

For the case of $N = 250$, a 3-stage and a 4-stage transmission, both optimized for maximum efficiency, are shown to scale in Figures 4a and b, respectively. The 3-stage transmission employs three equal stages of 6.3:1, while the 4-stage transmission employs four equal stages of 4.0:1 each. As indicated by the optimization, the 4-stage transmission reduces the overall mass by 26% relative to the 3-stage equivalent, and additionally increases the acceleration capabilities of the gear train by 50%. The 4-stage transmission also increases

overall efficiency by 1%, which is obviously modest relative to the mass and acceleration advantages. Note that, since these gear trains are scaled by (12), the stress experienced by both gear trains is the same.

B.1.4 Discussion

It is common for designers to use the minimum feasible number of stages when designing a multistage gear train. The analysis presented here, however, indicates that adding an additional stage (or stages) may significantly improve the performance of a drive system. An analytical solution for the number of stages to use in a multistage transmission to minimize the reflected inertia of the gear train was provided by [110]. However, that solution did not provide topological context for the optima. As can be seen from Figure 3, the local curvature around the optimum is small, which implies that a designer may select a number of stages for the transmission in the neighborhood of the optima without a large compromise in drive system performance. For this reason, the shape of these objective functions should be examined with respect to n so that design tradeoffs (such as mechanical complexity and packaging) may be effectively balanced.

As can be seen from Figure 3, similar trends hold with respect to the number of stages used in a transmission, regardless of how the stage ratios were selected. As such, all criteria are substantially affected by selection of number of stages, and therefore a designer should carefully consider the number of stages in the design process. Choosing the minimum feasible number of stages for the transmission may not provide optimal system performance, as indicated by Figure 3. As per the example described by Figure 4, although a 3-stage transmission may be feasible, the 4-stage equivalent provides improvements in transmission

performance with respect to all three objective functions, regardless of which of the three selection criteria were used for selection of stage ratios.

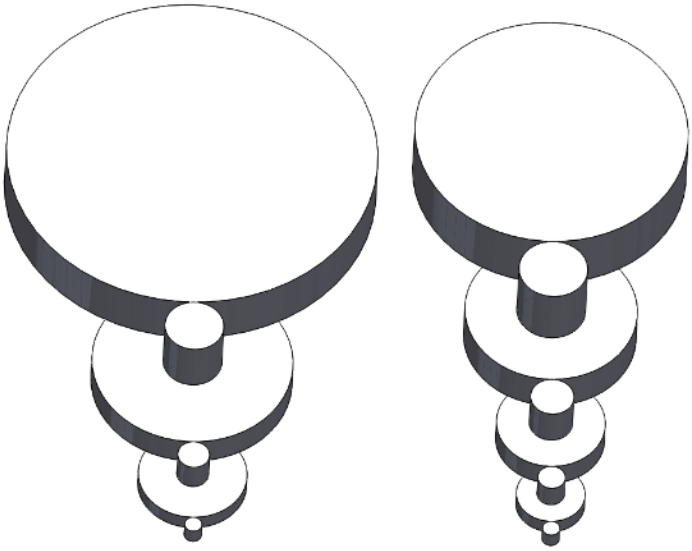

Figure 4: Physical depiction of a 3-stage (a) and a 4-stage (b) transmission with total ratios of 250:1 which maximize transmission efficiency. The 4-stage transmission has higher efficiency, higher normalized acceleration, and lower mass.

With respect to selecting the individual stage ratios of a gear train, Figure 3 also indicates that stage ratio selection has a more significant impact on efficiency, acceleration, and mass when the number of stages in the transmission is low. This can be seen by the divergence of the three curves in Figure 3a-c in the region of low number of stages. It is also interesting to note that the stage ratios show opposite trends when selected to minimize the mass of the transmission or to maximize the acceleration properties of a transmission, as shown in Figure 2. The divergence of optimal solutions highlights the value of considering the relative importance of minimal rotational inertia, versus minimum mass, when selecting the stage ratios for a given gear train and design application.

Considering multiple objective functions simultaneously, as is done in this work, allows a designer to assess which design objectives are sensitive to particular design

parameters. For example, Figure 3 shows that the selection of number of stages has a significant effect on the acceleration capabilities of the drive system, but has a relatively small effect on the overall efficiency of the transmission. If maximizing efficiency were the only objective function considered, a designer may have overlooked the possibility of designing a transmission with maximum acceleration (with almost no cost in efficiency).

It should be noted that this optimization does not consider some aspects of transmission design that may affect the objective functions considered. For example, the mass of the shafts and bearings necessary to construct a transmission have not been considered, and the efficiency losses associated with bearings are not considered. The formulation presented here also does not include the effects of speed (i.e., pitch-line velocity) on gear stress. The volumetric packaging of the optimization's resulting transmissions is also not considered, although this is expected to scale closely with transmission mass. Despite these limitations, the analyses presented here are believed to capture salient features of gear-based transmission design, and the formulation and implications of it should offer useful and accurate insights with respect to selecting the number of stages and stage ratios of gear trains for achieving desired performance characteristics.

B.1.5 Conclusion

This paper describes a formulation that provides the optimal stage ratios for a n-stage multistage gear train with a desired overall transmission ratio that maximizes efficiency, maximizes transmission acceleration, or minimizes transmission mass, respectively. In addition to providing a formulation from which a designer can obtain the optimal number of stages and stage ratios, the authors highlight several related implications regarding gear train

design, including the following two seemingly counterintuitive results. First, for a gear train that provides a given total gear reduction ratio, the respective objectives of minimizing rotational inertia (i.e., maximizing acceleration) and minimizing gear train mass are competing objectives with respect to selection of stage ratios. In particular, optimal stage ratio selection for a minimal rotational inertia solution entails successively increasing stage ratios, while optimal stage ratio selection a minimal mass solution entails successively decreasing stage ratios. Second, increasing the total number of stages can substantially decrease both mass and rotational inertia of a gear train. As such, substantially improved overall performance may be achieved by employing a number of stages that may be greater than the minimum feasible number of stages.

Appendix C

A Phase Variable Approach for IMU-Based Locomotion Activity Recognition

This work presents an algorithm for activity recognition using body-worn IMUs. This algorithm leverages the cyclic nature of locomotion as described in a phase variable context in order to identify the activity being performed by the user. This work was published as a journal article in the *IEEE Transactions on Biomedical Engineering* in September of 2017.

C.1 Manuscript C: A Phase Variable Approach for IMU-Based Locomotion Activity Recognition

C.1.1 Abstract

Objective: This paper describes a gait classification method which utilizes measured motion of the thigh segment provided by an inertial measurement unit (IMU). Methods: The classification method employs a phase-variable description of gait, and identifies a given activity based on the expected curvature characteristics of that activity over a gait cycle. The classification method was tested in experiments conducted with seven healthy subjects performing three different locomotor activities: level ground walking, stair descent, and stair ascent. Classification accuracy of the phase variable classification method was assessed for classifying each activity, and transitions between activities, and compared to a linear discriminant analysis (LDA) classifier as a benchmark. Results: For the subjects tested, the phase variable classification method outperformed LDA when using non-subject-specific training data, while the LDA outperformed the phase variable approach when using subject-

specific training. Conclusions: The proposed method may provide improved classification accuracy for gait classification applications trained with non-subject-specific data. Significance: This paper offers a new method of gait classification based on a phase variable description. The method is shown to provide improved classification accuracy relative to an LDA pattern recognition framework when trained with non-subject-specific data.

C.1.2 Introduction

Human movement typically entails a variety of periodic locomotion activities including walking, running, stair ascent, and stair descent. Recently, portable and/or wearable devices have started to emerge (e.g., smartphones, wrist monitors, etc.), which are able to monitor human movement and activity. Such monitoring has a number of potential applications, particularly with regard to healthcare. The monitoring of activities can include varying levels of precision. In the simplest form, monitoring may entail a recognition of movement, relative to absence of movement. Monitoring may further entail recognition of the number of steps during movement (e.g., similar to a common pedometer). In addition to number of steps, movement monitoring may provide recognition of activity type, such as walking, stair ascent, or stair descent. In this paper, such monitoring is referred to as activity monitoring (i.e., monitoring the number of steps associated respectively with a set of possible activities). Although various sensing technologies are available for such monitoring, such activity monitoring systems should ideally employ a minimum set of sensors. Due to the recent introduction of low-cost multi-axis MEMS-based inertial measurement units (IMUs), and to the relative ease with which they can be worn, MEMS IMUs are a particularly compelling sensing technology for such applications. As such, this paper offers a

methodology for activity monitoring of locomotion activities that incorporates measurements from a single leg-worn IMU.

Given the recent emergence of wearable sensors (e.g., wrist-worn sensors, smartphones, etc.) and the number of potential applications associated with activity monitoring, many researchers have begun developing activity monitoring algorithms. Reviews of various methodologies employed for activity monitoring using body-mounted sensors are given in [134-136]. The vast majority of methods described in these reviews, particularly for purposes of gait activity classification, employ pattern recognition approaches. Many variations of pattern recognition approaches exist, but nearly all employ a similar sequential computational taxonomy, which consists of first windowing sensor data; then extracting characteristic features from the windowed data; then potentially reducing the number of features using dimension reduction techniques; and finally employing a classification algorithm or approach to classify the data (in this case into a possible set of locomotion activities). As described in [137], some common features used in the feature extraction component include time-domain features (e.g., mean, median, variance, etc.), frequency-domain features (e.g., mean, median, or variance of frequency content from FFT), and wavelet-based features, which essentially provide an indication of frequency content changes over time. Although this paper does not focus on the relative utility of these feature types, a recent paper by [137] examining the relative accuracy of a gait activity classification approach using various feature types indicated that time and frequency-based feature types yielded higher classification accuracies than wavelet-type features. Regardless, following the feature selection and potential dimensional reduction components of the pattern recognition taxonomy, a classification algorithm is employed to classify activity based on

the (full or reduced) set of features. A large number of classification algorithms exist. A partial review of relevant algorithms is given in [134]. Among the classification algorithms recently used for gait activity classification include support vector machines [138-140], hidden Markov models [141], Gaussian mixture models [142, 143], linear discriminant analysis [10, 144], neural networks and decision tree [140], and logistic regression [145].

This paper presents a novel approach to gait activity classification that can be employed either as a complement to, or as an alternate to, the aforementioned pattern recognition approaches. Specifically, the method proposes a new feature set based on a phase-variable-based coordinate system. In the phase variable construct, the progression of a periodic activity is uniquely characterized by a single phase variable (or potentially by a set of phase variables) [146-148]. The phase variable construct has been recently employed in the context of human locomotion in several papers associated with the control of powered lower limb prostheses, including papers by [149-152]. Rather than employ a phase variable for purposes of prescribing a control behavior within a given locomotion activity (i.e., [17-20]), the authors present here a method that employs the notion of a phase variable as a basis to formulate a phase-variable-based set of features for purposes of gait activity identification. This phase-variable-based set of features could be employed in the feature extraction component of any common pattern recognition approach. Rather than do so in this paper, however, the authors examine the value of phase-variable-based features in a heuristic activity recognition algorithm. The method is described in the context of gait recognition (i.e., classification) of three activities: walking, stair ascent, and stair descent, and employs a single variable as input to the classifier. The sagittal plane motion of the thigh is utilized as the (single) input variable for the classifier, and is provided by a single (six-axis) IMU

worn on the thigh. Experimental assessments were performed with seven healthy subjects who performed multiple gait activities, including level walking at three speeds, stair ascent, and stair descent. Classification results were obtained with the proposed approach, and compared to results using a linear discriminant analysis (LDA) pattern recognition approach.

C.1.3 Algorithm Description

C.1.3.1 *Phase Space*

As previously mentioned, the method presented here is based on a phase variable (PV) representation, which requires that the variable input of interest be represented in a phase space (i.e., a signal as a function of its derivative). The methodology presented here further requires that the input variable form a simple closed curve in the phase space. Representation of a signal in a phase space (signal as a function of its derivative) as a simple closed curve requires that the signal be periodic and that each period be characterized by a single global maximum, a single global minimum, and no local extrema as a function of time.

The authors consider here the thigh angle with respect to the inertial reference frame (i.e., with respect to the vertical) in the sagittal plane as the input signal for activity classification. The thigh angle generally requires an integration of the corresponding phase in order to form a simple closed curve [152], and as such is represented here in the integral phase space (i.e., as the locus of points relating the angle to the time-integral of the angle). Specifically, the two dimensions (x and y) of the phase space used in this work are the thigh segment angle with respect to the gravity vector in the sagittal plane and the integral of a mean-subtracted version of this angle:

$$x(t) = \theta_T \qquad (1)$$

$$y(t) = \int_0^t \left[\theta_T - mean\left(\vec{\theta}_T\right)\right] dt$$

where θ_T is the thigh angle input. The bounds of the integral coincide with the beginning and end of a stride (i.e., the integral is reset each stride). The vector notation indicates a vector containing the time-history of a particular signal over the course of a stride (i.e., the mean subtraction of the integral occurs once per stride to allow for stride-to-stride consistency in the phase space). Note that this method of using a subtracted mean integral is the same as that originally proposed and implemented by [152].

Figure 1 shows the averaged thigh angle for seven healthy subjects for walking, stair ascent, and stair descent, plotted in the angle versus mean-subtracted integral phase space, as measured by a motion capture system. Note that, as required by the method, the locus of points for each activity forms a simple closed curve in this space for each limb segment input.

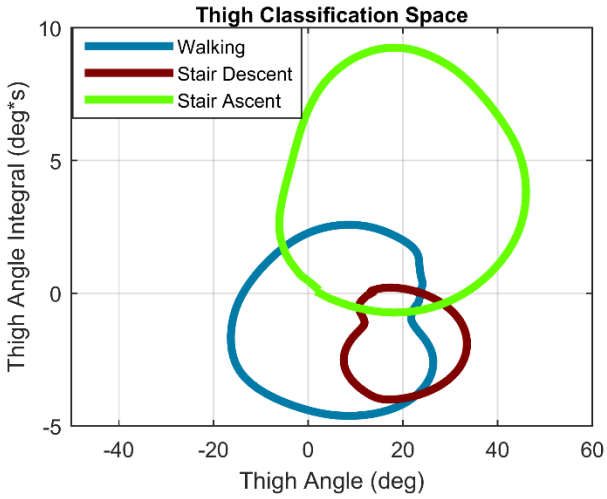

Figure 1: Phase space for the thigh. The phase space consists of the integral of the mean-subtracted thigh angle plotted against the thigh angle. Thigh angle is calculated relative to the gravity vector in the sagittal plane. Walking (blue), stair descent (red), and stair ascent (green) stride data for healthy subjects form simple closed curves in this space.

C.1.3.2 *Coordinate Frame Construction*

As seen in Fig. 1, the orbit of data for each activity is characterized by a unique shape, relative to the other activities. In order to distinguish each curve from the others, a separate activity-specific coordinate frame is constructed from the measured gait data associated with each activity (i.e., a data-driven coordinate frame). Each coordinate frame consists of two coordinates, here named "progression" and "magnitude," respectively. The progression coordinate is associated with the direction along the phase variable in that it indicates the progression through a given stride/period. The magnitude coordinate is the distance from the centroid of the coordinate frame (the origin). Specifically, each activity-specific coordinate frame is established by calculating the centroid of each respective closed activity curve, and using that centroid as the Cartesian origin of the coordinate frame. The centroid-centered curve is then scaled about the origin. This process creates a series of concentric paths (loops

of constant magnitude, m) centered about the origin. A series of rays (lines of constant progression, p) are then added which begin at the origin and pass through the reference data points in the phase space. This process creates a "spider web" type shape centered about the origin. It should be noted that reference data that is evenly spaced in time will result in a progression variable p which is also linearly spaced in time.

Figure 2 shows activity-based coordinate frames created for walking using the thigh angle input. These figures also have superimposed upon them the thigh data associated with walking, stair ascent, and stair descent. For each activity in each activity-specific coordinate frame, the progression and magnitude can be calculated quickly via a coordinate frame transformation, the specific details of which can be found in section C.1.8:

$$p = f(x, y) \qquad (2)$$

$$m = g(x, y)$$

where the progression of a given point is found by interpolating between the progression values associated with each ray in the coordinate frame (i.e., $p = 0$ for the start of a stride and 1 for the end of a stride) by using the angle between the point of interest and the horizontal. The magnitude of a point in the phase space is calculated in the activity-specific coordinate frame as the scalar by which one would need to multiply the original closed curve such that the new closed curve intersected the point of interest in the phase space. Both the progression and magnitude of points in the phase space can be calculated quickly within a given activity-specific coordinate frame.

Using an activity-specific coordinate frame, and given the definitions of progression and magnitude respectively, an instantaneous measure of similarity between an activity and

activity-specific coordinate frame can be formed by taking the partial derivative of the magnitude of an activity curve with respect to progression of the curve as follows:

$$D = \frac{\partial m}{\partial p} \qquad (3)$$

which is referred to here as the "divergence rate," and denoted by the symbol D. The divergence rate provides an instantaneous measure of how well the local curvature of an activity curve, as a function of progression, matches the activity of the coordinate frame on which it is evaluated.

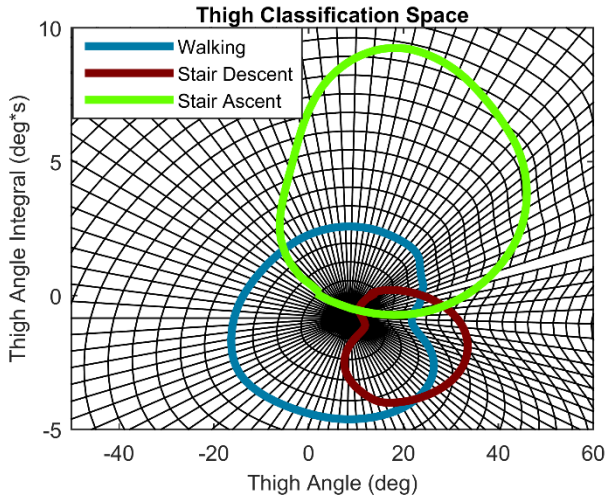

Figure 2: Custom coordinate frame constructed from a level-ground walking reference curve for the thigh. Walking (blue), stair descent (red), and stair ascent (green) stride data are plotted on this coordinate frame. Each concentric closed curve in the frame is a curve of constant magnitude (m) while each radial line is a line of constant progression (p).

In other words, the divergence rate indicates the extent to which the shape of a curve is aligned with the shape of a given activity-specific coordinate frame. An activity that

perfectly matches an activity-specific coordinate frame will have a divergence rate of zero (at all values of progression), regardless of magnitude. A small divergence rate indicates that data in the phase space is concentric with the closed loop used to generate the coordinate frame. Assuming invariance in the shape of an activity curve, as is generally the case in human locomotion, divergence can be used to indicate similarity of shapes shown in Figs. 1 and 2, and thus can be used to identify which activity is being performed. By examining Fig. 2, it can be seen that walking strides are expected to be fairly concentric with the paths of constant magnitude using the walking coordinate frame, yielding low divergence rate (D) values. However, the paths generated by healthy subjects when descending or ascending stairs are not concentric with the paths of constant magnitude in the walking coordinate frame, yielding much higher magnitudes of the divergence rate. This property can be leveraged to classify strides into various activities.

C.1.3.3 *Stride Classification*

Although Fig. 2 shows only the walking-specific coordinate frame, classification of activity entails constructing activity-specific coordinate frames for each activity, based on training data (i.e., averaged exemplar data). In this study three coordinate frames are constructed – one each for walking, stair descent, and stair ascent, respectively. The reference data used to construct these frames would presumably consist of an average of multiple strides from a single subject, or the average of multiple strides from multiple subjects. Subscripts are used to denote the coordinate frame, where w, d, and a are subscripts that represent the walking, stair descent, and stair ascent coordinate frames respectively.

An activity can be classified by computing the root mean square (RMS) of the

divergence rate for a given stride with respect to each activity-based coordinate frame to form a classification vector, $\vec{C}$. This vector, $\vec{C}$, provides a measure of RMS path divergence rate in each activity-based coordinate frame over the course of an entire stride, given by:

$$\vec{C} = \left[RMS(\vec{D}_w) \quad RMS(\vec{D}_d) \quad RMS(\vec{D}_a)\right] \qquad (4)$$

The elements of $\vec{C}$ provide a measure of similarity between the input data and the prototypical reference curve. The current activity can thus be classified as that corresponding to the smallest element of the classification vector.

C.1.3.4 *Confidence-Based Hysteretic Switching*

The proposed method can also provide a measure of the confidence of gait activity classification by examining the relative magnitudes of the entries in the classification vector, $\vec{C}$. A high degree of confidence is indicated when the magnitude of one entry is much lower than the other entries, while a low confidence is indicated when the entries of $\vec{C}$ are similar in magnitude. The average classifier confidence can be assessed while a user is performing a known activity by averaging the activity-normalized classification vectors across all strides in which the user is performing the known activity:

$$\bar{C}_n = mean(\frac{\vec{C}}{RMS(\vec{D}_n)}) \qquad (5)$$

where the mean is taken across all strides associated with activity *n*. A classifier confidence matrix, ε, can then be constructed by concatenating the mean classification vectors across

all activities into a single matrix (in this case of three activities, this matrix will be 3x3).

$$\varepsilon = \begin{bmatrix} \bar{C}_w \\ \bar{C}_d \\ \bar{C}_a \end{bmatrix} \tag{6}$$

To improve the classification accuracy, a state-machine can be implemented in which the classifier can classify the measured data as one of three states/activities. Each state/activity transitions to any other state/activity through a state transition (Fig. 3). The accuracy of the classifier can be improved by leveraging information from the confidence matrix, ε, in the design of the state transitions. Specifically, a state transition requirement can be constructed from the elements of ε and the measured data such that the classifier will switch from activity *i* to activity *j* if and only if the switching condition is satisfied (where the *i* and *j* numerical indices coincide with the numerical indices indicated for each activity in Fig 3):

$$switch \quad if \quad \left(T_{i\to j}\right) RMS\left(\vec{D}_j\right) < RMS(\vec{D}_i) \tag{7}$$

$$T_{i\to j} = S\varepsilon_{j,i}$$

where $T_{i\to j}$ is a switching threshold gain for the transition between activity *i* and activity *j*, S is a scalar switching sensitivity gain ($S = 0.02$ in this work), and $\varepsilon_{j,i}$ is the element in the j^{th} row and i^{th} column of the confidence matrix ε. The switching sensitivity gain used in this work was empirically tuned, as described in the following subsection of this paper. It should

be noted that $T_{i\to j} \neq T_{j\to i}$ which results in different switching conditions for each transition in the finite state machine. As such, the classifier is only allowed to switch states/activities if the RMS of the divergence rate for that stride becomes greater than S multiplied by the expected confidence associated with a new activity, when compared to the current activity. In order for the classifier to switch between activities, the classifier must have a sufficiently high level of confidence that the user is performing a different activity before switching to that activity. For example, in the case that a user is descending stairs, if training data suggests that $RMS(\vec{D}_w)$ is expected to be 10 times greater than $RMS(\vec{D}_d)$ ($\varepsilon_{2,1} = 10$), then the classifier will only switch from walking to stair descent if $RMS(\vec{D}_w)$ is at least 20% (i.e., 0.02*10) greater than $RMS(\vec{D}_d)$. In order to ensure that the algorithm cannot switch from the current state to more than one other state simultaneously, hysteretic switching is implemented as a two-step process: 1) identify the activity associated with the minimum entry in $\vec{C}$, and 2) if the state identified by step 1 is different than the current state, evaluate (7) to determine if a state transition should take place.

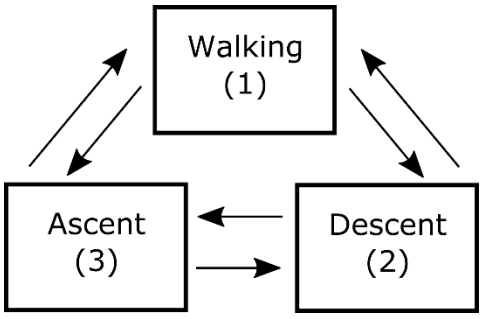

Figure 3: Activity classification state machine diagram in which each state/activity can transition to any other state/activity. Each state transition is governed by its own transition threshold as described by (7).

C.1.4 Implementation and Assessment

C.1.4.1 *Experimental Protocol*

To assess the efficacy of the previously described classification approach, the approach was implemented on data from seven healthy subjects (five men and two women) performing three locomotor activities – level ground walking (at three cadences), stair descent, and stair ascent. The test subjects ranged in age from 24 to 31 years old with an average age of 26.6 years. The study was performed with approval from the Vanderbilt University Internal Review Board (IRB). Each subject walked over level ground for 20 strides at three different cadences (enforced with a metronome): 85, 100, and 115 steps/min (walking speed was not controlled). The subjects also descended 20 stairs and ascended 20 stairs at a self-selected speed.

Thigh angular motion associated with each subject and each activity was measured using an IMU-based motion capture system (Xsens MVN). The motion capture data was utilized to provide global limb segment angles (angles with respect to the gravity vector) in the sagittal plane for the thigh segment, which was in turn used for the classification analysis previously described. All associated computation was implemented in MATLAB.

C.1.4.2 *Analysis*

The gait classification approach was assessed by using a leave-one-out cross validation in which data from six subjects was utilized to construct a reference curve ("training data"), and stride data from the seventh subject was classified using the proposed algorithm. This process was repeated such that each subject's data was classified using the remaining subjects' data to construct the reference curve. This cross-validation process

produced seven sets of classifier accuracy data which was averaged to assess the proposed method. This analysis represents an application scenario in which a single reference curve or training set may be applied universally to all users (not a subject-specific classifier).

To determine if the accuracy of the algorithm could be improved with subject-specific reference curves, each subject's strides were classified using the mean of their activity-specific gait data as the reference closed curve. The accuracy of the PV classifier was then assessed by calculating the percentage of accurately classified strides. Accuracy data was averaged across all of the subjects.

Although each element in the classification vector nominally corresponds to the RMS of the divergence rate over an entire stride, the classification vectors for the thigh input were calculated using only the final 75% (i.e., $0.25 \leq p \leq 1.0$) of the stride (i.e., the first 25% of each stride was excluded from consideration in all activities due to the relatively large inter-stride variability observed in the thigh input). If not excluded, the high variability in thigh motion specifically associated with the beginning of stair ascent would negatively affect classifier accuracy, which depends on gait consistency. Following computation of the respective classification vectors, the accuracy of the classifier was assessed by calculating the percentage of accurately classified strides for each individual gait activity. In each case, the stride was classified in the class corresponding to the smallest element in the classification vector. In all accuracy calculations, all walking data was considered regardless of cadence to determine if the approach is robust to variations in step frequency.

The accuracy of the PV classifier was compared to a conventional pattern recognition approach using a linear discriminant analysis (LDA) classifier. The LDA classification approach used two time-domain features to classify each stride: thigh segment angle mean

and standard deviation. Note that use of these features is recommended by [137], which indicates that these feature types tend to yield high classification accuracies for activity recognition.

A confidence matrix, ε, was created using the all of the data from the leave-one-out cross validation in which the reference curves were not subject-specific. The single confidence matrix was created by averaging the confidence matrix values from the analysis of each subject's data during the leave-one-out cross validation process. This confidence matrix was then utilized to implement the confidence-based switching state machine as described in (7). All strides were re-analyzed using this confidence-based switching in order to determine if this state machine approach could improve classifier accuracy.

If the switching sensitivity gain as described in (7) is too high, the classifier may be resistant to switching states in order to classify a new activity. If this gain is too low, the confidence-based switching will provide no additional benefit over the phase variable approach alone. The switching sensitivity gain was chosen by tuning the gain in order to maximize the classification accuracy on a single subject using subject-specific training data. This gain value was then used in all other applications of the hysteretic switching algorithm. To assess the activity switching aspect of the proposed algorithm, gait activity transitions were simulated by concatenating gait data from steady state activities into a single set of data. All six possible transitions between the three gait activities (see Fig. 3) were simulated in this way and the strides were classified by all three classification algorithms: linear discriminant analysis (LDA), the phase variable classifier (PV), and the phase variable classifier supplemented with the confidence-based switching (PV+CS). Gait transition data was classified using subject-specific training data and non-subject-specific training data via

the previously described method of leave-one-out cross validation.

C.1.5 Results

The average confidence matrix (6) calculated from the leave-one-out cross-validation of the experimental data, is given in Table 1. Recall that the confidence of classification is indicated by the relative magnitudes of the off-diagonal terms in the matrix, where higher off-diagonal numbers indicate a greater degree of confidence (larger expected difference in the entries of $\vec{C}$).

Table 1: Three by three confidence matrix associated with the leave-one-out cross validation. Each row of the confidence matrix was normalized to the entry associated with the activity being performed as noted in (5).

Thigh-Based Classification Confidence Matrix (ε)		Coordinate Frame Utilized		
		Walking	Descent	Ascent
Activity Performed	Walking ($\bar{C}_w$)	1	64	167
	Descent ($\bar{C}_d$)	13	1	77
	Ascent ($\bar{C}_a$)	126	133	1

The off-diagonal entries in Table 1 are utilized to determine the thresholds for state transitions in the confidence-based state machine (Fig. 3).

The PV classifier accuracy for the leave-one-out cross-validation is shown in Fig. 4, along with the accuracy resulting from the LDA classifier, and with the accuracy resulting from the phase variable approach with confidence-based switching (PV+CS classifier). The accuracy across all seven tested subjects were averaged to produce the bars (means) and error bars (plus and minus one standard deviation) in Fig. 4. The accuracy of the classifiers is segmented into respective accuracies when classifying each individual activity, then

averaged into classifier-specific accuracies to determine the average classifier accuracy.

As shown in the plot, the PV classification accuracies for each activity were 99.4±1.3%, 93.8±10.8%, and 100±0%, for level walking, stair descent, and stair ascent, respectively, which resulted in an average classification accuracy of 97.7±3.5%. For the LDA classifier, the classification accuracies for each activity were 99.1±2.1%, 96.4±9.4%, and 92.0±18.7%, for level walking, stair descent, and stair ascent, respectively, while the average classification accuracy was 95.8±6.8%.

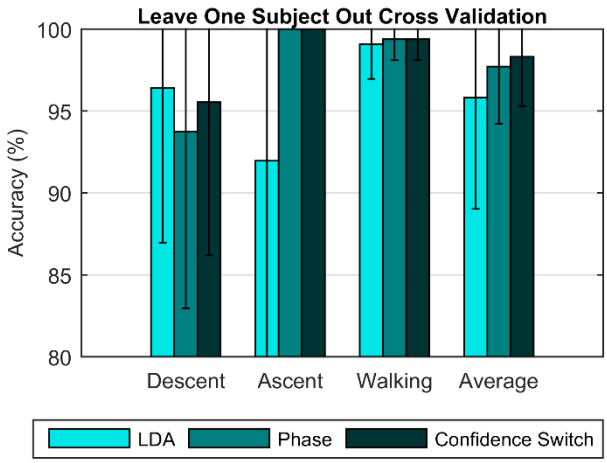

Figure 4: Classification accuracies from the non-subject-specific training represented by leave-one-out cross validation for the LDA classifier (light blue), phase variable classifier (medium blue), and the phase variable classifier with confidence-based switching (dark blue).

When the phase variable classifier was supplemented with confidence-based switching (PV+CS), the accuracies were 99.4±1.3%, 95.5±9.4%, and 100±0 %, for level walking, stair descent, and stair ascent, respectively, while the average classification accuracy was 98.3±3.0%.

The classifier accuracy was also examined using subject-specific reference curves ("training data"). Using subject-specific coordinate frames should account for gait patterns

that are unique to individual subjects, and thus should result in higher classification accuracy. The resulting subject-specific classifier accuracies, averaged across all seven subjects are given in Fig. 5. For the PV classifier, the average classification accuracies when using subject-specific frames were 99.8±0.4%, 96.4±4.9%, and 99.0±2.5%, for level walking, stair descent, and stair ascent, respectively, while the average classification accuracy was 98.4±1.6%. For the LDA classifier, the average classification accuracies when using subject-specific frames were 99.9±0.3%, 100±0%, and 100±0%, for level walking, stair descent, and stair ascent, respectively, while the average classification accuracy was 99.9±0.1%. When the phase variable classifier is supplemented with confidence-based switching (PV+CS), the accuracies were 99.9±0.3%, 98.2±3.0%, and 100±0%, for level walking, stair descent, and stair ascent, respectively, while the average classification accuracy was 99.4±1.1%. Thus, as expected, the accuracy of classification using subject-specific coordinate frames was notably improved relative to the non-subject-specific case (i.e., relative to Fig. 4).

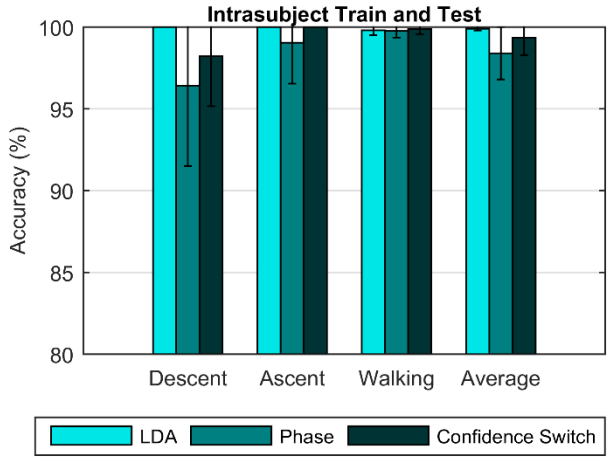

Figure 5: Classification accuracies from subject-specific training and testing for the LDA classifier (light blue), phase variable classifier (medium blue), and the phase variable classifier with confidence-based switching (dark blue).

The classifier accuracy was also examined on the concatenated gait data (represented

gait transitions) in which all six possible activity transitions were examined. This analysis was performed using non-subject-specific training data via a leave one out cross validation (Fig. 6) and with subject-specific training data (Fig. 7). The classifier accuracies for all the transitions were additionally averaged to more easily compare the classification algorithms.

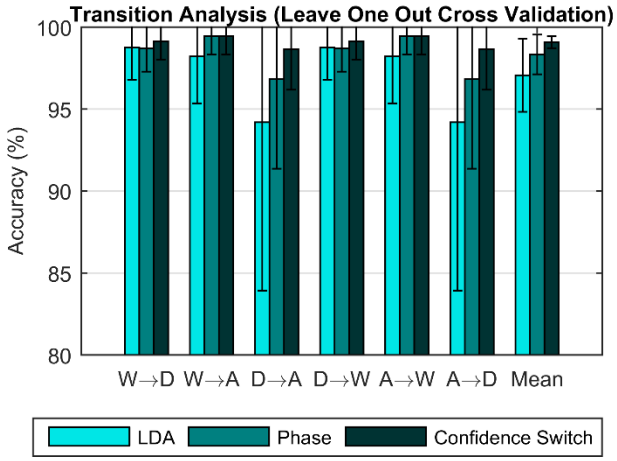

Figure 6: Classification accuracies for non-subject-specific training for transition gait data (leave one out cross validation) for the LDA classifier (light blue), phase variable classifier (medium blue), and the phase variable classifier with confidence-based switching (dark blue). Transitions from the first activity to the second activity are denoted by arrows where walking, stair descent, and stair ascent are abbreviated by W, D, and A, respectively.

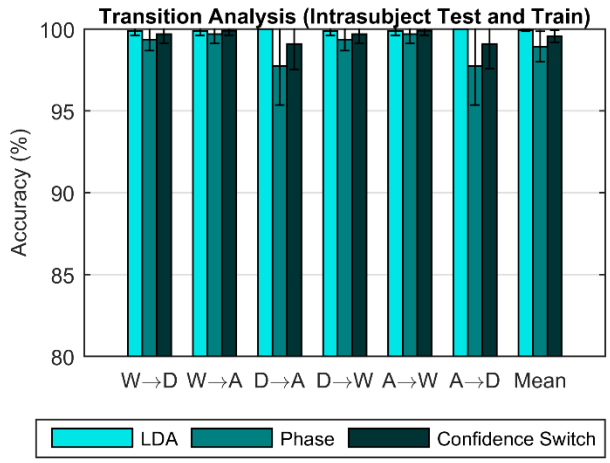

Figure 7: Classification accuracies for subject-specific training for transition gait data (intrasubject training and testing) for the LDA classifier (light blue), phase variable classifier (medium blue), and the phase variable classifier with confidence-based switching (dark blue). Transitions from the first activity to the second activity are denoted by arrows where walking, stair descent, and stair ascent are abbreviated by W, D, and A, respectively. The mean accuracies across all transition data is additionally presented in the far right set of bars.

C.1.6 Discussion

C.1.6.1 *Classifier Accuracy*

As can be seen from Figs. 4 and 6, the proposed PV classifier (both without and with the confidence-based switching) exhibits higher classification accuracies on average than the LDA classifier while also maintaining more consistent classification accuracies across subjects (i.e., lower standard deviation) when non-subject-specific training data is utilized. In the scenario depicted in Figs. 5 and 7, in which the training data was subject-specific, the LDA classifier outperformed the PV method. As indicated by Figs. 4-7, the addition of confidence-based switching (i.e., PV+CS approach) enhances the classification accuracies relative to the PV approach.

C.1.6.2 *Factors Affecting Algorithm Efficacy*

As is well known (and indicated in [83]), humans tend to adopt highly consistent movement during locomotion. Since the phase variable method classifies activity based on the nominal (i.e., mean) shape of movement, the method is particularly well-suited to applications that use non-subject-specific training. Note that using a mean-generated curve, as opposed to a distribution of points, also provides the beneficial characteristic that it avoids issues associated with overfitting, since the process of averaging by its nature precludes overfitting. An important requirement of this method, however, is that the input associated with different gait activities to be classified be characterized by a trajectory in the phase space that is qualitatively distinct (in shape and/or centroid) from that of other activities. This is in contrast with the LDA classification algorithm implemented in this study, which had no features that explicitly describe the shape of the trajectory traversed in the phase space. This lends insight into scenarios in which the LDA algorithm is expected to outperform the phase variable approach and vice versa. For example, consider the classification scenarios pictured in Fig. 8, in which two hypothetical activities have identical shapes and are centered about the same centroid (one activity is a scaled version of the other). For the PV approach, these two activities are indistinguishable from one another because the divergence rate of either activity, as calculated on the coordinate frame created by the other activity, will be close to zero. However, the standard deviation of the angle trajectory of the two activities will be different, allowing the LDA algorithm (that employs standard deviation as a feature) to distinguish between the two activities. The case pictured in Fig. 8b provides a counter example in which two hypothetical activities have similar means and standard deviations (in the segment angle dimension), but have different shapes in the phase space. The two

activities pictured in Fig. 8b would therefore be easily distinguishable with the PV algorithm, but not with a typical LDA classifier (particularly one that employs mean and standard deviation as features). As such, in order for the PV algorithm to effectively classify activities, the activities should exhibit different shapes in the phase space and/or be centered about different centroids.

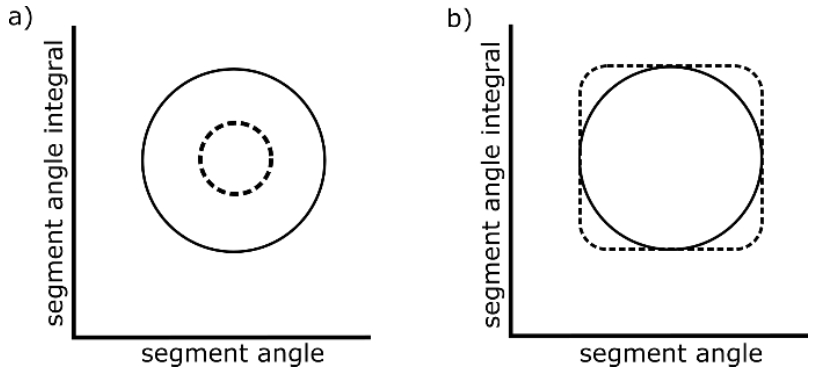

Figure 8: Example scenario in which two activities plotted in the phase space (solid line activity and dashed line activity) in which LDA should classify more accurately (a) and where the phase variable approach should perform more accurately (b).

C.1.6.3 *Real-Time Considerations and Possible Applications*

As described here, the PV algorithm computes the RMS divergence rate associated with an entire stride for purposes of classifying activity, primarily because equation (1) requires the mean of the stride's limb segment angle trajectory, which is only known at the end of a stride. This type of implementation is sufficient for activity monitoring algorithms in which classification can be recorded at the end of each stride. In applications requiring classification of an activity within the span of a stride (e.g., control of a microprocessor-controlled prosthesis), the approach as implemented here would not be suitable. The algorithm proposed here, however, could potentially be adapted to smaller time windows to provide intra-stride classification functionality by employing methods similar to those

described in [152].

C.1.6.4 *Divergence Rate as a Feature for Pattern Recognition*

Although presented here as a method to classify gait activities (i.e., using the vector of RMS divergence rates, and potentially supplemented with the confidence-matrix-based switching law), the divergence rate vector could separately be employed as a feature within a standard pattern recognition taxonomy. Specifically, in addition to time domain, frequency domain, or wavelet based features, a pattern recognition system could extract from the windowed data the classification vector ($\vec{C}$) as a feature, which could be used independently or in conjunction with other features as input to a classifier. Based on the study presented here, the classification vector provides an information-rich feature that encodes information about the centroid and shape of a trajectory in the phase space, which would presumably enhance the accuracy of a pattern recognition approach.

C.1.7 Conclusion

This paper describes a method for the classification of gait activities based on representing limb motion in a phase-space-based coordinate system. The classification method as examined here utilizes the measured movement of the thigh as input, and represents this movement on a set of phase-variable-based activity-specific coordinate frames to classify an activity type. The method in essence matches a phase space trajectory to the closest "activity template," where the activity template is obtained as the average movement associated with an activity in the phase space. The process of matching is based on calculation of the curvature of a trajectory within the phase space, where zero curvature

within the coordinate frame indicates a perfect match. The proposed approach was illustrated in the context of classification of three gait activities – level walking, stair descent, and stair ascent – using the thigh limb segment measured from a leg-worn IMU. The PV method outperformed an LDA classifier when used with non-subject-specific training data, while the LDA outperformed the PV when using subject-specific training data. As such, it appears that the PV method may be particularly well-suited to gait classification applications involving non-subject-specific training data.

C.1.8 Coordinate Transformation

The Cartesian dimensions of a point in the classification space, $\vec{a} = \left[a_x, a_y\right]^T$, can be converted to a progression (p) and magnitude value (m) through a coordinate transformation as described in (2) (Fig. 9). In order to define this coordinate transformation, a set of points in Cartesian space, $\vec{F} = [\vec{X}, \vec{Y}]$, must be chosen from which the coordinate frame is constructed. These points represent the reference curves utilized in the main body of the paper. The centroid of the reference curve is defined by the point $\vec{\beta} = [\beta_x, \beta_y]^T$ and is given by:

$$\vec{\beta} = [mean(\vec{X}), mean(\vec{Y})]^T \qquad (8)$$

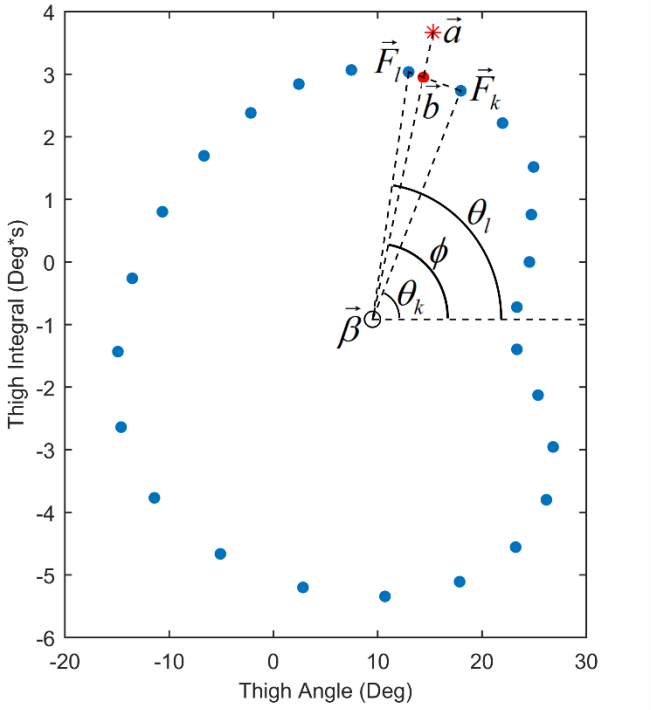

Figure 9: Coordinate transformation example with key variables shown for clarity. Blue points represent the points in $\vec{F}$. The centroid is labeled as $\vec{\beta}$ while the point being transformed is $\vec{a}$. The angle from the horizontal to key points are also labeled as φ, θ_k, and θ_l.The point $\vec{b}$ is also indicated.

Assuming that the entries in $\vec{F}$ are linearly spaced in time, a linearly space progression vector spanning the range of $p = 0$ to $p = 1$ is created that is the length of $\vec{F}$:

$$\vec{p}_q = \frac{q-1}{length(\vec{F})-1} \quad for \;\; q = 1 \;\; to \;\; q = length(\vec{F}) \qquad (9)$$

where q indicates the q^{th} element in $\vec{p}$. Additionally, an array of angles from the horizontal to each point in $\vec{F}$ can be found using:

$$\vec{\theta} = atan2(\vec{Y} - \beta_y, \vec{X} - \beta_x) \qquad (10)$$

where *atan2*() is the four-quadrant inverse tangent function. The angle from the horizontal to the test point can also be found using this four-quadrant inverse tangent function as follows:

$$\varphi = atan2(a_y - \beta_y, a_x - \beta_x) \qquad (11)$$

The angle φ is has the following bounds: ($\theta_k \leq \varphi \leq \theta_l$) where the angles θ_k and θ_l are defined by the angles from the horizontal to the points $\vec{F}_k$ and $\vec{F}_l$ where k is the k^{th} point and l is the l^{th} point in $\vec{F}$. The progression value of point $\vec{a}$ is found by interpolating φ between the progression values associated with the points $\vec{F}_k$ and $\vec{F}_l$ as follows:

$$p = p_k + (\varphi - \theta_k)\frac{p_l - p_k}{\theta_l - \theta_k} \qquad (12)$$

where p_k and p_l are the k^{th} and l^{th} entries in $\vec{p}$.

To calculate the magnitude of the point $\vec{a}$, the intersection of the line that passes through $\vec{a}$ and $\vec{\beta}$ and the line that passes through $\vec{F}_k$ and $\vec{F}_l$ must be found. This intersection point, $\vec{b}$ can be quickly found as follows:

$$A = \begin{bmatrix} \frac{Y_k - Y_l}{X_k - X_l} & -1 \\ \frac{\beta_y - a_y}{\beta_x - a_x} & -1 \end{bmatrix} \qquad (13)$$

$$B = \begin{bmatrix} \frac{Y_k - Y_l}{X_k - X_l} X_l - Y_l \\ \frac{\beta_y - a_y}{\beta_x - a_x} a_x - a_y \end{bmatrix}$$

$$\vec{b} = A^+ B$$

where the k or l subscript indicates the k^{th} or l^{th} element, respectively, of the vector indicated and where the + superscript indicates the Moore-Penrose pseudoinverse. The ratio of the distances from $\vec{\beta}$ to $\vec{b}$ and from $\vec{a}$ to $\vec{\beta}$ can then be taken in order to calculate the magnitude of point $\vec{a}$:

$$m = \frac{\left\| \vec{a} - \vec{\beta} \right\|}{\left\| \vec{b} - \vec{\beta} \right\|} \qquad (14)$$

Appendix D

A Stair Ascent and Descent Controller for a Powered Ankle Prosthesis

This work presents the design and assessment of a set of controllers for stair ascent and descent. A supervisory controller is also presented that allows for transitions between stair ascent, stair descent, walking, and standing. This work was performed by a visiting undergraduate student, Steven Culver, under my advisement. The work was published as a journal article in the *IEEE Transactions on Neural Systems and Rehabilitation Engineering* in May of 2018.

D.1 Manuscript D: A Stair Ascent and Descent Controller for a Powered Ankle Prosthesis

D.1.1 Abstract

This paper presents a control system for a powered transtibial prosthesis that provides stair ascent and descent capability, as well as an ability for user-controlled transitions between walking, standing, stair ascent, and stair descent. The control system was implemented on a powered prosthesis and evaluated on a single unilateral transtibial amputee subject. The ability of the prosthesis to provide appropriate functionality during stair ascent and descent was assessed by comparing gait kinematics and kinetics of the prosthesis to those of a passive dynamic elastic response (DER) prosthesis and those of a set of non-amputee subjects. Data from the assessment indicates that the powered prosthesis is able to provide some desirable stair ascent and stair descent characteristics, relative to the passive prosthesis.

D.1.2 Introduction

Stairs are commonplace in human-designed environments. Although non-amputee persons can easily ascend and descend stairs, stair ambulation can be demanding and potentially dangerous for individuals with lower-limb amputation. While there have been some substantial advances in the past decade in below-knee prosthetic technology, modern prosthetic ankle-foot complexes remain deficient with respect to their ability to fully replicate non-amputee human gait [62], particularly during stair ascent and descent. Among these deficiencies, non-amputee stair ascent requires net positive power delivery [153], which cannot be provided by energetically passive dynamic-elastic-response (DER) prosthetic feet [154, 155], leading to asymmetrical gait and necessitating compensatory actions of the hip and knee [156]. Similarly, non-amputee stair descent requires the ability of the ankle joint to appropriately configure itself prior to foot strike, and to dissipate substantial power during the loading phase [153]. Passive DER prosthetic feet are unable to actively reconfigure the ankle (i.e. actively plantarflex during swing), and as such stair descent with DER prostheses is characterized by heel strike rather than toe or forefoot strike [156]. Additionally, the spring-like nature of DER prostheses does not allow for the substantial power dissipation following foot strike that characterizes non-amputee stair descent.

Recent advances in prosthetic technology have introduced powered ankle-foot prostheses, which are potentially capable of better replicating non-amputee human biomechanics than corresponding passive prostheses. Multiple powered transtibial prostheses have been introduced in research literature over the last decade, such as those

described in [22, 23, 63, 157, 158]. Despite the emergence of these devices, little work has been published on control methods of stair ascent and descent for them (with the exception of [49, 66], to be discussed subsequently). In contrast, a number of control methods for stair ascent and descent for powered transfemoral prostheses have been described, both for purposes of controlling movement (e.g., [5-9]) and for purposes of recognition of intent to do so (e.g., [10-12]).

Among the notable differences between the transfemoral and transtibial cases, the latter generally have considerably fewer sensors, and thus must provide for control and intent recognition with different information, and typically a small subset of the information available in the transfemoral case. As previously mentioned, two papers that do describe methods of control for stair ascent and descent in a powered transtibial prosthesis are [49] and [66]. In both these works, which are both from the same research group, the prosthesis controller employs electromyogram (EMG) information from the residual limb. In the former work [49], the EMG was used primarily to recognize intent to switch between walking and stair descent, while in the latter [66], EMG was used to volitionally modulate powered plantarflexion in the prosthesis during ambulation.

In the work presented here, the authors present a control methodology that enables stair ascent and descent functionality with a powered transtibial prosthesis, and also present a corresponding methodology for volitionally switching between walking and stair functionality, based solely on two measurements – ankle angle (i.e., angle between foot and shank, as measured by an ankle encoder) and shank angle (i.e. angle of shank relative to the vertical, as measured by a 3-axis inertial measurement unit, or IMU. Specifically, the authors describe a stair ascent activity controller, a stair descent activity controller, and a supervisory

controller for facilitating user-controlled transitions between them and a (previously published) level-walking controller. Experimental results are presented on a subject with transtibial amputation, comparing stair ascent and descent characteristics with the powered prosthesis and associated controllers to performing the same activities with a daily-use DER passive prosthesis.

D.1.3 Control for Ascent and Descent

D.1.3.1 *Impedance-Based Control Design*

The control system for the ankle employs an overall control structure similar to one presented by the authors in a previous publication [64], although that paper presents a controller for standing and walking only. This paper adds stair ascent and stair descent controllers to that structure, in addition to a means for the user to switch between these four activity controllers (i.e. standing, walking, stair ascent, and stair descent). As in the previous work, each activity controller takes the form of a finite state machine (FSM), where the behavior within each state emulates a passive spring-damper system at the ankle with controller-selectable stiffness, equilibrium point, and damping coefficient, such that the ankle torque is given by:

$$\tau = k_i\left(\theta_a - \hat{\theta}_i\right) + b_i\dot{\theta}_a \qquad (1)$$

where τ, θ_a, and $\dot{\theta}_a$ denote ankle torque, ankle angular position, and ankle angular velocity of the prosthesis, and k_i, b_i, and $\hat{\theta}_i$ denote the stiffness, damping coefficient, and equilibrium angle for the i^{th} state of a given activity controller. Prospective benefits of the piecewise passive-impedance control framework are discussed in [159]. Note that all decisions in the standing, walking, stair ascent, and stair descent control structure are based strictly upon the

measured combination of the ankle angle θ_a (i.e., angle between foot and shank) and shank angle θ_s (i.e., sagittal-plane angle of shank relative to vertical, as measured by a 3-axis IMU).

D.1.3.2 *Stair Ascent Controller*

The stair ascent FSM, depicted in Fig. 1, consists of five states that are typically activated sequentially during a single stride of stair ascent. The five states, numbered sequentially from State 0 to 4, correspond respectively to foot strike, middle stance, push off, early swing, and late swing. The respective behaviors within each state and the corresponding transition condition to each successive state are described in the text below.

The supervisory controller enters the stair ascent controller in State 0, the foot strike state, which is indicated by ankle dorsiflexion, specifically a dorsiflexive angular velocity $\dot{\theta}_a$ greater than a threshold, and a dorsiflexive angle θ_a also greater than a threshold. Similar to heel strike during walking, this can be considered the start of the gait phase. The ankle behavior in this state is characterized by a relatively high stiffness and damping and an equilibrium angle of zero, which absorbs shock associated with foot strike. Following foot strike, the ankle transitions into State 1, the middle stance state, based on a positive shank angular velocity ($\dot{\theta}_s$). The middle stance state is characterized by a high stiffness, an equilibrium angle of zero, and high damping, which enables the prosthesis to support the user's weight in a high impedance state as the contralateral foot is swung upwards towards the next step. Following middle stance, the controller transitions into State 2, the push-off state. The timing of push-off is synchronized with stance knee extension (associated with lifting the user's center of mass upward to the next stair), which is inferred to occur when the ankle angle is dorsiflexed past a threshold and the shank angular velocity becomes

significantly negative (i.e., direction of shank rotation such that the knees moves posteriorly relative to the ankle). The push-off state is the main power delivery state and is characterized by a high stiffness with a plantarflexed equilibrium angle, and moderate damping. Push-off is assumed to have concluded when the ankle reaches the push-off equilibrium angle, which essentially indicates toe-off (i.e., the ankle is no longer loaded), at which point the controller transitions to early swing, which is characterized by a high stiffness, a slightly dorsiflexed equilibrium angle, and high damping, which allows the ankle to rapidly dorsiflex following push-off in order to clear the next step during the prosthesis swing phase. Following active swing-phase dorsiflexion, indicated when the ankle has reached the equilibrium angle and the ankle angular velocity is approximately zero, the controller transitions to State 4, late swing, which essentially holds the ankle in a neutral position. State 4 is characterized by similar impedance characteristics used in the landing state, but with a somewhat lower stiffness. Upon detection of foot strike, as previously discussed, the controller transitions to State 0 and repeats the stair ascent gait cycle. Note that the transition conditions corresponding to the stair ascent state controller (shown in Fig. 1) are summarized in Table I.

TABLE I
FINITE STATE TRANSITIONS FOR THE STAIR ASCENT CONTROLLER

Transition	Description	Condition
T_{A01}	Shank has positive angular velocity as the user extends leg and loads ankle.	$\dot{\theta}_s > 0$
T_{A12}	Ankle is loaded; shank rotates quickly as user steps upward.	$\theta_a > \theta_{a,th,12}$ $\dot{\theta}_s < \dot{\theta}_{s,th,12}$
T_{A23}	Ankle is significantly plantarflexed after push off.	$\theta_a < \theta_{a,th,23}$
T_{A34}	Ankle has returned to a neutral position and is static.	$\dot{\theta}_a \approx 0$ $t_{ST} > t_{th,34}$
T_{A40}	Dorsiflexion of ankle indicates toe has contacted next stair (toe strike).	$\dot{\theta}_a > \dot{\theta}_{a,th,40}$ $\theta_a > \theta_{a,th,40}$

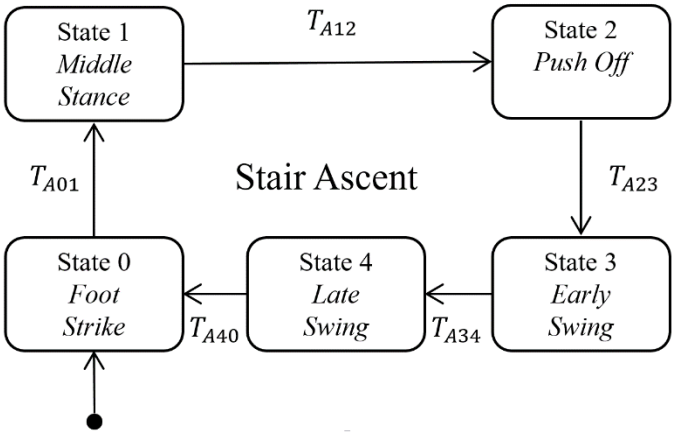

Fig. 1. Finite state machine executed by the prosthesis for stair ascent.

D.1.3.3 *Stair Descent Controller*

The stair descent FSM, depicted in Fig. 2, consists of two states, one that corresponds

to loading the prosthesis and one that corresponds to unloading. The two states are numbered 0 and 1, and correspond to stance and swing, respectively.

The prosthesis enters State 0, the stance state, with the ankle in a substantially plantarflexed position. The transition into State 0 corresponds to the toe strike event, detected by a substantial dorsiflexive ankle angular velocity. The ankle behavior in this state is characterized by low stiffness, an equilibrium angle towards plantarflexion, and high damping, the combination of which allows substantial power absorption via ankle dorsiflexion as the prosthesis is loaded, which assists in lowering the user down the stairs in a controlled fashion. In addition to the damping, the stiffness biases the ankle toward a substantially plantarflexive angle. As a result, when the prosthesis is unloaded following stance phase, the stiffness causes the ankle to plantarflex. The combination of ankle plantarflexion (detected by an ankle angular velocity towards plantarflexion) and a sufficiently negative foot angle ($\theta_f = \theta_s - \theta_a$), which corresponds to the plantar portion of the foot facing posteriorly, indicates unloading of the prosthesis and the initiation of swing phase, which switches the FSM into State 1, the swing state, which is characterized by a low stiffness and a plantarflexed equilibrium position, and employs a damping constant that ramps initially from a relatively low value, to a high value as the angular position of the ankle moves more towards plantarflexion, and a stiffness that similarly ramps slightly downward. This position-dependent change in impedance allows the unloaded prosthesis to initially quickly plantarflex, then transition to a soft stop as the prosthesis approaches the desired ankle angle. Upon toe-strike, the descent controller transitions back to State 0 (stance) based on the previously described detection of the toe-strike event. Note that the transition from State 1 to 0 also includes a minimum duration requirement to avoid false

detection of ankle dorsiflexion velocity resulting from potential oscillation during swing phase. A summary description of state transition conditions used in the stair descent controller are listed in Table II.

TABLE II
FINITE STATE TRANSITIONS FOR THE STAIR DESCENT CONTROLLER

Transition	Description	Condition
T_{D01}	Ankle is unloaded; shank is rotated to point foot downward.	$\dot{\theta}_a < \dot{\theta}_{a,th,01}$ $\theta_f < \theta_{f,th,01}$
T_{D10}	Foot has made contact with next stair; ankle dorsiflexes.	$\dot{\theta}_a > \dot{\theta}_{a,th,10}$ $t_{ST} > t_{th,10}$

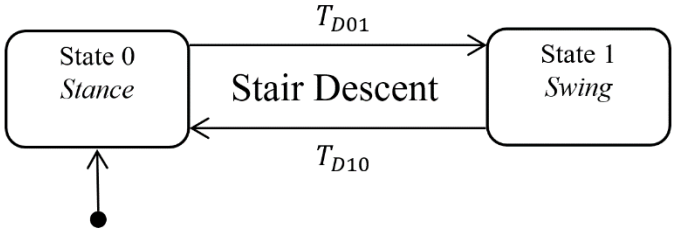

Fig. 2. Finite state machine executed by the prosthesis for stair descent.

D.1.3.4 *Walking and Standing Controllers*

The full suite of ankle controllers includes terrain-adaptive standing and variable-cadence walking controllers in addition to the previously-described stair ascent and descent controllers. The standing and walking controllers were adapted from prior work, and are described and diagrammed in [64], but for completeness are described briefly here. The walking controller consists of four states: State 3, which corresponds to late swing and early stance (i.e., heel strike); State 0, which corresponds to middle stance; State 1, which

corresponds to late stance (i.e., push off); and State 2, which corresponds to early swing. The standing controller consists of two states: State 0, which provides ground-adaptive supportive stiffness during weight bearing; and State 1, which provides conformal damping that enables adaptation to ground slope during non-weight-bearing (i.e., specifically when transitioning between the non-weight-bearing and weight-bearing states). As in the stair ascent and descent controllers, the ankle behavior within each finite state in the walking and standing controllers is given by (1).

D.1.3.5 *Supervisory Controller*

The supervisory controller FSM, depicted in Fig. 3, enables the user to switch between the standing, walking, stair ascent, and stair descent activity controllers. As shown in the figure, all controllers transition through the standing controller. From State 1 (i.e., non-weight-bearing) of the standing controller, the controller switches to stair ascent upon a toe strike (and subsequent dorsiflexion); switches to walking upon a heel strike (and subsequent plantarflexion); and switches to stair descent based on a holding the shank in a posteriorly-rotated position for a brief period of time (as subsequently described). All controllers return to State 0 of the stance controller by remaining in a mid-stance state, in the absence of shank motion, for a brief period of time.

More specifically, the controller switches from State 1 of the standing controller into State 0 of the stair ascent controller upon a forefoot strike, which is indicated by a dorsiflexive angular velocity and a dorsiflexed angular position greater than a threshold angle. Note that this is the same transition employed within the stair ascent controller to transition from late swing to landing (i.e., State 4 to State 0). The stair ascent controller

switches back to standing when the user maintains stance for a brief period of time in the absence of shank motion; specifically the stair controller can switch out of stair ascent in either of States 4, 0, or 1, when the ankle torque (τ_a) remains below a threshold for a sufficient period of time, indicating that the user is not continuing the stair ascent gait cycle.

The standing controller transitions from State 1 of the standing controller to State 3 of the walking controller at heel strike, indicated by a plantarflexive angular velocity and a plantarflexed angular position past a threshold angle. The transition back to State 0 of standing controller occurs from States 3 or 0 of the walking controller (i.e., early or middle stance) when the ankle and shank angular velocities are approximately zero for a sufficient length of time, indicating that the user is not continuing the walking gait cycle.

The standing controller transitions from State 1 of the standing controller to State 1 of the stair descent controller when the user holds the prosthesis such that the shank angular position exceeds a threshold and the shank angular velocity is approximately zero. This condition corresponds to a body posture similar to mid-swing on the prosthesis-side, although rather than swinging, the leg posture is held static for a short duration. The switch into stair descent is indicated by the ankle plantarflexion associated with stair descent State 1. The stair descent controller switches from State 0 of stair descent to State 0 of the standing controller when the user pauses in stance, as indicated when ankle and shank angular velocities are approximately zero for a sufficient period of time, indicating that the user is not continuing the stair descent gait cycle. Summary descriptions of each transition condition of the supervisory controller are listed in Table III.

TABLE III
FINITE STATE TRANSITIONS FOR THE SUPERVISORY CONTROLLER

Transition	Description	Condition
T_{SA}	Dorsiflexion of ankle indicates toe has contacted first stair.	$\dot{\theta}_a > \dot{\theta}_{a,th,SA}$ $\theta_a > \theta_{a,th,SA}$
T_{AS}	Controller is in late swing, landing, or stance state. Foot is in contact with ground. Torque is low and static for a sufficient length of time.	state $\in \{0,3,4\}$ $\tau_a < \tau_{th,AS}$ $t_{ST} > t_{th,AS}$
T_{SW}	Forward extension of shank and plantarflexion of ankle indicates heel strike of first step forward.	$\theta_s > \theta_{s,th,SW}$ $\dot{\theta}_a < \dot{\theta}_{a,th,SW}$ $\theta_a < \theta_{a,th,SW}$
T_{WS}	Controller is in early- or mid-stance state; ankle and shank are static for a sufficient length of time.	state $\in \{0,3\}$ $\dot{\theta}_s \approx 0$ $\dot{\theta}_a \approx 0$ $t_{ST} > t_{th,WS}$
T_{SD}	Volitional cue: user lifts foot and bends knee, statically aligning ankle with contralateral shank.	$\theta_s < \theta_{s,th,SD}$ $\dot{\theta}_s \approx 0$ $t_{ST} > t_{th,SD}$
T_{DS}	Controller is in stance state. Ankle is loaded. Ankle and shank are static for a sufficient length of time.	state = 0 $\dot{\theta}_s \approx 0$ $\dot{\theta}_a \approx 0$ $t_{ST} > t_{th,DS}$

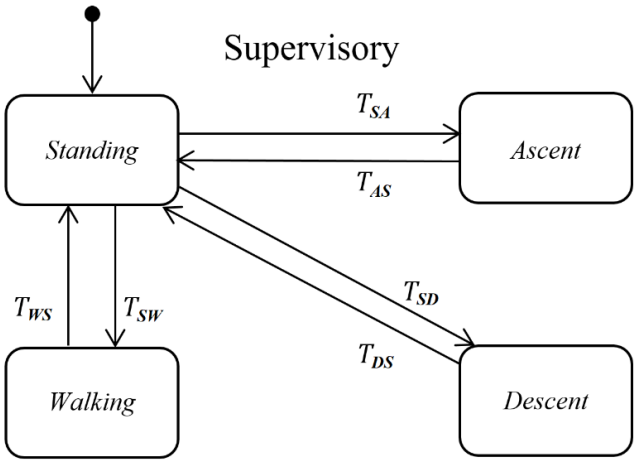

Fig. 3. Finite state machine executed by the prosthesis for transitions between standing, walking, stair ascent, and stair descent controllers.

D.1.4 Experimental Implementation and Assessment

D.1.4.1 *Prosthesis Prototype*

The previously-described control structure was implemented in a powered transtibial prosthesis prototype and its ability to provide appropriate functionality assessed on a subject with transtibial amputation. The prosthesis prototype, shown in Fig. 4, is similar to the transtibial prosthesis described in [64], although since that publication has been revised to include an integrated embedded system and battery. A brief description of functionality is described here, with more information given in [64]. The prosthesis has a range of motion of 45 deg of plantarflexion to 25 deg of dorsiflexion. Ankle torque is provided by a Maxon EC60 14-pole brushless motor that drives the ankle joint through a 116:1 three-stage belt/chain/chain transmission. A carbon fiber parallel spring engages at an approximately neutral ankle position (i.e., $\theta_a \approx 0\, deg$) and provides approximately 4.7 N-m/deg of unidirectional stiffness towards plantarflexion to assist with push-off torque production. The powered drive system is capable of providing peak torques of approximately 100 Nm, while the parallel spring provides an additional approximately 50 Nm in the range of dorsiflexion typically associated with push-off, such that combined torque is approximately 150 Nm.

Prosthesis sensing includes an absolute encoder at the ankle joint, an incremental encoder on the motor, and a 6-axis IMU on the embedded system. As previously indicated, these sensors are fused to provide real-time measurement of ankle angle and shank angle. Current sensing, in combination with a model of transmission dynamics (as discussed in [64]) provides an estimate of motor torque, which together with ankle and shank angle, are

the exclusive set of measurements employed in the full control system.

A custom embedded system mounted on the posterior aspect of the prosthesis prototype (see Fig. 4) includes: 1) a custom four-quadrant brushless motor servoamplifier; 2) a 16-bit digital signal processing chip (dsPIC33) that provides control of the brushless motor servoamplifier and sensor measurement and signal conditioning; 3) a 32-bit microcontroller (PIC32) that provides impedance-level control of the ankle joint, and communicates with a laptop supervisory controller via a CAN bus for controller prototyping. Specifically, for the work presented here, the prosthesis was tethered to a laptop computer running Simulink Real-Time Workshop through a CAN bus. The prosthesis sent sensor information to the Simulink controller, which determined the appropriate controller state and returned the corresponding set of impedance parameters to the PIC32, which employed the embedded system control structure to emulate the appropriate impedance on the prosthesis.

The prosthesis was powered by an on-board six-cell 24-volt lithium-polymer battery pack. The mass of the prosthesis as shown in Fig. 4 is 2.67 kg, excluding the mass of the battery-pack and shoe. The battery pack and associated housing together (see Fig. 5) have a mass of approximately 320 g, such that the total prosthesis mass with battery is approximately 3 kg.

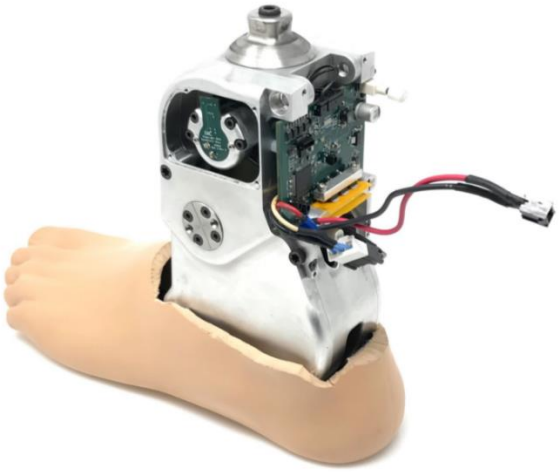

Fig. 4. Vanderbilt transtibial prosthesis prototype.

Fig. 5. Vanderbilt transtibial prosthesis prototype during stair ascent and descent, including integrated battery pack, and also showing CAN cable for supervisory control and data acquisition.

D.1.4.2 *Single-Subject Experiments*

The extent to which the proposed controller provides appropriate gait characteristics during stair ascent and descent was investigated in experiments on a single subject with transtibial amputation. The experiments specifically evaluated movement kinetics and kinematics provided by the powered prosthesis and controller during stair ascent and descent, relative to the same activities with the subject's daily use prosthesis, and relative to that of non-amputee subjects. The transtibial amputee subject was a 50-year-old male with a body

mass of 80.7 kg. The subject's passive daily-use prosthesis was a Fillauer AllPro. Approval to perform these assessments was granted by the Vanderbilt Institutional Review Board, and informed consent was obtained for the subject prior to the assessments.

The experimental implementation proceeded in two phases: the first was a controller tuning and subject acclimation phase, and the second was an experimental evaluation phase. During the controller tuning phase, control parameters for the level ground walking, standing, stair ascent, and stair descent controllers were experimentally tuned. A nominal set of controller parameters for impedance and transition conditions were adapted from [64] for standing and walking, and were established based upon values of ankle, shank, and foot angular position, angular velocity, and torque from non-amputee subject data for stair ascent and descent from [67, 83]. These parameters were tuned iteratively first on non-amputee subjects using able-bodied adaptors to provide comfortable and effective ascent and descent functionality, and subsequently tuned on the amputee subject to provide the same. A listing of all controller parameters for the full controller is given in Tables IV (impedance parameters) and V (transition conditions). Following controller tuning, the subject was allowed to acclimate to the powered prosthesis controller over a period of several hours on multiple days, until the subject felt comfortable with the prosthesis behavior and functionality in each activity mode.

The experimental evaluation phase consisted of three separate experiments, each conducted on a separate day. The first assessed ankle torque and motion for the powered and passive ankles during stair ascent and descent; the second measured the ground reaction force during stair descent for both types of prostheses; and the third involved repeated completion of a walking circuit involving walking, ascent, and descent while using the powered

prosthesis, in order to assess efficacy of the supervisory controller.

In the first experiment, the subject ascended and descended an eight-step staircase at a self-selected speed for each prosthesis type (powered and passive), while data were recorded throughout the eight step ascent and descent process. Images corresponding to the ascent and descent portions of this experiment conducted with the powered prosthesis are shown in Fig. 5, and a video showing ascent and descent of the stairs with both prosthesis types is provided in the supplemental material. Although data were collected during the entire ascent and descent processes, data were only analyzed for the second and third strides on the staircase for each activity, which follows the analysis protocol employed in [67]. A total of 14 trials were recorded for each of ascent and descent, where each trial consisted of two strides (i.e., for a total of 28 strides analyzed for ascent and 28 for descent). The passive and powered prosthesis data were all recorded in a single session, where all trials were completed with the passive prosthesis first, followed by all trials with the powered prosthesis. The authors assumed that any effects of fatigue would distort data corresponding to the powered prosthesis more severely than it would the passive device.

Ankle angle data for both prostheses were recorded via a 10-camera motion capture system (Vicon T40), employed with a lower body skeletal marker set consisting of thirty-eight reflective 15 mm markers. Motion capture data were sampled at 200 Hz using Vicon Nexus software, and data subsequently processed using C-Motion Visual3D and MATLAB to extract sagittal plane ankle joint motion. Strides corresponding to both stair ascent and descent were parsed and normalized to a time base of 100%, where strides begin and end at initial ground contact of the foot.

Ankle torque was recorded using different methods for the powered and passive

prostheses. Since the passive prosthesis is well-approximated as a stiffness, the stiffness of the daily-use passive prosthesis was characterized during level walking using the previously-described camera system, a set of AMTI OPT400600 force plates, and Visual 3D software, followed by post-processing in MATLAB (details provided in [160]). The resulting characterization of stiffness, combined with the measured ankle deflection, provided an estimate of the ankle torque provided by the passive prosthesis. Ankle torque for the powered prosthesis was calculated from the measured motor current, in combination with a model of the transmission system described in [64].

In a second set of experiments, the subject descended stairs onto a set of force plates (AMTI OPT400600). The subject performed this task 16 times for each prosthesis, and for each foot (i.e., descended onto the force plates with both the prosthesis side and sound side). As in the first set of experiments, these were conducted in one session, completing all trials with the passive prosthesis first, followed by all trials with the powered prosthesis.

For the third experiment, which evaluated the efficacy of the supervisory controller, the subject was instructed to navigate a self-paced ambulatory circuit that included four sections requiring the use of three ambulatory activity controllers (level walking, stair ascent, level walking, and stair descent). To navigate the circuit, the subject was placed in control of the prosthesis and was able to switch between activity mode controllers using the methods previously described. The circuit was navigated both clockwise (supervisory controller modes: standing, ascent, standing, walking, standing, descent, standing, walking, standing) and counterclockwise (supervisory controller modes: standing, walking, standing, ascent, standing, walking, standing, descent, standing). The circuit was traversed 15 times consecutively while the activity controller data was recorded. Note that a video showing the

subject completing the ambulatory circuit is included in the supplemental material.

TABLE IV
IMPEDANCE PARAMETERS FOR ACTIVITY MODE CONTROLLERS

Controller	State	$k\left(\frac{Nm}{\text{deg}}\right)$	$b\left(\frac{Nm \cdot s}{deg}\right)$	θ(deg)
Stair Ascent	Foot Strike	4	0.4	0
	Mid Stance	6	0.5	0
	Push Off	7	0.2	-20
	Early Swing	7	0.6	5
	Late Swing	3	0.3	5
Stair Descent	Stance	0.4	0.7	-25
	Swing	1 - 0.6	0 - 0.5	-20
Level Ground Walking	Late Swing	1	0.3	2
	Mid Stance	5	0.5	-4
	Late Stance	8	0.2	-20
	Early Swing	7	0.8	2
Standing	Stance	5	0.5	0
	Swing	1	0.3	0

TABLE V
FINITE STATE TRANSITIONS FOR ACTIVITY MODE CONTROLLERS

Contr.	Trans.	Condition
Stair Ascent	T_{A01}	n/a
	T_{A12}	$\theta_{a,th,12} = 4$ deg, $\dot{\theta}_{s,th,12} = -20$ deg/s
	T_{A23}	$\theta_{th,23} = -16$ deg
	T_{A34}	$t_{th,34} = 0.5$ s
	T_{A40}	$\dot{\theta}_{a,th,40} = 5$ deg/s, $\theta_{a,th,40} = 6$ deg
Stair Desce	T_{D01}	$\dot{\theta}_{a,th,01} = -5$ deg/s, $\theta_{f,th,01} = -2$ deg
	T_{D10}	$\dot{\theta}_{a,th,10} = 15$ deg/s, $t_{th,10} = 0.5$ s
Supervisory	T_{SA}	$\dot{\theta}_{a,th,SA} = 5$ deg/s, $\theta_{a,th,SA} = 6$ deg
	T_{AS}	$\tau_{th,AS} = 20$ Nm, $t_{th,AS} = 0.5$ s
	T_{SW}	$\theta_{s,th,SW} = 5$ deg, $\dot{\theta}_{a,th,SW} = -5$ deg/s, $\theta_{a,th,SW} = -1$ deg
	T_{WS}	$t_{th,WS} = 0.75$ s
	T_{SD}	$\theta_{s,th,SD} = -12$ deg, $t_{th,SD} = 0.5$ s
	T_{DS}	$t_{th,DS} = 1.0$ s

D.1.5 Results

D.1.5.1 *Stair Ascent Data*

Figure 6 shows results of the stair ascent experiment, and specifically shows the averaged ankle joint angle, torque, and power versus percent stride for stair ascent for the two experimental cases previously described. Each plot is the average of 28 strides of data for each prosthesis. Power was computed in MATLAB as the product of the ankle velocity and the phase-matched torque. The prosthesis data is also shown with averaged data from non-amputee-subject stair ascent, as reported by [67].

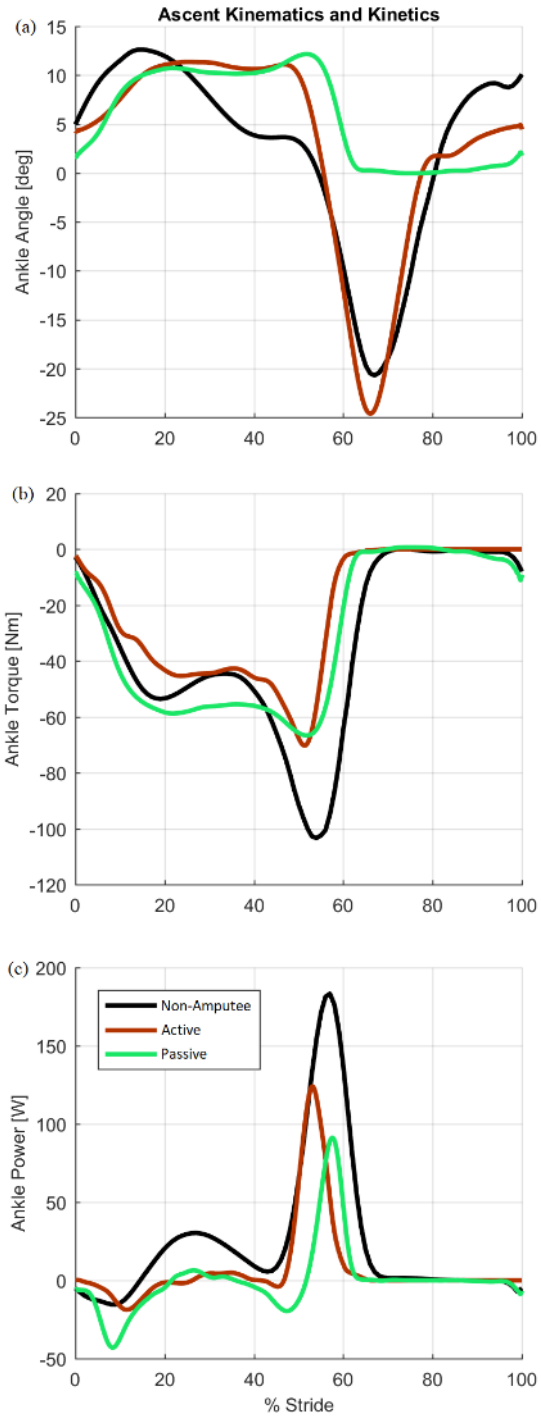

Fig. 6. Kinematics and kinetics comparison for the ankle joint in stair ascent, showing (a) ankle angle, (b) ankle torque, and (c) ankle power. The three lines on each plot indicate average ankle joint kinematics or kinetics for non-amputee subjects (non-amputee) and the experimental results for the amputee subject using the powered prosthesis (active) and the subject's daily use prosthesis (passive).

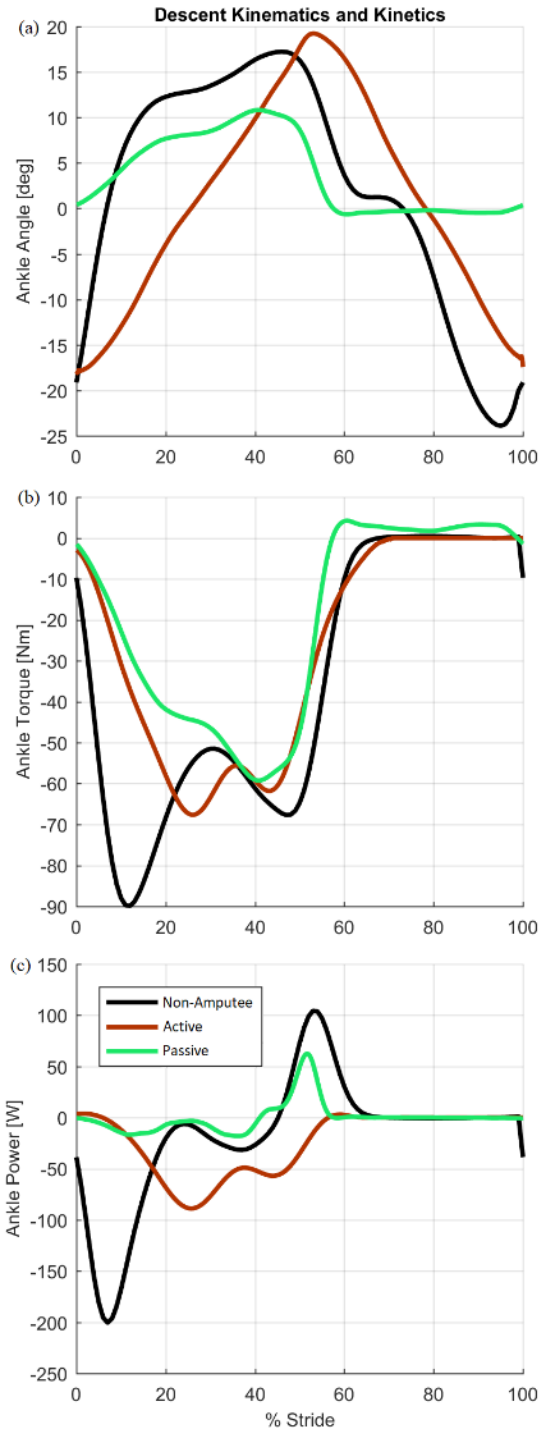

Fig. 7. Kinematics and kinetics comparison for the ankle joint in stair descent, showing (a) ankle angle, (b) ankle torque, and (c) ankle power. The three lines on each plot indicate average ankle joint kinematics or kinetics for non-amputee subjects (non-amputee) and the experimental results for the amputee subject using the powered prosthesis (active) and the subject's daily use prosthesis (passive).

D.1.5.2 *Stair Descent Data*

Figure 7 shows the results of the stair descent experiment, specifically the averaged ankle angle, torque, and power as a function of stride for each prosthesis (where each is the average of 28 strides), along with averaged data for non-amputee subjects from [67] [24]. Figure 8 shows the results of the second stair descent experiment (i.e., stepping onto the force plates) showing the average ground reaction forces during stair descent for each foot and each type of prosthesis. Specifically, Fig. 8a shows the ground reaction force when the subject's prosthesis side makes contact with the next stair (i.e., lowering by the sound side), while Fig. 8b shows the ground reaction force when the subject's sound side makes contact with the next stair (i.e., lowering by the prosthesis). From Fig. 8a, the passive prosthesis reaches peak loading of 790 N at 0.30 seconds and has an average stride time of 0.99 seconds, while the powered prosthesis reaches peak loading of 800 N at 0.66 seconds and has an average stride time of 1.43 seconds. From Fig. 8b, the passive prosthesis reaches a peak loading of 1346 N and has an average stride time of 1.06 seconds, while the powered prosthesis reaches a peak loading of 1125 N and has an average stride time of 1.60 seconds.

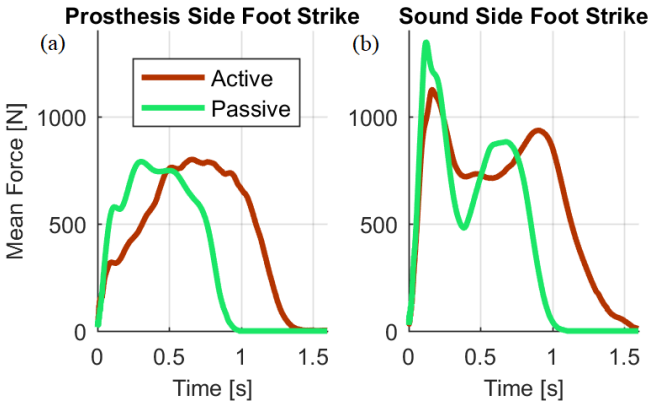

Fig. 8. Ground reaction forces for (a) prosthesis side, subject lowering bodyweight with sound side, and (b) sound side, subject lowering bodyweight with prosthesis side.

D.1.5.3 *Supervisory*

Figures 9 and 10 show results corresponding to the third experiment (i.e., the ambulatory circuit conducted with the powered prosthesis). Specifically, Fig. 9 shows the results of one clockwise user-controlled circuit and contains two plots: Fig. 9a shows the activity mode controllers during circuit testing (0 = standing, 1 = stair ascent, 2 = level walking, 3 = stair descent), while Fig. 9b shows the ankle joint angle versus time of the powered prosthesis. Figure 10 shows the results of 15 consecutive circuits (10 clockwise, 5 counterclockwise). The plots show activity mode versus time for each consecutive circuit trial.

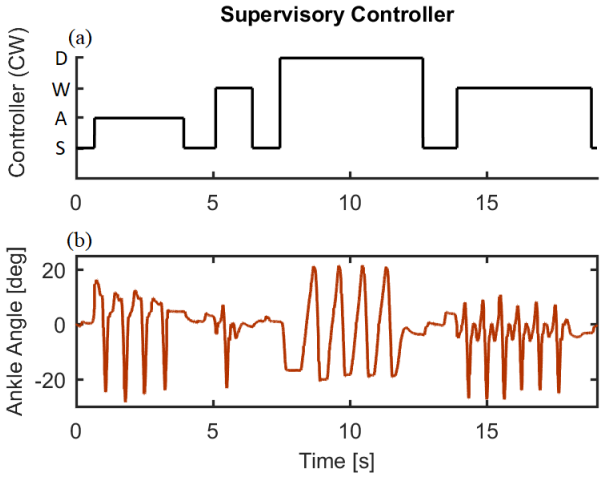

Fig. 9. Results of single clockwise circuit trial. Plot (a) indicates which activity mode controller the user has selected (S = standing, A = stair ascent, W = level walking, D = stair descent). Plot (b) indicates ankle angle for comparison with previous plots of ankle angle during stair ascent and stair descent. User must come to standing in order to switch between activity mode controllers.

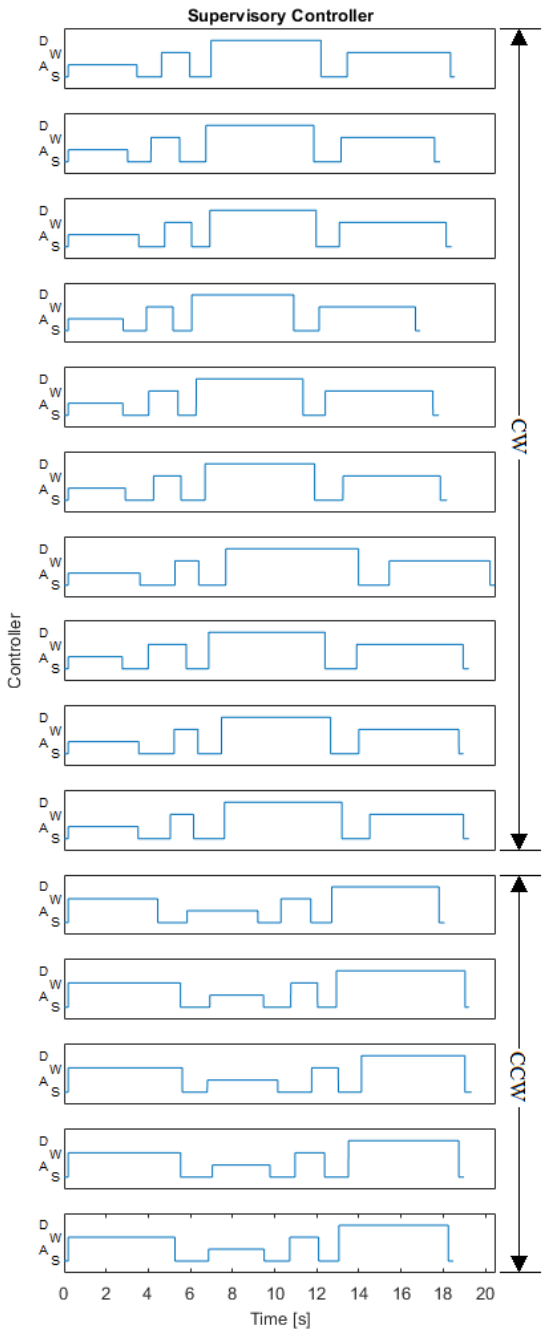

Fig. 10. Results of 15 consecutive circuit trails, both clockwise and counter clockwise. Y-axis indicates which activity mode controller the user has selected (S = standing, A = stair ascent, W = level walking, D = stair descent).

D.1.6 Discussion

D.1.6.1 *Stair Ascent Controller*

As depicted in Fig. 6a, the ankle angle of the powered prosthesis behaves similarly to the passive prosthesis during the stance phase, but clearly behaves as the non-amputee ankle during late stance for the push-off event. As depicted in Fig. 6b, the ankle torque is fairly similar in all three cases, although the powered prosthesis is somewhat more torque-limited (due to hardware limitations) relative to the other two cases. Integrating the power for each case over the respective strides, as shown in Fig. 6c, the net energy delivered by the passive prosthesis during stair ascent was 0.0 J/stride, the net energy delivered by the powered prosthesis was on average 11.3 J/stride, while the net energy observed in the non-amputee subject data is 36.7 J/stride. As such, unlike the passive prosthesis, the powered prosthesis delivers substantial energy to the user, although due to power limitations, the energy delivered is approximately one third of the energy observed during typical non-amputee stair ascent.

D.1.6.2 *Stair Descent Controller*

As depicted in Fig. 7a, the non-amputee ankle angle cycles between approximately 20 deg of dorsiflexion (at mid-stride) and 20 deg of plantarflexion (at the start and end of stride). The powered prosthesis similarly cycles between these configurations, as it dorsiflexes substantially during at mid-stride, and plantarflexes substantially before toe-strike. In contrast, the passive ankle dorsiflexes relatively little in mid-stance (due to its relatively high stiffness), and provides no plantarflexion, since doing so requires motive power. Although the ankle torques provided by each prosthesis type do not differ

substantially during stair descent (Fig. 7b), the power characteristic of the two prosthesis types is substantially different, as apparent in Fig. 7c. An integration of the power over the stride indicates 0.0 J/stride of energy dissipation provided by the passive prosthesis and 40.7 J/stride provided by the powered prosthesis. In comparison, the non-amputee data indicates an average energy dissipation of 40.0 J/stride. As such, the powered prosthesis provides a substantially better approximation of non-amputee descent behavior, relative to the passive prosthesis.

The averaged force plate data associated with stair descent foot strike, shown in Fig. 8, indicates distinct differences between the passive and powered prostheses during the loading response of both the sound and prosthetic sides. As indicated in Fig. 8a, during foot strike on the prosthesis side, the powered prosthesis enables a substantially more gradual loading response than does the passive prosthesis. This results from the fact that the passive prosthesis makes heel contact, while the powered prosthesis makes toe contact, and gradually accepts loading through the damping of the ankle as the ankle dorsiflexes under load.

As shown in Fig. 8b, during foot strike on the sound side, the powered prosthesis enables substantially lower peak forces than sound-side foot strike when wearing the passive prosthesis. On average, the peak forces associated with foot strike with the passive prosthesis is 1350 N, while the corresponding peak with the powered prosthesis is 1130 N, indicating a 15% reduction in peak force with the powered prosthesis. This reduction is presumably due to the increase power dissipation observed and previously described, which removes body mass kinetic energy during descent, thus reducing the velocity of the sound foot at foot strike, and thus reducing peak forces associated with impact. As such, the powered prosthesis appears to improve foot strike characteristics on both sides during stair

descent, relative to the passive prosthesis.

D.1.6.3 *Controller Generalizability*

Anecdotally, the controller was surprisingly robust to variation in stair geometry, largely because the switching conditions are almost exclusively based on angular velocities, rather than angles. Specifically, the switching conditions listed in Tables I and II (for ascent and descent, respectively) include several compound conditions that involve both angles and angular velocities. In these compound conditions, one condition is a "guard" condition, while the other is the actual "switching" condition. The guard condition is intended to restrict the transition to a narrower part of the state space, in the event that the actual switching condition may occur elsewhere in the state space. In all compound conditions listed in Tables I and II, the angles are guard conditions, while the angular velocities are the switching conditions. The one exception is T_{A23}, although that condition is based on the push-off equilibrium angle, which is known by the controller (i.e., it is an impedance equilibrium angle, not an independently adjustable threshold). Therefore, there are in fact no tunable angle-based *switching* conditions in the stair controllers. Although the angle-based *guard* conditions are tunable, operation of the controller is generally not sensitive to reasonable variations in these thresholds.

Despite anecdotal evidence of controller robustness to variation in stair geometry, motion capture was conducted with only one staircase, and therefore insufficient data exists with which to formally characterize the generalizability of the controller to variation in stair geometry.

D.1.6.4 *Supervisory Controller*

As can be seen in Fig. 10, the subject was able to reliably command the prosthesis to switch to the appropriate activity controllers. The 15 trials shown were representative of general use, and indicate no mistaken mode switches. As such, the supervisory controller provides a robust means of controlling walking and stair ascent and descent functionality. One drawback to the controller, however, is that it requires the user to pause when exiting stair ascent, and when entering and exiting stair descent. In contrast, a passive prosthesis does not change behavior for these different activities, and therefore requires no pause when transitioning between them. As a result, there is a clear trade-off introduced by a powered prosthesis; namely, the prosthesis is able to provide multiple "activity-specific" behaviors, but doing so requires the device to switch between these behaviors. The extent to which these behaviors have value to a user will likely depend on the balance between the real or perceived enhancement in function within a given activity, relative to the real or perceived inconvenience of switching from one activity controller to another.

D.1.7 Conclusion

This paper presents the design and single-subject assessment of a control system for stair ascent and descent in a powered transtibial prosthesis, and a supervisory controller that facilitates transitions between standing, level ground walking, stair ascent, and stair descent controllers. Experimental results on a single amputee subject indicate that the powered prosthesis provides potential biomechanical benefit relative to a passive prosthesis during stair ascent and descent, specifically: 1) net power assistance during stair ascent; 2) net power dissipation during stair descent; and 3) improved bilateral foot strike characteristics during

stair descent. Additionally, experimental results of a supervisory controller indicate that the subject was able to reliably transition between four activity controllers, albeit with a pause when switching out of stair ascent, and in and out of stair descent.